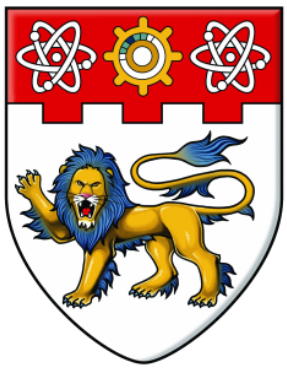

NANYANG TECHNOLOGICAL UNIVERSITY

ENGINEERING OF THIENOTHIOPHENE-BASED CONJUGATED MOLECULES FOR THE DEVELOPMENT OF EFFICIENT P-TYPE SEMICONDUCTOR

ABE YUICHIRO

INTERDISCIPLINARY GRADUATE SCHOOL
ENERGY RESEARCH INSTITUTE @ NTU (ERI@N)

2016

ENGINEERING OF THIENOTHIOPHENE-BASED CONJUGATED MOLECULES FOR THE DEVELOPMENT OF EFFICIENT P-TYPE SEMICONDUCTOR

ABE YUICHIRO

Interdisciplinary Graduate School
Energy Research Institute @ NTU (ERI@N)

A thesis submitted to the Nanyang Technological University in partial fulfilment of the requirement for the degree of
Doctor of Philosophy

2016

Statement of Originality

I hereby certify that the work embodied in this thesis is the result of original research and has not been submitted for a higher degree to any other University or Institution.

11th August 2016
Date

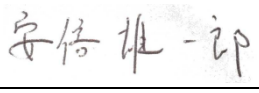

Abe Yuichiro

Abstract

In order to reduce the cost of energy production from clean and renewable energy source, next-generation solar cells have been extensively studied. Amongst the candidates for the next generation solar cells, organic solar cells have the advantage of a higher degree of freedom in terms of materials design and selection. Decades of research in the field has resulted in impressive power conversion efficiency (PCE). However, the materials development relies heavily on trial-and-error method due to the lack of good understanding of how to translate the molecular structure to the solid-state structure in devices. In this paper, small molecules having π–conjugated backbones have been synthesized and their properties have been studied in an attempt to establish the design principles of efficient organic semiconductors for the application in organic photovoltaic (OPV) devices.

Novel small molecules based on dithienocyclopentathieno[3,2-b]thiophene (DTCTT) structure which consists of thienothiophene core was synthesized and compared to the structural analogue based on Indacenodithiophene (IDT) which consists of a benzene core instead. Dense molecular packing structure due to the strong interactions between sulfur atoms in the thienothiophene unit was expected to result in an increase in the hole mobility. This is an important parameter for high-efficiency solar cells. The effect of the packing structure on optical, thermal, and charge transport properties was investigated. As expected, the DTCTT-based compound showed enhanced crystallinity and higher hole mobility than the IDT-based compound. However, when it was mixed together with the fullerene acceptor and incorporated into OPV devices, no significant increase in PCE was obtained. Although the film crystallinity of the DTCTT-based small molecule was high, uneven and rough film morphology resulted in poor device performance. The control of morphology in the solid state was the key to further improvement of device efficiency.

Subsequently, derivatives of the DTCTT-based molecules with different side groups were synthesized and their self-assembled structures were analyzed in detail. This approach was attempted to understand the impact of molecular design into the solid-state structure which eventually leads to control of the morphology. Structural analysis using X-ray diffraction techniques and computational calculations revealed that the derivatives adopt a columnar structure with the slip-stacked manner of π–π stacking. It was also found that the derivatives with two thiophene rings in the side group showed the unique crystal-to-crystal reversible phase transition behavior in heating and cooling cycle. It was concluded that the columnar one-dimensional structure reorganized during the transitions in a similar manner to liquid crystalline materials. Due to the one-dimensional organization favorable to charge transport, a hole mobility value as high as 0.02 $cm^2/V \cdot s$ was obtained in the field-effect transistor.

The novel DTCTT-based molecules demonstrated high potential as efficient p-type organic semiconductors in solar cells and filed-effect transistors. With a rigorous structural analysis of the molecular self-assembly and the solid-state behavior, modified molecular structures were rationally proposed as a direction for the future research. The approach carried out in this thesis is believed to have provided detailed guidance for the design of efficient organic semiconductors.

Acknowledgements

My Ph.D. pursuit was like a long way of journey. Life in these four years at NTU was full of difficulties and anguish due to inexperience in a foreign culture and little progress of researches. Under such circumstances, I was supported and guided by people by my side. I would like to address my gratitude here.

First and foremost, I would like to thank my supervisor, A/P Lam Yeng Ming for her invaluable advices, guidance and coaching. Without her kind and continuous support, I would have not finished my Ph.D. study. I would also like to thank A/P Cesare Soci for his astute advice from a physist's viewpoint, A/P Andrew Clive Grimsdale for his passionate lecture on synthetic and material chemistry, and Prof Michael Toney for his generosity to have collaboration in X-ray diffraction measurement at the SLAC.

In terms of assistance with experiments, I appreciate Dr. Li Hairong for his help and discussion on organic synthesis, Chin Xin Yu for my training of OFET fabrication, and Dr. Bruno Donnadieu for his help with conducting the single crystal X-ray diffraction measurement. I am also very much grateful to Prof. Lam's group members, especially to Dr. Teddy Salim for his sincerity. They helped me to relieve my nerve during my life in Singapore.

My research works couldn't have been completed without the financial and facility support from the Energy Research Institute at NTU (ERI@N). I would also like to extend my gratitude to the people at ERI@N for their help to my work, lecture, and discussion.

Finally, I sincerely appreciate and would like to thank my parents for giving me the opportunity to explore this world.

Table of Contents

Table Captions

Figure Captions

Abbreviations

OPV	Organic Photovoltaics
sm-OPV	Small molecular Organic Photovoltaics
DSSC	Dye-sensitized Solar Cell
OFET	Organic Field-effect Transistor
OLED	Organic Light-emitting Diode
NREL	National Renewable Energy Laboratory
PCE	Power Conversion Efficiency
FF	Fill Factor
DA	Donor Acceptor
CS	Charge Separation
BHJ	Bulk Hetero Junction
HOMO	Highest Occupied Molecular Orbital
LUMO	Lowest Unoccupied Molecular Orbital
EQE	External Quantum Efficiency
AFM	Atomic Force Microscope
POM	Polarized Optical Microscope
TEM	Transmission Electron Microscope
SEM	Scanning Electron Microscope
XRD	X-ray Diffraction
SWAXD	Small and Wide Angle X-ray diffraction
GI-SWAXD	Grazing Incident Small and Wide Angle X-ray Diffraction
SCLC	Space Charge Limited Current
MALDI-TOF MS	Matrix-assisted Laser Desorption/Ionization – Time-of-Flight Mass Spectroscopy
NMR	Nuclear Magnetic Resonance
DSC	Differential Scanning Calorimetry
DFT	Density Functional Theory
HTM	Hole Transporting Material

DTCTT	Dithienocyclopenta-thieno[3,2-b]thiophene
IDT	Indacenodithiophene
IDTT	Indacenodithieno[2,3-b]thiophene
TT	Thieno[3,2-b]thiophene
BT	2,1,3-Benzothiadiazole
Th	Thiophene
PDMS	Poly(dimethylsiloxane)
PTFE	Poly(tetrafluoroethylene)
oDCB	ortho-Dichlorobenzene
PEDOT:PSS	Poly(3,4-ethylenedioxythiophene):Polystyrene
ITO	Indium Tin Oxide

Chapter 1

Introduction

Photovoltaic power generation is a promising system towards achieving a sustainable society as it provides a mean to generate electricity using a clean and inexhaustible energy source–the sun. A variety of materials has been studied in order to develop high efficiency and cost-effective solar cells. Organic materials have the advantage of attaining desired properties through molecular design which has a wide degree of freedom in structures. A few decades of materials research in this field have established effective designing strategies of polymers and small molecules used in the system. However, this development relies heavily on trial-and-error method as there is a lack of good understanding of the solid-state structure of materials from nano to macroscopic scales which is essential for efficient devices. In this thesis, the molecular self-assembled structures of newly designed small molecules were investigated in detail. The thienothiophene unit was incorporated on an aromatic backbone so as to enhance the close packing structure through sulfur-sulfur interactions. This design was evaluated using material characterizations and its performance as donor component in solar cell devices. A particular focus was placed on the impact of molecular structures and intermolecular interactions on crystallization behavior. The findings and outcomes would contribute to a rational designing of efficient OPV materials.

1.1 Background

Electricity is essential in all aspects of our urban life such as lightning, consumer electronics, transportation, product manufacturing, etc. and the life without it is hardly imaginable. However, the desire for better life and economic growth causes an exponential increase of the electricity demand, which has triggered serious environmental problems globally. Present electricity production heavily relies on fossil fuels but it is predicted to deplete in the near future. In addition, emission of carbon dioxide which occurs during combustion of the fuels will have a detrimental effect on ecosystem by increasing the average global temperature due to the green-house effect. As a carbon-free electricity production, nuclear energy has been developed to cater to a fraction of the total electricity demand. Although this technology does not produce carbon dioxide or toxic gas emission during energy generation, it produces radioactive wastes which will remain for millions of years. Besides, it is concerned that nuclear power plant will cause a large-scale disaster like catastrophic accidents occurred in Chernobyl and Fukushima.

Fossil fuels and nuclear energy currently take charge of majority of electricity production: about 77% in total electricity production (Fig. 1.1, Fossil fuels and nuclear). However the realization of the global warming issue and the threat of nuclear energy led to a demand for “clean” renewable energy sources. As a result, the term “sustainability” became a buzzword. Among the potential renewable energy sources, solar energy has advantages of its inexhaustible amount, feasibility, and cleanliness. According to the report published by the Renewable Energy Policy Network for the 21st Century (REN21) in 2015[1], 30–40 GW of solar photovoltaic system has been installed annually from 2010, reaching a total capacity of 177 GW in 2014. Consequently, electricity production from solar energy constitutes about 1% of global electricity production at present time (Fig. 1.1, Solar PV). This rapid growth is supported

by governmental and industrial investment the amount of which is the largest among that invested to renewable energy sources.

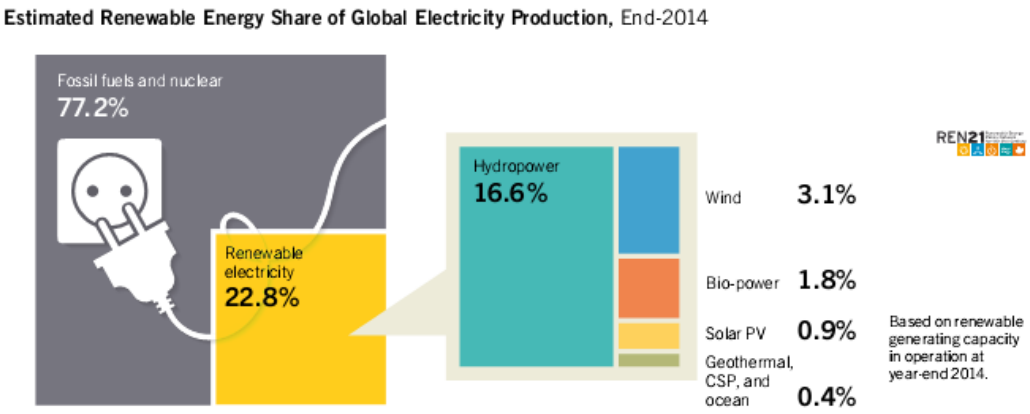

Fig. 1.1 Energy share percentiles of global electricity production[1]

A major challenge in solar cell research is to reduce the production cost so as to compete with the conventional power generation system. Further reduction is possible by developing cheaper manufacturing processes and improving the power conversion efficiency (PCE) of the device system. At this moment, silicon solar cell dominates more than 90% of market share in commercial solar cells because the material is abundant and a long-time technological development has enabled rapid cost down. However, the manufacturing process requires high temperature (>1000 °C) and large investment to produce wafers which is suitably high purity for solar cell applications. High energy consumption in this process results in a long energy payback time. As a solution to this technology, solution-based manufacturing process such as the roll-to-roll manufacturing has been proposed as a low temperature and cost-effective manufacturing option.

Improvement in the device efficiency also brings about reduced energy production cost as every doubling of the efficiency of solar cell can reduces the cost per unit electricity by half. The goal of this attempt was presented; an

upper limit of solar cell efficiency was calculated in 1961 by two physicists, Shockley and Quesser[2]. Assuming a simplified operating condition and taking the balance of both excitation and radiative recombination into account, they determined a 33% limit in PCE for any type of single junction solar cells. Since the present commercially available silicon solar cells show c.a. 15% PCE, there is still room for doubling the efficiency. However, the research in silicon solar cell has been conducted for a long time and there is less scope for further improvement. Therefore, various next-generation semiconducting materials have been explored as alternatives. Inorganic semiconductors such as cadmium telluride (CdTe), gallium arsenide (GaAs), and copper indium gallium diselenide (CIGS) have been developed and consisted of the second generation solar cells. Although their efficiency is competitive to the first generation crystalline silicon solar cells, they necessitate the use of toxic and expensive materials. In an attempt to find cheaper and greener alternatives, another class of solar cells has emerged and they are called third generation solar cells including dye sensitized solar cells (DSSC), quantum dot solar cells, organic solar cells, and metal-organic hybrid perovskite solar cells. The National Renewable Energy Laboratory (NREL) in the US has published the efficiency chart of various types of solar cells (Fig. 1.2). Some of the solar cells have already achieved very high efficiency at laboratory scale (usually a cell size of 0.02–0.1 cm^2) but there are many issues to be solved before commercialization of technology, which includes scaling up the manufacturing into the large modules (> 10 cm^2). Other issues are a short operation lifetime of devices and poor environmental friendliness and compatibility with public health of materials. None of the potential candidates have yet to meet all the prerequisites in an economically viable manner. Thus, the materials development is still crucial to achieve the final goal.

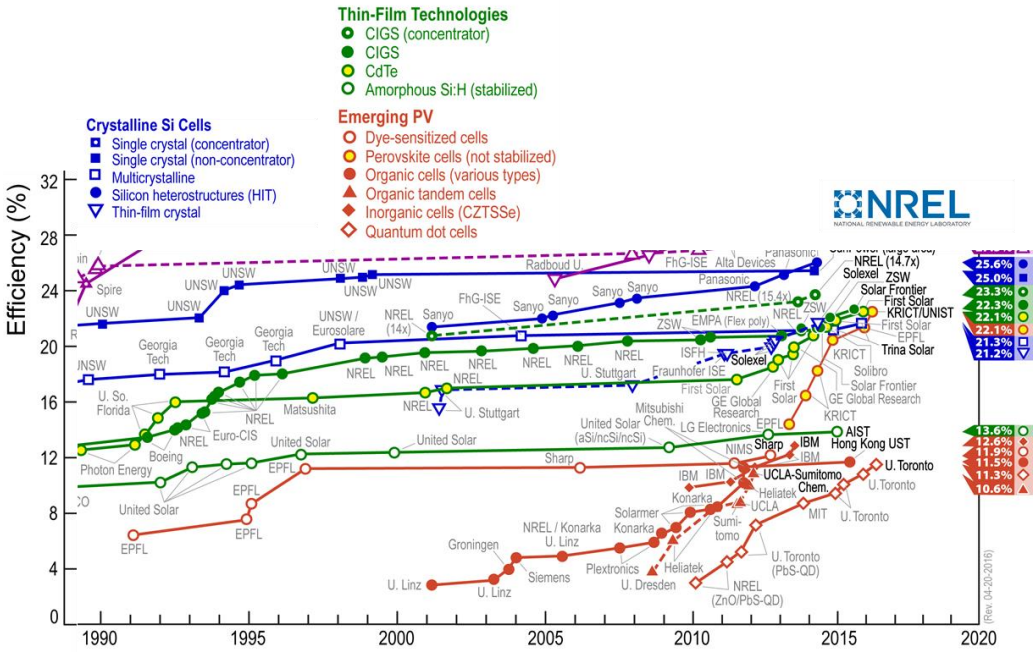

Fig. 1.2 Solar cell efficiency chart of emerging PVs[3]

1.2 Organic solar cells

Organic solar cells have come a long way since the first demonstration of an efficient organic solar cells (1% PCE) by CW Tang from Kodak in 1986[4]. Ever since then, the cell efficiency has increased gradually and it has reached 10.8% as the current certified highest in record[5], though a company claimed they achieved a cell with 13% PCE. The OPV has advantage as it is practically applicable to the roll-to-roll manufacturing process which allows a reduced production cost. In addition, OPV materials generally have the high molecular absorption coefficient which enables them to be operated under diminished and scattered lighting conditions, whereas silicon solar cells drop their efficiency drastically under such a condition. Commercialized products have already been manufactured by companies such as Heliatek GmbH; they have production lines capable of producing cells with PCE of 7–8%.

One of major challenges for the development of materials used in OPV is to

optimize the solid-state structure and morphology in thin film. These structural factors affect the charge transport and recombination process, and thus they are crucial for high efficient devices. However they are difficult to predict because we do not have a good understanding of translating a molecular structure in the nano- and macroscopic scale encompassing entire devices. Since the solid-state structure of organic molecules is stabilized by weak van der Waals interaction, the packing structures in crystals have a certain degree of freedom in the rotation and displacement of molecules. This character induces polymorphs and structural defects, which make it difficult to predict the molecular organization in silico using theoretical calculation. In addition, the photovoltaic converting layer, or the active layer, needs both well-organized p-type and n-type semiconductors (donor and acceptor) for a good device operation. In order to achieve such a good morphology of donor and acceptor materials, the optimization process is crucial. However this process is often tedious and time-consuming due to trial-and-error method used and it has lack of rational evidence in terms of how to achieve the optimized structure from a molecular structure. In order to bring the rational molecular designing into reality, it is imperative to understand the structure/property relationship in detail.

1.3 Designing efficient organic semiconductors for BHJ solar cells

The optimum power conversion efficiencies in organic solar cells can be calculated with a few assumptions in mind as was demonstrated by Dennler and coworkers[6] (Fig. 1.3). In this figure, two assumptions were used: i) OPV devices can convert 90% of solar energy at each wavelength from 300 nm to the wavelength corresponding to the bandgap energy (horizontal axis, nm) (EQE = 90%) and ii) devices have a fill factor of 0.7 (FF = 0.7). These values have been observed in the state-of-the-art OPV devices[7-9] and are reasonably achievable. Taking into account of the energy losses during charge transfer and transport, a PCE of 17–20% for a single junction OPV device could be possible. In order to

reach this 20% goal, donor-acceptor (D-A) materials used in the active layer need to fulfill the following criteria:

1) Wide absorption spectra up to 800–1000 nm.

2) Higher and more balanced charge transport mobility for both holes and electrons in order to achieve FF of 0.7–0.8.

Sun light has a wide spectrum ranging from ultraviolet to infra-red: 300 to 2500 nm. In order to take advantage of whole range of the spectrum, organic semiconductors used in solar cells need to have an essentially low energy bandgap. However, the requirement of lower band gap and higher open-circuit voltage is incompatible and a broad absorption around 800–1000 nm is ideal to extract maximum power as the peak-top position indicates in Figure 1.3. Some of conjugated aromatic systems have already achieved as low bandgap as the range using co-polymerizing electron-rich and -deficient monomers (DA copolymers) [10,11].

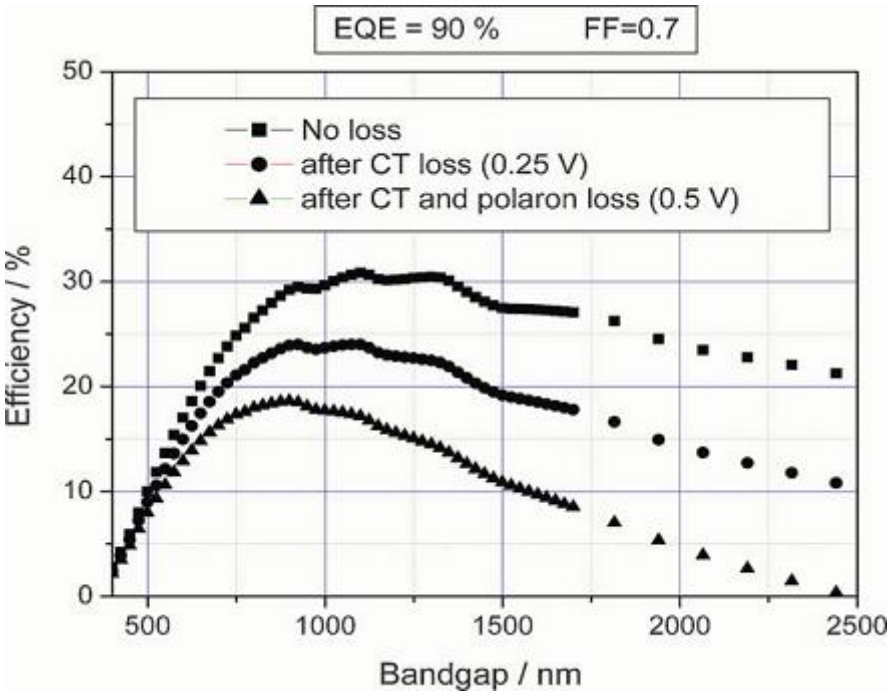

Fig. 1.3 Plot of practical maximum efficiency versus band gap for bulk heterojunction solar cell[6]

High carrier mobility is generally difficult to achieve in the bulk-heterojunction (BHJ) film where donor and acceptor materials form mixed and randomized network. However, the D-A morphology in the BHJ film provides a good charge separation, essential step for solar cell operation, due to the high surface area between donor and acceptor materials, and thus the OPV device with the BHJ active layer show the best performance. In BHJ film, a typical carrier mobility is 10^{-6}–10^{-4} $cm^2/V \cdot s$ whereas in pristine film consists of only donor or acceptor materials, the mobility of 10^{-3}–10^{-2} $cm^2/V \cdot s$ in the diode configuration and 1–10 $cm^2/V \cdot s$ in the transistor configuration has been achieved. This difference can be attributed to the difficulty in making both organized and interpenetrating structure of donor and acceptor materials over the entire device scale[12]. Further enhancement up to 10^{-2} $cm^2/V \cdot s$ is proposed as an optimum mobility value to extract charge carriers effectively without losing them through the recombination mechanism[13]. In order to achieve this goal, careful material design and a good understand of the packing structure is necessary so as to achieve an ideal solid-state structure in which molecules form a closely packed system having a high degree of overlapped molecular orbitals, together with a long range order (i.e. fiber-like morphology). The solid-state structure is also affected by crystallization condition and hence the optimization process with varying parameters such as temperature, solvent system, and additives needs to be investigated. Therefore in this thesis, the rational molecular design and its effect on the molecular self-assembled structures has been explored.

1.4 Objectives and Scope

The research in this thesis focuses on the investigation of the self-assembled structure of small molecules based on dithienocyclopentathieno[3,2-b]thiophene (DTCTT). They are compared to the analogous small molecules based on Indacenodithiophene (IDT) (Fig. 1.4). The IDT structure has been attracting considerable attention recently as a building block in organic

semiconductors because of its coplanarity and extended conjugation length. These characters made it a good candidate as a backbone unit for polymeric semiconductors; polymers containing this backbone structure have shown to have mobility values of over 1 $cm^2/V \cdot s$ in OFET[14,15]. It was also incorporated into p-type polymers[16-18], p-type small molecules[19-21], and n-type small molecules[22-24] for OPV application and has achieved a good device performance. Dicyclopentadithieno-thieno[3,2-b]thiophene (DTCTT) has a similar structure with the IDT except that the central benzene is replaced by a thieno[3,2-b]thiophene unit (TT). The incorporation of TT units into organic semiconductors has proven to be beneficial for the improvement of charge transport properties due to its close inter-molecular packing structure, promoted by the presence of the sulfur atoms[25]. This incorporation has led to some high mobility organic semiconductors such as the benzothieno[3,2-b]benzothiophene (BTBT) and the poly(2,5-bis(3-alkylthiophen-2-yl)thieno[3,2-b]thiophenes) (PBTTT)[25-28]. Large conjugation backbone and a strong electron donating ability as well as the rigid backbone structure of the DTCTT are also advantageous for light-harvesting ability over a wide spectral range. These features are ideal for high performance OPV materials. However, D-A polymers composed of DTCTT backbone have yet to show good photovoltaic performance so far[29-31]. Detailed structural analysis has not been reported due to the intrinsic structural uncertainty of polymeric materials and small molecules composed of DTCTT backbone has yet to be reported.

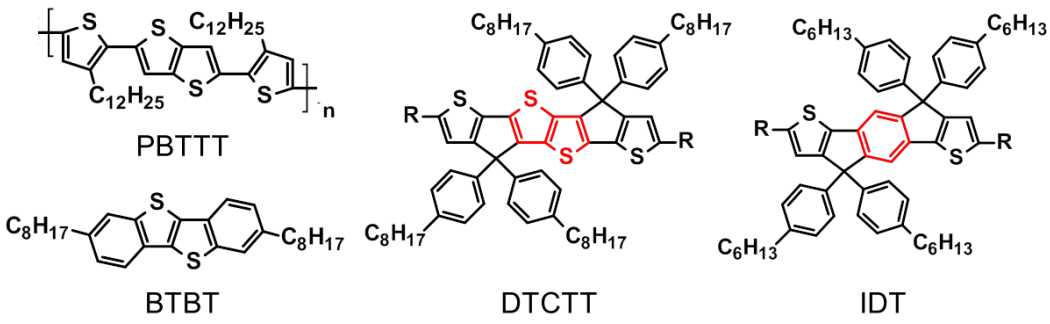

Fig. 1.4 Chemical Structures of PBTTT, BTBT, DTCTT and IDT backbone

This research aims to provide insight into the development of efficient p-type organic semiconductors for OPV application using the molecular engineering technique. Both DTCTT and IDT were incorporated into small molecular OPV (sm-OPV) and the photovoltaic properties were investigated. The hole mobility was measured using hole-only devices and OFET devices. These results were discussed so as to elucidate structure/property relationship.

Decades of research and developments in this field has borne fruits of efficient OPV materials, some of which achieved record efficiency of 11–13%. However, such a materials development largely relies on trial-and-error method attributed to lack of understanding of how the molecules form the self-assembled structures. Theoretical simulation predicts the maximum possible PCE, as discussed above section 1.3, suggesting that there is huge room for improving the present efficiency further to 20%. The OPV device efficiency has increased rapidly since the first OPV demonstration, but these seems plateau in recent years mainly due to the limitation in useful empirical approach applicable to materials development. Small molecular OPV (sm-OPV) is a good system to quantitatively investigate the relationship between the solid-state structure and properties in film because, unlike polymer materials, small molecules have defined structures. In this thesis, the molecular designing of DTCTT-based small molecules was explored and the effect of incorporating TT unit into the backbone structure was validated through characterization and structural analysis. This approach as well as the novel DTCTT-based small molecules has potential to contribute to the further development in this field.

1.5 Dissertation Overview

This thesis consists of six chapters. The introductory chapter provides a broad overview and motivation behind this PhD study. Organic solar cell is introduced from a broad perspective including significance of this technology,

achievement, issues toward better performance, and the limitations of the current approach to materials development. On top of this, the aims, scope, and contribution of this work are presented.

In Chapter 2, literature review is provided to highlight the noteworthy researches in the development of organic semiconductors. Works that has been carried out to explore the relationship between molecular structures and the intrinsic charge transport properties are summarized. Following that, the effect of the morphology and crystallinity in thin film on the performance of OPV devices is explained. Representative materials used in the BHJ active layer in OPV devices are also presented.

In Chapter 3, the principles of device operation and characterization techniques used in this thesis are explained. The experimental procedure, organic synthetic techniques, and materials characterization are presented. Principles of solar cell evaluation, charge career mobility measurement, and structural analysis using X-ray diffraction techniques are also presented.

In Chapter 4, the DTCTT-based novel donor molecule, di(HTh2BT)DTCTT, and the structurally similar IDT analogue, di(HTh2BT)IDT, are synthesized and their properties are characterized. The effect of incorporating TT unit in the DTCTT backbone is investigated with respect to their optical, thermal, structural, and charge transport properties. They are then blended with the $PC_{71}BM$ acceptor to form the BHJ layer in sm-OPV devices. After optimizing the device fabrication, their device performance is explained in relation with the thin-film properties.

In Chapter 5, derivatives of the DTCTT- and IDT-based molecules with different side groups were synthesized and characterized for the purpose of investigating the self-assembled structure in detail. Difference in crystallinity

based on their varied side group structures is discussed using X-ray diffraction techniques carried out in the single crystal, powder, and thin-film samples. A particular focus is placed on the liquid crystal-like reversible phase transition behavior of the DTCTT derivatives. The relationship between crystallinity and charge carrier mobility in the OFET is discussed.

In the last chapter, key results obtained in this work are summarized. Based on findings and outcomes in this thesis, modified structures of the DTCTT derivatives are rationally proposed and the aims are explained. Ongoing research is also presented. Finally, the molecular designing strategy applied in this thesis is validated.

1.6 Findings and Outcomes/Originality

This research would contribute to the scientific community in the field of the molecular designing of organic semiconducting materials used in OPV devices. The contributions are specified as follows;

1. Developed novel DTCTT-based molecular donor materials as a promising backbone structure for sm-OPV
2. Demonstrated that the incorporation of TT unit in backbone structure led to red-shift in absorption spectra, better crystallinity, and higher hole mobility suitable to the OPV application
3. Suggested the important role of S-S interaction in designing a self-assembly structure in these materials.
4. Discovered the unusual reversible phase transition behavior of the DTCTT derivatives and opened up the possibility of designing stimuli-responsive organic semiconductors.
5. Characterized the detailed self-assembled structure of the DTCTT derivatives and demonstrated a viable approach to a rational material design for developing efficient OPV materials.

References:

[1] REN21Secretariat, Renewables 2015 Global Status Report, Paris, 2015, p. 175.

[2] W. Shockley, H.J. Queisser, *Journal of Applied Physics* 32 **(1961)** 510.

[3] NREL, *http://www.nrel.gov/ncpv/images/efficiency_chart.jpg* (accessed 30 October 2015).

[4] C.W. Tang, S.A. VanSlyke, *Applied Physics Letters* 51 **(1987)** 913.

[5] Y. Liu, J. Zhao, Z. Li, C. Mu, W. Ma, H. Hu, K. Jiang, H. Lin, H. Ade, H. Yan, *Nat Commun* 5 **(2014)** 5293.

[6] G. Dennler, M.C. Scharber, C.J. Brabec, *Adv Mater* 21 **(2009)** 1323.

[7] X. Guo, N. Zhou, S.J. Lou, J. Smith, D.B. Tice, J.W. Hennek, R.P. Ortiz, J.T.L. Navarrete, S. Li, J. Strzalka, L.X. Chen, R.P.H. Chang, A. Facchetti, T.J. Marks, *Nat Photon* advance online publication **(2013)**.

[8] M.D. Irwin, D.B. Buchholz, A.W. Hains, R.P.H. Chang, T.J. Marks, *Proceedings of the National Academy of Sciences* 105 **(2008)** 2783.

[9] Z. He, C. Zhong, S. Su, M. Xu, H. Wu, Y. Cao, *Nat Photon* 6 **(2012)** 591.

[10] R.L. Uy, S.C. Price, W. You, *Macromolecular Rapid Communications* 33 **(2012)** 1162.

[11] J.-S. Wu, S.-W. Cheng, Y.-J. Cheng, C.-S. Hsu, *Chemical Society Reviews* 44 **(2015)** 1113.

[12] J.A. Bartelt, D. Lam, T.M. Burke, S.M. Sweetnam, M.D. McGehee, *Advanced Energy Materials* 5 **(2015)** n/a.

[13] D. Neher, J. Kniepert, A. Elimelech, L.J. Koster, *Sci Rep* 6 **(2016)** 24861.

[14] I. McCulloch, R.S. Ashraf, L. Biniek, H. Bronstein, C. Combe, J.E. Donaghey, D.I. James, C.B. Nielsen, B.C. Schroeder, W. Zhang, *Accounts of Chemical Research* 45 **(2012)** 714.

[15] X. Zhang, H. Bronstein, A.J. Kronemeijer, J. Smith, Y. Kim, R.J. Kline, L.J. Richter, T.D. Anthopoulos, H. Sirringhaus, K. Song, M. Heeney, W. Zhang, I. McCulloch, D.M. DeLongchamp, *Nat Commun* 4 **(2013)** 2238.

[16] X. Guo, M. Zhang, J. Tan, S. Zhang, L. Huo, W. Hu, Y. Li, J. Hou, *Adv Mater* 24 **(2012)** 6536.

[17] D.B. Sulas, K. Yao, J.J. Intemann, S.T. Williams, C.-Z. Li, C.-C. Chueh, J.J. Richards, Y. Xi, L.D. Pozzo, C.W. Schlenker, A.K.Y. Jen, D.S. Ginger, *Chemistry of Materials* 27 **(2015)** 6583.

[18] Y.-C. Chen, C.-Y. Yu, Y.-L. Fan, L.-I. Hung, C.-P. Chen, C. Ting, *Chemical Communications* 46 **(2010)** 6503.

[19] Y. Sun, G.C. Welch, W.L. Leong, C.J. Takacs, G.C. Bazan, A.J. Heeger, *Nat Mater* 11 **(2012)** 44.

[20] Y. Chen, X. Wan, G. Long, *Accounts of Chemical Research* 46 **(2013)** 2645.

[21] J.-L. Wang, Q.-R. Yin, J.-S. Miao, Z. Wu, Z.-F. Chang, Y. Cao, R.-B. Zhang, J.-Y. Wang, H.-B. Wu, Y. Cao, *Advanced Functional Materials* 25 **(2015)** 3514.

[22] H. Bai, P. Cheng, Y. Wang, L. Ma, Y. Li, D. Zhu, X. Zhan, *J. Mater. Chem. A* 2 **(2014)** 778.

[23] Y. Lin, Q. He, F. Zhao, L. Huo, J. Mai, X. Lu, C.J. Su, T. Li, J. Wang, J. Zhu, Y. Sun, C. Wang, X. Zhan, *J Am Chem Soc* 138 **(2016)** 2973.

[24] W. Zhao, D. Qian, S. Zhang, S. Li, O. Inganäs, F. Gao, J. Hou, *Adv Mater* 28 **(2016)** 4734.

[25] J.I. Park, J.W. Chung, J.Y. Kim, J. Lee, J.Y. Jung, B. Koo, B.L. Lee, S.W. Lee, Y.W. Jin, S.Y. Lee, *J Am Chem Soc* 137 **(2015)** 12175.

[26] H. Iino, T. Usui, J. Hanna, *Nat Commun* 6 **(2015)** 6828.

[27] M.O. Ahmed, C. Wang, P. Keg, W. Pisula, Y.-M. Lam, B.S. Ong, S.-C. Ng, Z.-K. Chen, S.G. Mhaisalkar, *Journal of Materials Chemistry* 19 **(2009)** 3449.

[28] I. McCulloch, M. Heeney, C. Bailey, K. Genevicius, I. MacDonald, M. Shkunov, D. Sparrowe, S. Tierney, R. Wagner, W. Zhang, M.L. Chabinyc, R.J. Kline, M.D. McGehee, M.F. Toney, *Nat Mater* 5 **(2006)** 328.

[29] H. Bronstein, R.S. Ashraf, Y. Kim, A.J. White, T. Anthopoulos, K. Song, D. James, W. Zhang, I. McCulloch, *Macromolecular Rapid Communications* 32 **(2011)** 1664.

[30] Y.J. Cheng, C.H. Chen, T.Y. Lin, C.S. Hsu, *Chem Asian J* 7 **(2012)** 818.

[31] B.C. Schroeder, R.S. Ashraf, S. Thomas, A.J. White, L. Biniek, C.B. Nielsen, W. Zhang, Z. Huang, P.S. Tuladhar, S.E. Watkins, T.D. Anthopoulos, J.R. Durrant, I. McCulloch, *Chem Commun (Camb)* 48 **(2012)** 7699.

Chapter 2

Literature Review

In this chapter, the historical developments of organic semiconductors were reflected and noteworthiness of research results, especially, the designing principle for making high performance materials was highlighted. Charge transport properties of organic materials, which behave differently from the inorganic counterparts, were intensively studied using computer modeling as well as experimental characterization. Polymorphism is an inevitable aspect of organic solid when structure/property relationship is to be discussed. These findings give insights to design efficient organic photovoltaic materials. In addition to charge transport properties, structural and morphological factors play a critical role when it comes to device fabrication and the operation. These studies were presented and discussed from a view point of the material development so as to clarify the factors need to be considered for designing novel molecules used in organic photovoltaics.

2.1 Organic Electronics

Semiconductor industry has emerged from metal and metal oxide material and became a viable business to fabricate the integrated circuit incorporated in electronic devices. On the other hand, organic material has been considered an insulating material for a long time and only limited researches were done from a fundamental view point. The situation has changed since the discovery of conductive polymers such as poly acetylene[1] developed by Prof H. Shirakawa, A. Heeger, and A. MacDiarmid, who were awarded novel prize in chemistry in 2001. Ever since, the conductive polymers have been used to many part of electric tool, utilizing the lighter, more flexible and less expensive features than inorganic semiconductors.

A crucial characteristic of organic semiconductors is to control the electric conductance. In this respect, more important fundamental property to characterize the charge transport properties is the charge carrier mobility value μ; conductivity σ and both electron and hole mobility have a relationship as shown below.

$$\sigma = e(n\mu_e + p\mu_h)$$

where e is the elementary charge and n and p are the number density of electrons and holes, respectively. Unlike metallic bond and ionic bond of inorganic semiconductors, organic semiconductors are formed by relatively weak Van der Waals interaction between aromatic molecules where electrons strongly binds to the molecular orbitals through coulombic forces and often have spatial disorder. In such cases, the electrical model which appropriately describes the charge transport characters is the hopping mechanism. Structural factors such as the mode of packing, defect site, and polymorphs paly important role for it. Therefore, in order to design efficient organic semiconductor

materials, it is necessary to understand the charge carrier transport behavior and molecular packing structure. In this literature review, the structure and semiconducting property relationship were discussed with referring some key research results in this field.

2.1.1 Charge transport property of organic molecules and the structure relationship

According to the classical theory of the hopping charge transport of organic materials[2,3], two key parameters are used to evaluate efficiency of material: transfer integral (t) and reorganization energy (λ). They determine the intermolecular electron exchange rates and then the ultimate charge carrier mobility. The former is a degree of close packing as well as the mode of alignment between adjacent molecules. The latter means the degree of intra-molecular orbital deformation upon excitation, which largely related to the molecular rigidity and the electronic structure. Basically, the charge transport is enhanced when molecules pack closely with large overlap of p orbitals (large transfer integral) and excited molecules pass the charge carriers effectively to adjacent molecules without consuming the energy into reorganizing intramolecular molecular orbital (low reorganizing energy). The relationship can be described in the following equation[4]:

$$k_{et} = \frac{4\pi t^2}{h}\sqrt{4\pi\lambda RT}^{-1}\exp(\frac{-\lambda}{4RT})$$

where k_{et} is the hopping rate of charge transfer, h is Planck constant, t is the transfer integral, λ is the internal reorganization energy, R is the distance between adjacent molecules, T is temperature in Kelvin. Both parameters are sensitive to molecular alignment and subtle structural change, shift and tilt of π–π stacking manner can have a large impact (Fig. 2.1a and b); increase of the π–π stacking distance and tilt angle can lead to significantly reduced transfer

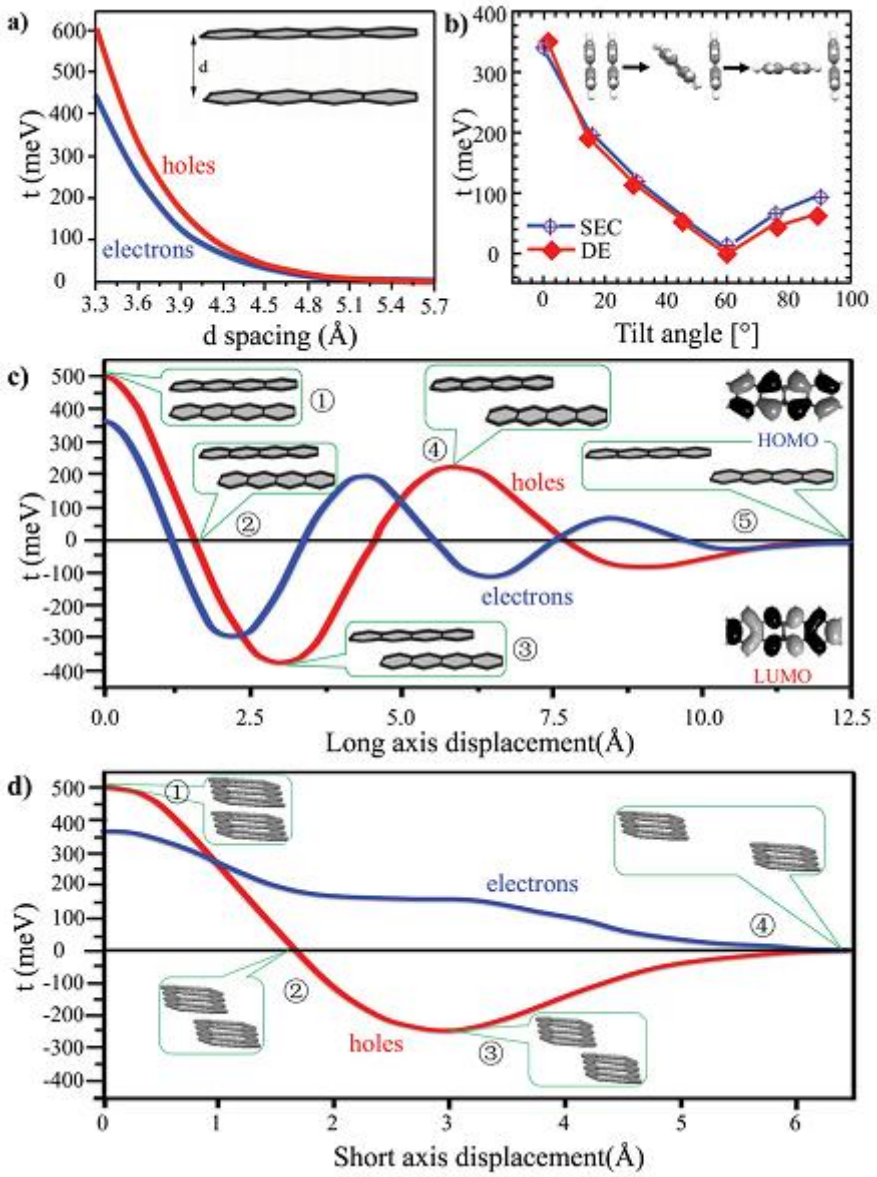

Fig. 2.1 INDO calculation graph of transfer integrals in the relation with dimer structure of tetracene: a) effect of π–π distance, b) effect of the tilt angle c) effect of the shifted distance along a long axis and d) short axis. The HOMO and LUMO molecular orbitals are shown in (c). Printed from a literature[5].

integrals. In addition, the two dimensional displacement of the dimer can also result in the decrease of wave function overlap and electronic coupling (Fig. 2.1c and d). It is noteworthy that the phases, bonding and antibonding

interaction of aromatic orbitals, also affect the transfer integral which resulted in oscillated curve in Fig. 2.1 c (see inset of the HOMO–LUMO structure of pentacene). This theoretical calculation suggested optimal molecular orbital overlap is more important than purely maximizing close intermolecular interaction. The important implication from this theoretical model is that polymorphism, different modes of packing structure, can potentially modulate electronic properties of material by introducing even subtle changes in molecular alignment. Since each polymorph is composed of the same chemical composition, the different properties arise from each mode of packing. In this regard, polymorphism provides an excellent platform to understand the

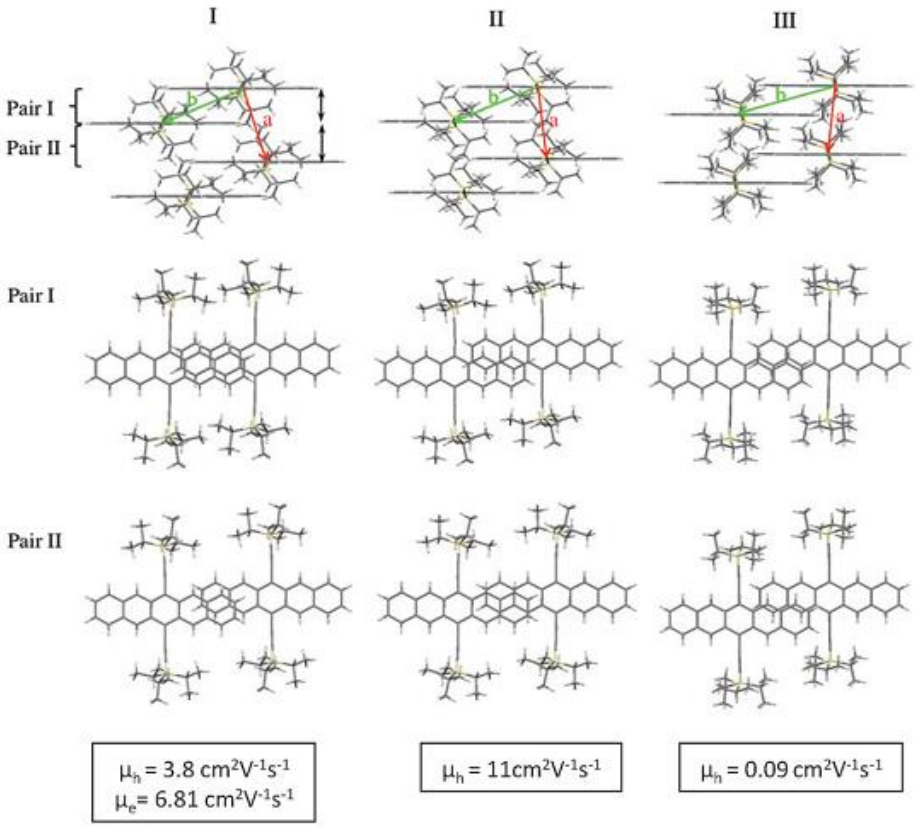

Fig. 2.2 Polymorphic structure of TIPS-pentacene crytals. The dimer structures in the crystal are shown together with their hole and electron mobility value[6].

structure/property relationship. Fig. 2.2 shows such an example of TIPS-pentacene derivatives. The pentacene derivatives can form three different polymorphs and they form dimer structures in a different manner especially in the manner of π−orbital overlapping. Despite of the subtle structural difference, measured mobility value varied in two orders of magnitude. This paper demonstrated importance of controlling polymorphic structures for efficient charge transport. Establishing crystallization condition to access a target polymorph is an effective strategy for enhancing material properties.

2.2 Morphology and Crystallinity of Organic Photovoltaics

The typical device architecture of an organic solar cell is shown in Fig. 2.3. It consists of an active layer, made up of both n- and p-type materials, sandwiched between two suitable electrodes such as Al and ITO. Between the active layer and the electrodes, other interlayers may be present to either block selective charges or to improve the charge transport process between the layers. The central phenomenon of electrons/holes generation takes place in the active layer and the morphology of this layer is of great importance. The first practical demonstration of organic cell was done by CW Tang from Kodak. They used a bilayer configuration (Fig. 2.3i) consisting of a phthalocyanine (p-type) layer and a perylene derivative (n-type) layer with PCE of 1%[7]. The generated electron-hole pairs in organic molecules bind strongly to the molecular orbital and need the internal electric field to be separated. This takes place between the donor (p-type) and acceptor (n-type) interface, and thus, the bulk-heterojunction (BHJ) morphology (Fig. 2.3ii)) was developed to provide the large interface and became the standard strategy to make efficient OPV devices[8,9]. The concept was first presented by the donor polymer (MEH-PPV) and fullerene acceptor to form a bicontinous network which showed very fast charge transfer kinetics and the PCE being 2.9%[10]. Extra cares have to be taken to optimize the BHJ morphology as it is crucial for efficient charge extraction. This is performed by

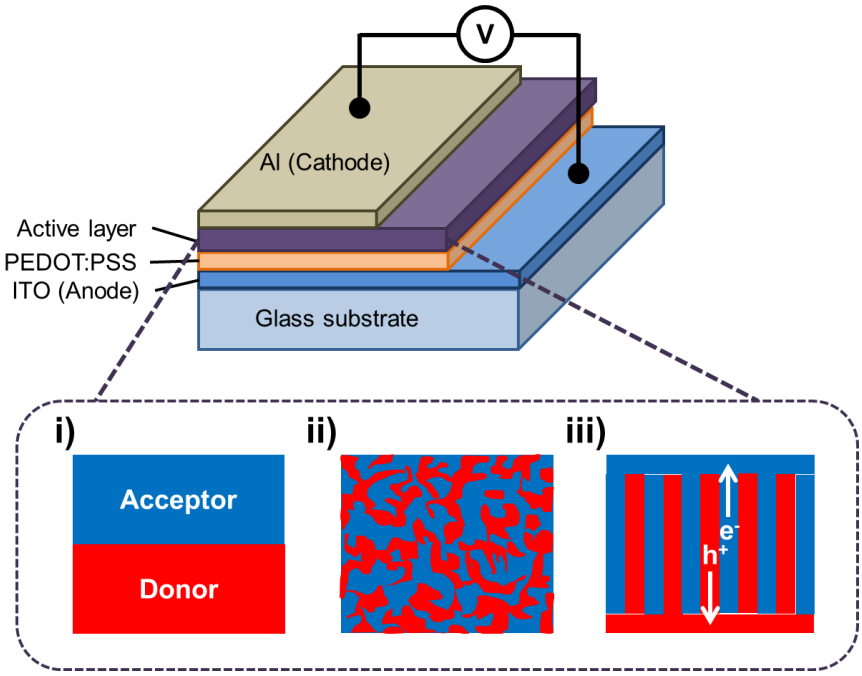

Fig. 2.3 Device structure of conventional OPV device and the active layer morphology: i) donor-acceptor bilayer, ii) bulk-heterojunction (BHJ), and iii) interdigitating morphology.

varying the processing conditions, including solvent system, additives, thermal annealing, and post deposition condition such as solvent vapor treatment. Morphological observation using AFM and TEM is a common method to evaluate the interpenetrating network structure and other advanced method using X-ray and Neutron scattering gives much clearer information about the solid-state structure in molecular level[11-13]. The BHJ film gives the best result so far, but it also produces "dead-end" point where the D-A phase is mixed and not separated or the interpenetrating network is not growing well towards the electrodes. The better morphology of intermixing and ordered nanostructures for charge generation and collection was proposed (Fig. 2.3iii). Attempts have not been successful so far possibly due to the limited understanding to make use of molecular self-assembly to achieve the nanostructures[14]. Solid-state structure of organic materials is stabilized by the weak van der Waals interaction and often forms polymorphic structure (several different modes of

packing structures) depending on processing condition. This intrinsic nature makes it difficult to predict the solid-state structure from the molecular structure. It is imperative to understand the relationship between weak intermolecular interaction and their organized structure in the molecular scale (nm) and in the BHJ blend morphology (μm).

In addition to the morphological consideration, crystallinity is another key feature for the achieving high performance solar cells. It is common phenomena that generated charge carriers are trapped in a film and hence does not reach to electrodes. This recombination process particularly happens when the voltage is high, leads to high charge density, and results in increased recombination probability. In order to obtain a high fill factor (FF) (> 80%), a high charge carrier mobility of around 10^{-2} $cm^2/V \cdot s$ as well as balanced hole and electron mobilities are predicted to be necessary[15-17]. In practice, it is also predicted that the mobility of 7 x 10^{-4} $cm^2/V \cdot s$ and 4 x 10^{-3} $cm^2/V \cdot s$ are at least needed for 100 nm and 300 nm thick devices respectively to avoid significant charge transport losses through the charge recombination mechanism[18]. In the field of organic field effect transistors (OFET), recent progress in materials development and crystallization control led to impressive mobility value of 1–10 $cm^2/V \cdot s$[19,20] and the highest value reached 43 $cm^2/V \cdot s$[21], which is comparable to that of amorphous silicon. The charge transport in the OFET occurs parallel to the interface with the dielectric layer and it is different from that in organic solar cells which charge transport occurs vertically between the electrodes. However, several organic semiconductors was recently reported to have a high mobility value up to 10^{-1} $cm^2/V \cdot s$ in the similar diode configuration[22,23] while a typical BHJ active layer shows the mobility of 10^{-6}–10^{-4} $cm^2/V \cdot s$. This difference indicates the difficulty in achieving both good donor-acceptor morphology and nanostructures for making effective charge transport pathway toward electrodes.

2.3 OPV materials

In order to achieve a high performance solar cell, the design of donor and acceptor molecules used in active layer is very critical. Representative small molecules and polymers are shown in Fig. 2.4. OPV was first fabricated using small molecules such as copper phthalocyanine (CuFc) and fullerene (C60) as the active layers and they were vacuum-deposited in a bilayer film. Since the development of BHJ concept, p-type polymer materials in combination with n-type fullerenes have been widely investigated as they provide the feasibility of

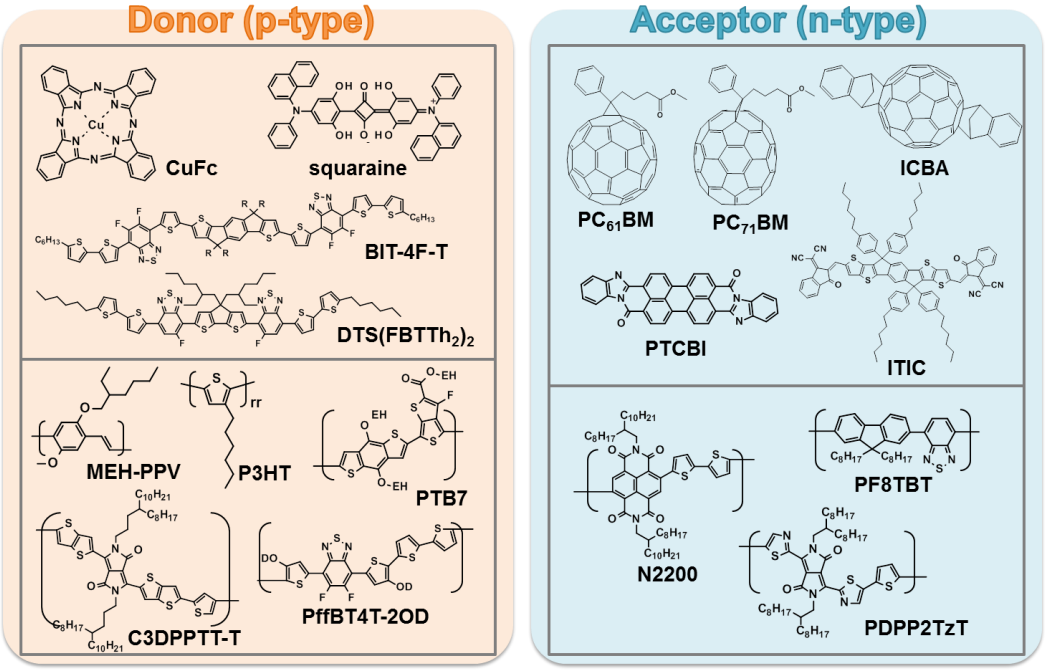

Fig. 2.4 Representative molecular structures of donor and acceptor materials used in active layer (up column: small molecules, down column: polymers)

solution processing. Regio-regular P3HT is the most intensely studied p-type polymer material. With a careful synthetic technique, 3-hexyl thiophenes form polymers in ordered alternating fashion. This regio-regular structure allows them to form close inter-molecular packing structure and red-shifted absorption spectrum, resulting in devices with PCE of more than 5% and a relatively high

EQE value[24-26]. Subsequently, the next major breakthrough in polymeric material comes from donor-acceptor (D-A) (also called push-pull) copolymers such as PTB7[27]. Unlike homopolymer such as P3HT, D-A copolymers tend to form quinoidal structure, where resonance structure of $D^{\delta+}$–$A^{\delta-}$ increases the double bond character in the polymer backbone. This feature leads to the effective modification of HOMO/LUMO level by changing the donor and the acceptor component of corresponding polymeric structures. Molecular engineering of backbone structure, side chains, and other form of substitution has developed a class of successful p-type polymers. The device efficiency after optimization effort of fabrication condition and device structure achieved over 10% of PCE.

Recently, small molecular material has attracted attention for photovoltaic application again. G. Bazan and co-workers has developed molecular donor materials having the D_1-A-D_2-A-D_1 structure with a long alkyl chain side groups, thus enable them to be solution processible. Polymeric materials have intrinsic structural uncertainty and often result in the batch-to-batch difference. Thus, there is added complication when it comes to molecular designing of polymeric materials and they often adopt a trial-and-error approach. This often hampered rational material designing. Small molecules have defined structure and high purity, which will allow for consistency in the material development. Some small p-type materials together with n-type fullerenes in OPV device have shown PCE of 10%[28,29]. There has also been some development in n-type materials. One such example is a class of n-type materials, ITIC, together with p-type polymer in OPV device demonstrated remarkable 11% of PCE[30]. This result is the clear differences from those of the n-type polymer materials, which have been studied for a long time, but have shown moderate efficiency, due to the limitation of material arise from synthetic difficulties to make electron deficient aromatic backbone. The versatility of small mo
lecular materials allows sophisticated structural engineering. It would be

possible to carry out rational molecular designing through the understanding of the structure/property relationship of these active OPV materials.

Reference:

[1] A.J. Heeger, *Reviews of Modern Physics* 73 **(2001)** 681.

[2] V. Coropceanu, J. Cornil, D.A. da Silva Filho, Y. Olivier, R. Silbey, J.-L. Brédas, *Chem Rev* 107 **(2007)** 926.

[3] L. Wang, G. Nan, X. Yang, Q. Peng, Q. Li, Z. Shuai, *Chem Soc Rev* 39 **(2010)** 423.

[4] V. Balzani, A. Juris, M. Venturi, S. Campagna, S. Serroni, *Chem Rev* 96 **(1996)** 759.

[5] H. Dong, X. Fu, J. Liu, Z. Wang, W. Hu, *Adv Mater* 25 **(2013)** 6158.

[6] Y. Diao, K.M. Lenn, W.-Y. Lee, M.A. Blood-Forsythe, J. Xu, Y. Mao, Y. Kim, J.A. Reinspach, S. Park, A. Aspuru-Guzik, G. Xue, P. Clancy, Z. Bao, S.C.B. Mannsfeld, *J Am Chem Soc* 136 **(2014)** 17046.

[7] C.W. Tang, *Applied Physics Letters* 48 **(1986)** 183.

[8] B. Kraabel, C.H. Lee, D. McBranch, D. Moses, N.S. Sariciftci, A.J. Heeger, *Chemical Physics Letters* 213 **(1993)** 389.

[9] J.J.M. Halls, C.A. Walsh, N.C. Greenham, E.A. Marseglia, R.H. Friend, S.C. Moratti, A.B. Holmes, *Nature* 376 **(1995)** 498.

[10] G. Yu, J. Gao, J.C. Hummelen, F. Wudl, A.J. Heeger, *Science* 270 **(1995)** 1789.

[11] Y. Huang, E.J. Kramer, A.J. Heeger, G.C. Bazan, *Chem Rev* 114 **(2014)** 7006.

[12] N.C. Miller, E. Cho, M.J. Junk, R. Gysel, C. Risko, D. Kim, S. Sweetnam, C.E. Miller, L.J. Richter, R.J. Kline, M. Heeney, I. McCulloch, A. Amassian, D. Acevedo-Feliz, C. Knox, M.R. Hansen, D.

Dudenko, B.F. Chmelka, M.F. Toney, J.L. Bredas, M.D. McGehee, *Adv Mater* 24 **(2012)** 6071.

[13] J.-T. Chen, C.-S. Hsu, *Polymer Chemistry* 2 **(2011)** 2707.

[14] M. Wang, F. Wudl, *Journal of Materials Chemistry* 22 **(2012)** 24297.

[15] J.A. Bartelt, D. Lam, T.M. Burke, S.M. Sweetnam, M.D. McGehee, *Advanced Energy Materials* 5 **(2015)** n/a.

[16] A.J. Heeger, *Adv Mater* **(2013)**.

[17] C.M. Proctor, J.A. Love, T.-Q. Nguyen, *Adv Mater* 26 **(2014)** 5957.

[18] D. Neher, J. Kniepert, A. Elimelech, L.J. Koster, *Sci Rep* 6 **(2016)** 24861.

[19] H. Sirringhaus, *Adv Mater* **(2014)**.

[20] W. Wu, Y. Liu, D. Zhu, *Chemical Society Reviews* 39 **(2010)** 1489.

[21] Y. Yuan, G. Giri, A.L. Ayzner, A.P. Zoombelt, S.C.B. Mannsfeld, J. Chen, D. Nordlund, M.F. Toney, J. Huang, Z. Bao, *Nat Commun* 5 **(2014)**.

[22] Y. Li, T. Dutta, N. Gerasimchuk, S. Wu, K. Shetye, L. Jin, R. Wang, D.-M. Zhu, Z. Peng, *ACS Appl Mater Interfaces* 7 **(2015)** 9372.

[23] Y. Li, R.G. Clevenger, L. Jin, K.V. Kilway, Z. Peng, *The Journal of Physical Chemistry C* 120 **(2016)** 841.

[24] G. Zhao, Y. He, Y. Li, *Adv Mater* 22 **(2010)** 4355.

[25] J.Y. Kim, S.H. Kim, H.H. Lee, K. Lee, W. Ma, X. Gong, A.J. Heeger, *Adv Mater* 18 **(2006)** 572.

[26] W. Ma, C. Yang, X. Gong, K. Lee, A.J. Heeger, *Advanced Functional Materials* 15 **(2005)** 1617.

[27] Z. He, C. Zhong, S. Su, M. Xu, H. Wu, Y. Cao, *Nat Photon* 6 **(2012)** 591.

[28] J.-L. Wang, Q.-R. Yin, J.-S. Miao, Z. Wu, Z.-F. Chang, Y. Cao, R.-B. Zhang, J.-Y. Wang, H.-B. Wu, Y. Cao, *Advanced Functional Materials* 25 **(2015)** 3514.

[29] K. Sun, Z. Xiao, S. Lu, W. Zajaczkowski, W. Pisula, E. Hanssen, J.M. White, R.M. Williamson, J. Subbiah, J. Ouyang, A.B. Holmes, W.W. Wong, D.J. Jones, *Nat Commun* 6 **(2015)** 6013.

[30] W. Zhao, D. Qian, S. Zhang, S. Li, O. Inganäs, F. Gao, J. Hou, *Adv Mater* 28 **(2016)** 4734.

Chapter 3

Experimental Methodology

In order to conduct aims and purpose of this PhD study, appropriate methods and models were selected and used to investigate material properties. Novel small molecular donor materials were synthesized and characterized their basic properties. They were then incorporated into photovoltaic devices and evaluated the performance. Principles of solar cell operation and measuring instruments were explained for a solid comprehension of the results and outcomes. Charge transport properties were evaluated using SCLC configuration and field-effect transistor devices so as to estimate the vertical and horizontal charge carrier mobility, respectively. Several X-ray diffraction techniques were used to investigate structural information of samples in different states. Interaction of X-ray with matters was explained. Different machine configurations were justified with the solid state structures of materials. Thermodynamics of polymorphic crystals was also presented to guide a qualitative understanding of the molecular self-assembly.

3.1 Synthesis and Characterization

3.1.1 Material

Materials used in this thesis were purchased from commercial sources except for synthetic molecules specified in each chapter. All reagents including solvents were used as received without further purification unless it is mentioned.

3.1.2 Synthesis and Characterization

General organic synthesis techniques were used to obtain final products. Synthetic schemes were described and explained in each chapter. The product was confirmed and fully characterized by several methods such as thin layer chromatography, MALDI-TOF MS, and 1H-NMR. As for novel compounds, further characterization with 13C-NMR and Elementary analysis were conducted. Detailed synthetic procedures and characterization data were shown in Appendix chapter.

3.2 Solar cell operation principle and device characterization

3.2.1 Charge generation and collection

Understanding photovoltaic mechanism in molecular level is important to design new efficient photovoltaic materials. Decades of research works revealed the phenomena and kinetics of photogeneration procedure. The principle mechanism of photogeneration takes place in the active layer of OPV device as follows: light absorption, exciton diffusion, exciton dissociation, charge collection (Fig. 3.1).

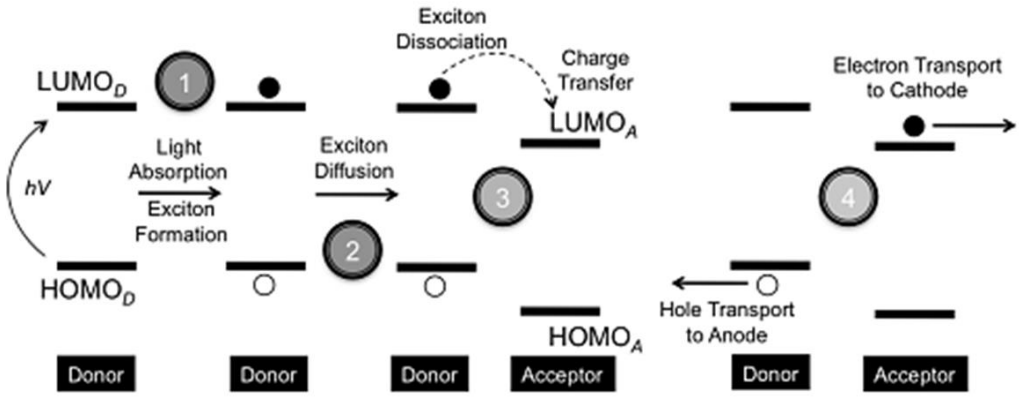

Fig. 3.1 Principle mechanism of photogeneration process occurring between donor and acceptor molecules[1]

(1) Light absorption and exciton formation

When the donor or acceptor molecules absorbs light, electron is excited from the highest occupied molecular orbital (HOMO) to the lowest unoccupied molecular orbital (LUMO). Electron in LUMO and vacant state in HOMO (hole) forms a loose coulombic pair (exciton) and migrate through the solid-state structure. Electronic state of organic molecules strongly bind to molecular orbital and the dielectric constant is low (3-3.5). Thus the generated excitons have a large exciton binding energy (0.1-1.0 eV) and are restricted within the unit cell, which are categorized to Frenkel excitons. This is a clear contrast with excitons generated in inorganic and hybrid type material which forms Wannier-Mott excitons having a low exciton binding energy of a few 10 meV, resulted in exciton dissociation instantly by ambient temperature and formation of free charge carriers.

(2) Exciton diffusion

Since the generated excitons in organic semiconductors have a high coulombic binding forces, they need to migrate to Donor-acceptor (D/A) interface and energy offset of HOMO and LUMO to dissociate the pair into charge carriers;

otherwise, the energy deactivates into thermal energy. The exciton diffusion length L_D is modeled with the equation:

$$L_D = (D\tau)^{1/2}$$

where D is the diffusion coefficient and t is the exciton lifetime. Major exciton generated is a singlet exciton generally has a short life time of less than 1 ns and the diffusion length is limited to less than 20 nm. Consequently, the morphology required to efficient OPV is the bulk-heterojunction film with average donor and acceptor domains with this range. Too small domain size gives detrimental effect as high rate of charge recombination takes place. Too large domain size is neither harmful as it does not provide effective D/A interface and results in loss of energy through thermal deactivation.

(3) Exciton dissociation and charge transfer

The internal electric field at D/A interfaces provides internal electric field the potential gap of which can be used to dissociate excitons. The exciton dissociation occurs through two steps, namely charge transfer state (CT) and the charge separated state (CS). Given exciton generated in donor molecules (D), excitons (D^*) go down to energetically stabilized CT state (D^+A^-) in the D/A interface in the presence of acceptor molecules (A). This close cationic and anionic charges needs to separate away into CS state ($D^+\cdots A^-$) for a good charge transport. However, the energy in CT state also has possibility to decompose into ground state through emitting heat, called charge recombination. Thermodynamics and kinetics determines the reaction direction. If the CS states are more thermodynamically stable and kinetically favorable, the excitons can be separated into holes, which stay in the donor domains, and electrons, which are transferred into the acceptor domains. In order to increase the efficiency of exciton dissociation, the amount of D/A interfaces has to be

maximized. Optimization of the morphology is a crucial part and often time-consuming step to make an efficient OPV device.

(4) Charge transport and collection at the electrodes

After the charge separation, the holes transport to the anode and the electrons to the cathode. Both charges move in the opposite direction due to the internal build-in potential attributed to the difference in the energy band position of interlayer and the work functions of both electrodes. The efficiency of the charge transport strongly depends on the charge mobility value. Under a certain electric field, charge carriers transport toward the direction along electric field but it has always chances of charge recombination. Given the life time as τ, the transportation behavior is described as the following equation:

$$\tau = \frac{\mu \cdot m^*}{q}$$

where q is a unit charge and m^* is the effective mass which is the intrinsic value to semiconducting material. According to the equation, the life time and the mobility are proportional, and thus, higher the mobility value has a high chance of charge collection at electrodes. The carrier mobility depends on the order of material in the solid state. Typically, amorphous organic semiconductor with low degree of order has low charge mobility ranging from 10^{-6} to 10^{-3} $cm^2/V \cdot s$[2], while highly crystalline material exhibit higher mobility by a few orders of magnitude. In bulk heterojunction devices, donor and acceptor phases are mixed with each other and it is crucial to engineer a good percolation pathway for both holes and electrons. The balance between hole and electron mobility values also affects the device performance. Unbalanced both mobility values eventually have charge carriers accumulated in a side of electrode, resulting in charge recombination at the concentrated area. The blend morphology needs to be optimized elaborately by changing device fabrication parameters. The blend composition, the choice of solvent, and additives used to spincoating have large

influence on the nanoscale morphology. Post-treatments such as thermal annealing and solvent vapor annealing can be also applied after the film formation and/or metal electrode deposition.

3.2.2 Device fabrication

Solar cell devices were fabricated using the following steps. After the ITO-coated glass substrates were sequentially cleaned by ultrasonication for 15 min in Hellmanex solution, acetone and isopropyl alcohol, they were plasma-cleaned for 15 min. Then, PEDOT:PSS (Clevios P Al 4083, filtered at 0.45 um PVDF) was spin-coated onto the cleaned ITO substrates at 3000 rpm for 60 sec to obtain a ca. 30 nm thick layer. After transferring the substrates into the glovebox containing a N_2 atmosphere, they were annealed at 140 °C for 10 min. Active layer was prepared by dissolving the donor material and $PC_{71}BM$ (1:3 wt/wt ratio, 15 mg/mL in anhydrous chloroform:oDCB = 9:1 mixed solution, filtered at 0.20 um PTFE), followed by spin-coating onto the PEDOT:PSS on ITO at 1500 rpm for 90 sec, resulting in a film of ca. 100 nm thickness as determined by surface analyzer. 0.2 mg/ml PDMS in chloroform solution was used instead of pure chloroform in the case of PDMS treated film. After drying inside glovebox for 1h, the TiOx solution was spin-coated on the active layer at 2000 rpm for 60 sec, and then subjected to oxidization for 40 min in air. Al electrode (ca. 100 nm) was thermally evaporated at low pressure ($<1 \times 10^{-6}$ Torr) and the complete device with an active area of 0.07 cm2 was obtained.

3.2.3 Current density–Voltage measurement

The performance of solar cells is evaluated by photocurrent density–photovoltage (I-V) curves. A typical I-V curve is depicted in Fig. 3.2. When it comes to evaluate solar cell performance using the I-V measurement, four important parameters need to be determined. 1) Open-circuit voltage (V_{oc}) is the

cell voltage measured when current is equal to zero. 2) Short-circuit current (I_{sc}) is the cell photocurrent measured at zero voltage. 3) Fill factor (FF) evaluates the cell's quality as a power source and is defined as the ratio of the maximum power output (P_m) to the product of I_{sc} and V_{oc}:

$$FF = \frac{I_m \times V_m}{I_{sc} \times V_{oc}}$$

where I_m and V_m represent the current and voltage corresponding to the Pm, respectively. 4) Photoconversion efficiency (PCE) is the energy conversion ratio of photons to electricity, and is defined as the ratio of obtained power from cell operation, Pm, to the incident radiation power (P_{in}) on the solar cell:

$$PCE = \frac{P_m}{P_{in}} = \frac{I_{sc} \times V_{oc} \times FF}{P_{in}}$$

Typically, solar spectrum of AM1.5G (100 mW/cm2) is used as the incident light source. Shockley and Queisser calculated the theoretical maximum power conversion efficiency based on assumption of the balance between both excitation and radiative recombination, and they were able to derive a 33 limit in PCE for any type of single junction solar cells[3].

.2.4 Quantum efficiency measurement

The Quantum Efficiency (QE) is a measure to evaluate the efficiency of the solar cell device. This can be calculated by taking the ratio of the number of carriers collected by the solar cell to the number of photons exposed to the cell at each wavelength of incident light. The QE of 100% indicates the energy from incident light converts to electricity at quantitative ratio. However the photon energy can be lost in devices by various mechanisms such as charge recombination and thermal deactivation. In addition, the actual device is unable

to utilize all of energy from incident light due to the optical loss such as light transmission and reflection. Taking all factors into consideration, External Quantum Efficiency (EQE) can be calculated by the following equation:

$$EQE\ (\lambda) = \frac{hc}{q\lambda}\ SR(\lambda)$$

where h is a Plank's constant, c is a speed of light, q is an elementary charge, l is a wavelength, and SR(λ) is a spectral response (A/W). The spectral response means the ratio of the generated current by the solar cell to the power incident to the solar cell at each wavelength. The calibrated standard silicon solar cell is used to calculate the constant at each wavelength and used as a reference compared to testing devices.

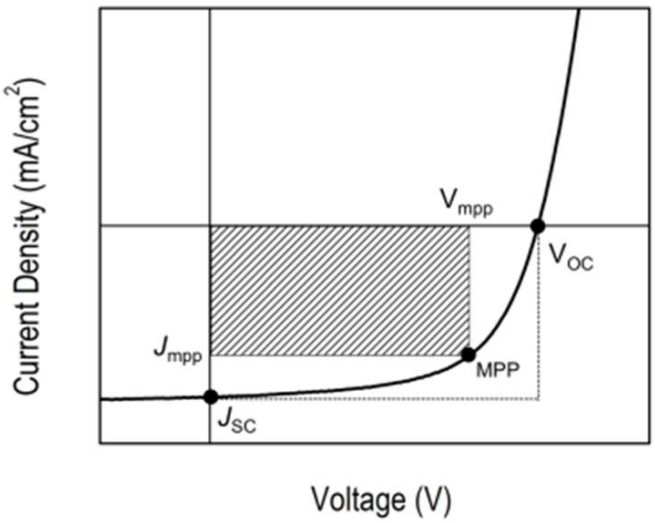

Fig. 3.2 Current density–Voltage (I-V) curve of typical OPV devices

3.3 Hole measurement

Ever since the demonstration of possible electric applications with organic materials[4], electrical properties have been investigated and reported in considerable amount of papers. Under a certain electric field E, current goes through a material is simply described as follows:

$$J = \sigma E$$

where J is the current density, E is the electric field, and σ is the electronic conductivity (S/m) or equivalent to the inverse of the electronic resistivity. Phthalocyanine is one of early examples which showed a high conductivity of 10^{-1} – 10^{-2} S/cm depending on temperature. The electric conductivity S is given as a sum of hole mobility (μ_h) and electron mobility (μ_e) as follows:

$$\sigma = \mathrm{e}(\mathrm{n}\mu_e + p\mu_h)$$

where e is the unit electron charge, n and p are the density of mobile electrons and holes in medium, respectively. These hole and electron mobility is the primary parameter to determine the electron conductivity of materials. The mobility value is depending on the electronic structure of molecules, the self-assembly structures and possibly perturbed by excessive amount of impurities, structural defects, boundaries. Novel organic materials aiming for electronic application need to fulfil a certain criteria depending on the application such as $>10^3$ $cm^2/V{\cdot}s$ for silicon and germanium replacement in semiconductor devices, 1-100 $cm^2/V{\cdot}s$ for amorphous silicon replacement , and 0.01-10 $cm^2/V{\cdot}s$ for solar cell applications[5]. It is imperative to predict and assess the mobility value, and thus, a variety of measurement techniques with each dynamic range, sensitivity, and configuration has been developed. In this PhD study, The hole-only device applied in SCLC model and the field-effect

transistor (FET) device were used to measure the hole mobility of novel organic materials.

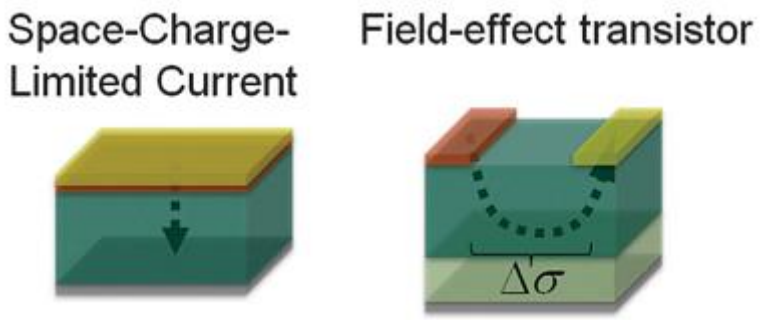

Fig. 3.3 Picture of device configuration for dark current measurement in SCLC model and field-effect transistor

3.3.1 SCLC model

The space-charge limited current is the current regime which current is dominated by charge carriers injected from the contacts and the current-voltage characteristics becomes quadratic ($I \propto V^2$). Trap states are always present in material, and thus, a bias voltage high enough to exceed the trap-filled-limit is necessary to model the I-V curve. Under the condition, the current is only dependent on the mobility and no more depends on the charge carrier density, hence, the mobility can be estimated from a simple current-voltage measurement. In order to calculate the hole mobility of materials, hole-only devices are made with the device structure of ITO/PEDOT:PSS/film material/Au. In this configuration, charge carriers transport vertically to electrodes similar to solar cell devices. The Mott-Gurney SCLC equation combined with field dependent mobility was used as described in detail in literatures[2]. A simplified form of SCLC model enhanced by the Frenkel effect are given by the following equation[6]:

$$J = \frac{9}{8}\varepsilon_0\varepsilon_r\mu_0 \exp\left(0.89\beta\sqrt{\frac{V - V_{bi}}{L}}\right)\frac{(V - V_{bi})^2}{L^3}$$

where J is dark current density, ε_0 is the vacuum permittivity, ε_r is the relative permittivity of material (ca. 3 for organic material), μ_0 is the hole mobility at zero field, β is the field activation factor, L is thickness of thin film. The internal potential is obtained by subtracting the built-in potential V_{bi} from the applied voltage V. The V_{bi} is calculated to 0.1 as the work function of PEDOT:PSS is -5.2 V and that of Au is -5.1 V.

3.3.2 Organic field-effect transistor

With the device structure depicted in Fig. 3.3, the FET can evaluate charge carrier mobility in which charges go parallel to the substrate. The transistor is a three-terminal component consisting of gate, drain, and sources. The current flow between source and drain and is controlled by the bias applied from the gate. FET has several configurations depending on their relative position of contacts and the dielectric/semiconductor layer. The bottom-gate and bottom-contact device was made on n++-Si substrates acting as a common gate. A 500 nm thermally grown oxide layer, passivated with hexamethyldisilazane (HMDA) was used as gate dielectric and Gold source and drain electrodes with a thickness of 50 nm on a 15 nm Ni adhesion layer were defined by photolithography. In this devices, negligible source-drain current (I_{SD} = 0) flows when the gate voltage is zero (V_G = 0) independent of the bias applied between the source and the drain contacts (V_{SD}). The device turns on when the gate voltage is applied between source and gate ($V_G \neq 0$) which induce the electric field and subsequently charge careers in the interface with the dielectric layer; a negative bias voltage induce cationic charges in the semiconductor interface. Depending on a bias voltage between source and drain (V_{SD}), the

electrical path is created and the current (I_{SD}) flows. The transistor's performance is evaluated from the output and transfer current–voltage plots, from which critical parameters such as the charge carrier mobility (μ), current on/off ratio (I_{on}/I_{off}), threshold voltage (V_{th}) are measured. Output characteristic is obtained under a fixed V_G by measuring I_{SD} in the sweep of V_{SD}. The I_{SD} increases linearly with the V_{SD} and is saturated at a high voltage in an ideal case. On the other hand, when V_{SD} is fixed in the saturation region, I_{SD} increases super-linearly (amplified current) with V_G, showing a transfer curve characteristic. Using the I-V response in the saturated condition, charge carrier mobility can be extracted with fitting I-V curve with the standard FET model[7] below:

$$|I_{SD}| = \frac{WC_i}{2L}\mu_{FET}(V_G - V_{th})^2$$

where W is the channel width, L is the channel length, C_i is the capacitance per unit area of the dielectric layer. The value of W should be much longer than L to suppress the contribution of curvature current.

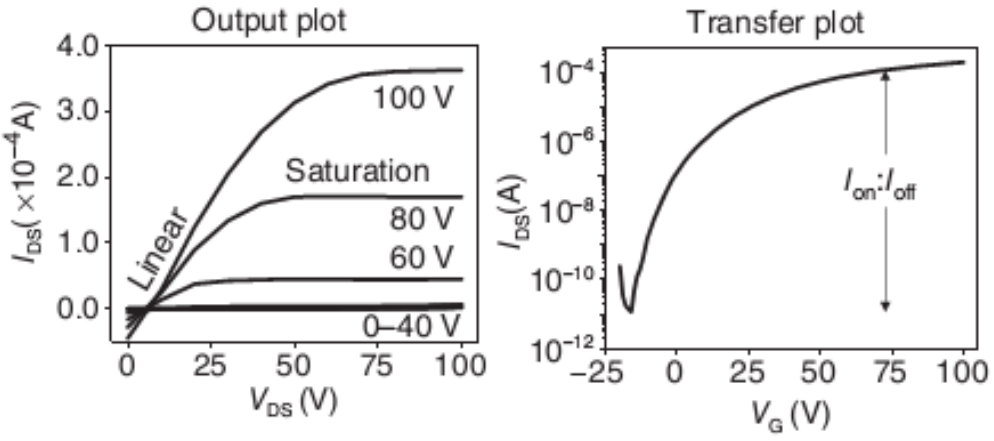

Fig. 3.4 Output characteristic and Transfer characteristic of OFET devices

3.4 X-ray diffraction and characterization

X-rays are electromagnetic waves with the wavelength ranging from 0.01 nm to 10 nm, or it can be also described as beams of photons with tassociated energy. X-ray can interact with matter and gives us detailed structural information of substance which is impossible to see with our bare eyes. It is a useful tool applied in many field of chemical, biological, and material sciences and has contributed to visualize nano-scale atomic structure such as the helical structure of DNA, absolute conformation of molecules, and the folding structure of proteins. On top of this, it can be used to analyse quantitative structural information of materials such as phase transition behavior, crystalline quality, orientation, and internal stress. This is made possible as a consequence of the interaction between X-rays and matter. X-rays with wavelengths below 0.1–0.2 nm are called hard X-rays, while those with longer wavelength are called soft X-rays. Hard X-rays are widely used to conventional structural analysis because it can deeply penetrate into substances and give strong intensity. On the other hand, soft X-ray can be easily absorbed in air and gives information mainly on the surface of sample. The hard X-rays have wavelengths of about one Å, similar to the size of atomic radius. Thus, it can be especially suitable to analyse atoms periodically arranged within the substance. X-ray coherently interact with electrons in atoms, hence the lighter atoms such as C, N, O, main constituents of organic molecules, have a low scattering cross section with hard X-ray. Soft X-ray can use the photon energy close to core absorption edge of those atoms to see the resonant enhancement sensitive to specific bond energy. This is highly sensitive to organic materials and gives useful information of BHJ blend morphology and in-situ crystallization behavior of span-cast film[8].

3.4.1 Bragg's law

In a consequence of the three dimensional ordered atomic arrangement in the solid state, coherent scattering of X-rays at atom sites results in constructive interference which scatters at a certain well-defined angles. This effect is similar to the diffraction of visible light interacting with a prism. X-ray also has a wavelength depending on the cathode material used in X-ray tube (0.0709 nm for Mo and 0.157 for Cu $K_{\alpha 1}$ X-ray source). When it comes to a crystal with ordered structures, it can be seen as a three dimensional grating with a spacing of a few Å. The diffraction can be observed when the wavelength of the incoming X-ray photon is the similar to the spacing size. In 1913, W.H. Bragg and W.L. Bragg described diffraction and interference of X-rays in a crystal which were then seen as reflections from the atomic planes in the crystal lattice. The positions of the reflections are calculated using the difference in optical path length and the neighbouring interplanar spacings. This follows the equation below;

$$2d\ sin\theta = n\lambda$$

where d is interplanar spacing, theta is the angle, n is order of the interference (n = 1,2,3...), and λ is wavelength of the beam (see Fig. 3.5). With known X-ray wavelength and obtained angle, peak patterns with various d-spacing values are obtained. This pattern and the intensity have structural information corresponds to a certain Millar indices and the crystal lattice parameters as well as symmetricity.

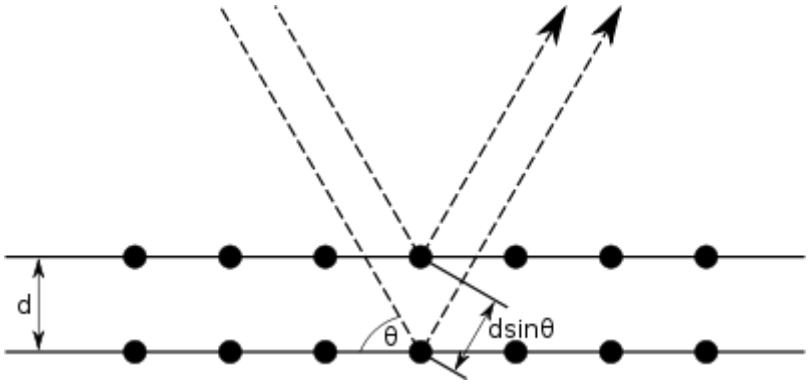

Fig. 3.5 Graphical representation of Bragg's law

3.4.2 Single crystal X-ray diffraction and powder X-ray diffraction

In single crystal X-ray diffraction, a crystal sample is rotated around various axes of machine set up in order to find a large number of different reflections. A three dimensional ordered structure of molecules diffracts X-ray so as to satisfy the Bragg's law and symmetricity rule (Fig. 3.6 left). Each spots can be assigned as indices by calculating the position from angle of incident X-ray beam. The atomic arrangement within the crystal, or the crystal structure, can be determined from the angular positions and the intensity of these reflections. A four-circle goniometer is required in order to observe all possible reflections.

In X-ray powder diffraction, the powder sample consists of large number of small crystallites, ideally randomly oriented with respect to each other. Because the X-ray diffraction comes from all orientation, the shape becomes a cone like shape with angle of theta (Fig. 3.6 right). The circular shape (Debye scherrer ring) is detected on sensor. If the polycrystalline domains have a favorable orientation (i.e. fibrous crystal growth), the scattered shape is not a perfect cone but become a set of scattered points on a circle of the cone. A powder diffractogram is obtained by integrating the detected intensity as a function of the angle between the incident beam and the diffracted beam.

In thin-film configuration in which the incident beam position is fixed to the critical angle of substrate, the diffraction pattern holds the information of anisotropy in the structure. Using two-dimensional detector, the orientation of molecules such as “edge-on” and “face-on” configuration can be revealed.

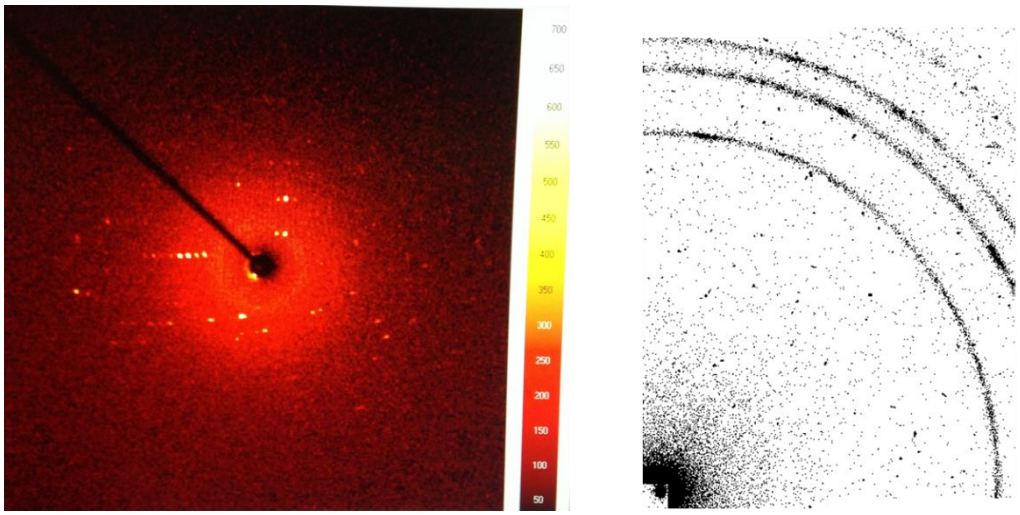

Fig. 3.6 Single crystal X-ray diffraction image (left) and powder x-ray diffraction image where incident X-ray beam is irradiated on center and bottom left, respectively

3.4.3 Structural analysis from X-ray diffraction measurements

Diffracted X-rays contain structural information of crystalline orderings in the solid-state (Fig. 3.7a). Thus, the ordering of substances inside the solid can be inferred through analysing detected peaks. With respect to crystals having a three-dimensional structure, the direction of diffracted beam extends over the three-dimensional space, and thus in order to collect peaks, single crystal X-ray diffraction measurement is used. In the subsequent analysis in single crystal X-ray crystallography, higher diffraction intensity increase accuracy of the analysis. A sufficiently large single crystal is usually necessary for this reason, and hence substances that are difficult to crystallize do not suit to this analysis.

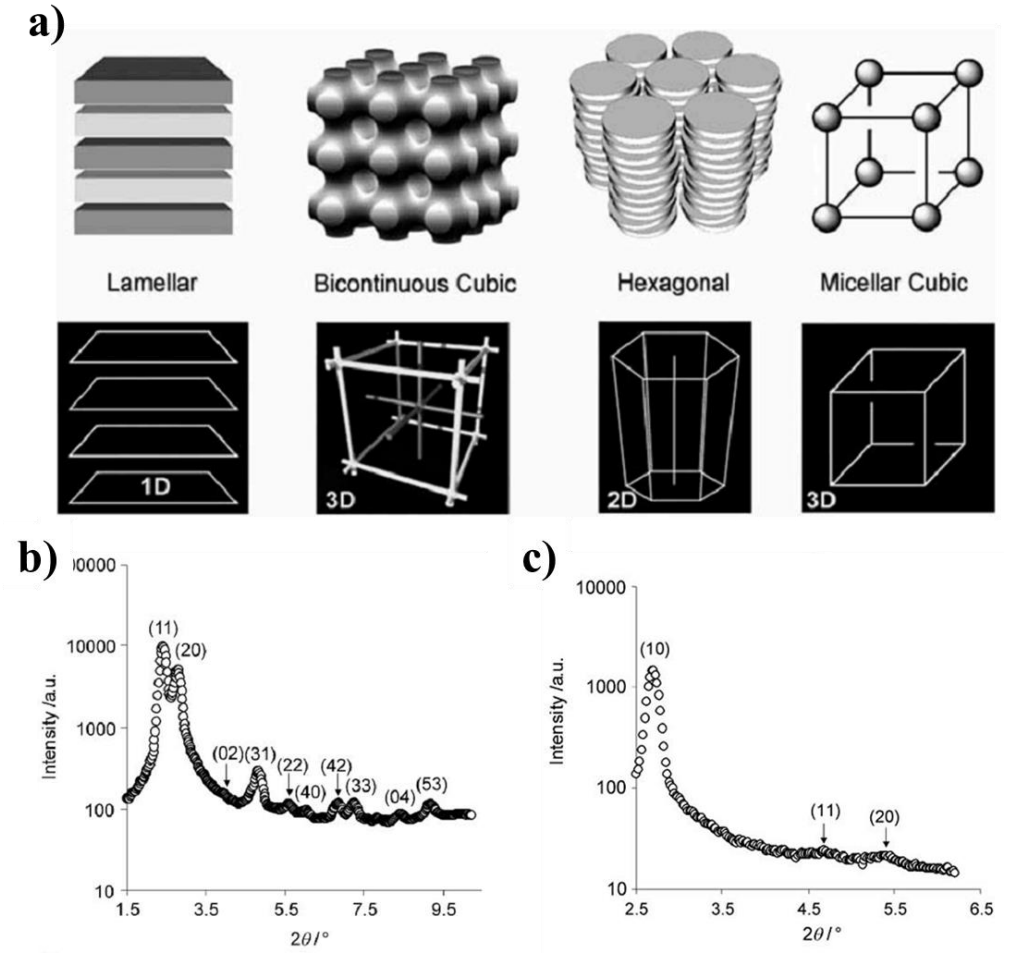

Fig. 3.7 a) The relationship between condensed phase structures and crystalline ordering[9]. (b, c) Small angle X-ray scattering (SAXS) of columnar liquid crystals b) Col (rectangular) phase P2/a and c)Col (hexagonal) phase P6/mmm[10].

On the other hand, samples having one- or two-dimensional ordering are less complex and powder X-ray diffraction measurement can be used to identify the structure in some cases. As to one-dimensional structures, lamellar structures of amphiphilic lipids and smetic phases of liquid crystals are well known. Diffraction peaks from these one-dimensional layered structures appear as a repeated pattern corresponding to distance between layers such as (10), (20), (30)... in Millar indices of (hk). As examples of two-dimensional structures,

columnar liquid crystals tend to form the tetragonal phase and hexagonal phase. Structural analysis of these structures is somewhat more complicated than that of one-dimensional structures. In addition to larger number of peaks, some peaks disappear due to the relationship between crystal symmetry and Millar indice (systematic absences). In Fig.3.7 (b) and (c) which are small angle X-ray scattering patterns, peaks corresponding to a certain spacing distance with Millar indices of (hk) are missing. On the other hand, analysing combined information of the diffraction angle (distance), intensity and Millar indices of missing/appearing peaks, each phase can be identified such as the case of columnar rectangular (b) and columnar hexagonal (c). Furthermore, given the size of constituent molecules and atoms, their structure and alignment in the solid state can be inferred.

3.4.4 Polymorphism

From a thermodynamic standpoint, the relationship among crystal polymorphs and melted liquid state can be illustrated using an energy-temperature diagram. An example of a reversible solid-to-solid phase transition system is shown in Fig. 3.7. In the diagram, the Gibbs free energy G and enthalpy H has a relationship following the equation;

$$G = H - TS$$

where T is temperature and S is entropy. In the diagram, Tp, mpI, and mpII represent the phase transition temperature of phase I/phase II, phase I/melt, phase II/melt, respectively. Materials form the most stable phase of which the Gibbs free energy has the lowest energy state. At absolute zero temperature, Gibbs free energy and enthalpy are equal because entropy term is negligible; entropy represents the degree of motion in system and it freezes at the absolute zero. On increasing temperature, the entropy terms, which are described as the

slope of curves, become significant. The Gibbs free energy comes with cross over at a temperature and the phase transition takes place. The system in the fig. 3.7 favors phase I in low temperature. On increasing temperature, phase transition to phase II. and eventually melt to liquid phase. This can reversibly take place as there several cross over points. This type of phase transition, having a transition temperature below the melting point, is known to the enantiotropic phase transition. Another polymorphic system which has the Gibbs free energy crossover above melting point is also common. In this case, one polymorph remains the stable form over the entire temperature range up to the melting point. The phase transition from metastable polymorph to the most stable polymorph takes place irreversible when they are accessible which cannot simply explained by temperature, and it is called the monotropic phase trantion. It is seen that the defect sites and eternal stimuli involve in the process. In differential scanning calorimetry (DSC), latent heat involved in the phase transitions can be detected. This corresponds to the difference in enthalpy (ΔH) on the diagram. On heating, it represents endothermic peaks for enantiotropic and exothermic peaks for monotropic phase transition.

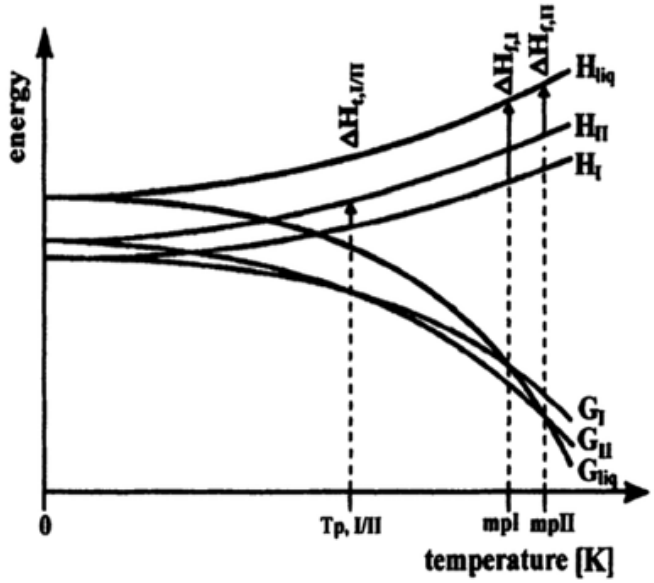

Fig. 3.8 Energy versus temperature diagram of liquid, polymorph I and II to describe the thermodynamics of Gibbs free energy and enthalpy[11]

Reference:

[1] T. Salim, *PhD thesis* NTU **(2011)**.

[2] V. Coropceanu, J. Cornil, D.A. da Silva Filho, Y. Olivier, R. Silbey, J.-L. Brédas, *Chem Rev* 107 **(2007)** 926.

[3] W. Shockley, H.J. Queisser, *Journal of Applied Physics* 32 **(1961)** 510.

[4] A.J. Heeger, *Reviews of Modern Physics* 73 **(2001)** 681.

[5] H. Dong, X. Fu, J. Liu, Z. Wang, W. Hu, *Adv Mater* 25 **(2013)** 6158.

[6] Z.B. Wang, M.G. Helander, M.T. Greiner, J. Qiu, Z.H. Lu, *Journal of Applied Physics* 107 **(2010)** 034506.

[7] S. Seki, A. Saeki, T. Sakurai, D. Sakamaki, *Phys Chem Chem Phys* 16 **(2014)** 11093.

[8] W. Chen, M.P. Nikiforov, S.B. Darling, *Energy & Environmental Science* 5 **(2012)** 8045.

[9] J.W. Goodby, R.J. Mandle, E.J. Davis, T. Zhong, S.J. Cowling, *Liquid Crystals* 42 **(2015)** 593.

[10] M. Kaller, S. Tussetschlager, P. Fischer, C. Deck, A. Baro, F. Giesselmann, S. Laschat, *Chemistry* 15 **(2009)** 9530.

[11] H. Chung, Y. Diao, *Journal of Materials Chemistry C* 4 **(2016)** 3915.

Chapter 4

DTCTT and IDT-based small molecular OPV

A novel donor material, di(HTh2BT)DTCTT, having a dithienocyclopenta-thieno[3,2-b]thiophene (DTCTT) core, was synthesized and used as a molecular donor in small molecular organic photovoltaic device (sm-OPV). DTCTT has a molecular structure similar to indacenodithiophene (IDT) but with a central thienothiophene instead of a benzene, and the effect of the more extended conjugation of the theinothiophene on its optical, thermal and photovoltaic properties was systematically investigated. The di(HTh2BT)DTCTT showed red-shifted absorption (up to 800 nm), a higher HOMO level and greater crystallinity than its IDT analogue. The sm-OPV devices were fabricated by spin-coating a blend solution with $PC_{71}BM$ and showed an encouraging PCE of 2.8% with J_{sc} of -9.3 mA/cm^2, V_{oc} of 0.73 V and FF of 0.42. This is the first report about the molecular donor based on a DTCTT backbone for sm-OPV and it can be seen that this compound has greater potential for achieving high efficiencies compared with its IDT analogue. Structural and morphological analysis indicated that further improvement may be possible by increasing the crystallinity of the blend film.[*]

*This section published substantially as reference:
Y. Abe, H. Li, J. Yin, C. Soci, A.C. Grimsdale, Y.M. Lam: Fused Thieno[3,2-b]thiophene-dithiophene Based Donor Material for Molecular Photovoltaics: Structural Comparative Study with Indacenodithiophene, *J. Mat. Chem. C*., **2016**, 4, 9656-9663

4.1 Introduction

Indacenodithiophene (IDT) is a well-known backbone structure used in OFET and OPV. In the field of OPV, it has been coupled with a variety of acceptor units to form donor-acceptor (D-A) type polymers and these have shown high performance in the power conversion efficiency of device from an early stage of material development[1-3]. One such successful D-A polymers is IDT coupled with a benzo[2,1,3]thiadiazole (BT) unit which, when blended with a fullerene acceptor, produced a very promising power conversion efficiency (PCE) of 6.4 %[4]. Recently, IDT has been incorporated into D_1-A-D_2-A-D_1 type molecules and have been tested in small molecular photovoltaic devices (sm-OPV)[5-7] with promising results[8-10]. In particular a device fabricated with a molecular donor containing units of IDT substituted with solubilizing alkyl side chains on its sp3 carbons and difluorobenzo-[2,1,3]thiadiazole (2FBT) showed a PCE of 8.1 %, which is among the highest values yet reported for a sm-OPV[11]. Furthermore, IDT has also been coupled with electron deficient units in an attempt to make efficient n-type semiconducting materials which might be good candidates to replace fullerene acceptors. Some of them have been mixed with polymer donors and PCEs of 11 % have been achieved[12-15].

These results showed that the IDT structure is a promising building block for further development of OPV materials and thus utilizing the family of other fused ladder-type arenes[16,17] can potentially be the direction for future research in this area. However, it remains to be seen how the structure can influence OPV device performance. Much attention has been paid to the relationship between the solid-state intermolecular interaction, nano-structured morphology and optoelectronic properties of organic materials. Recent attempts at the development of materials for sm-OPV, demonstrated that their solid-state properties vary in a complex fashion with a variety of structural factors such as the presence of hetero atoms[18,19], the nature, position and number of side

chains[20,21], and structure of the backbone [10,22,23]. Systematic investigation is necessary to elucidate the solid-state structure/properties relationships needed for rationally designing an efficient OPV material[6]. Molecular materials are a good candidate for this purpose as they have defined structure unlike polymer materials which have structural uncertainty in important parameters such as the degree of polymerization, the molecular weight distribution and the nature of end groups.

Dicyclopentadithieno-thieno[3,2-b]thiophene (DTCTT) has a similar structure with IDT except that the central benzene is replaced by a thieno[3,2-b]thiophene unit (TT). Polymers based on DTCTT coupled with several acceptor units have been reported for OFET and OPV applications with the highest mobilities and PCEs being 5.3 x 10^{-2} $cm^2/V \cdot s$ and 2.59% for the copolymers benzo[2,1,3]thiadiazole and thieno[3,4-c]pyrrole-4,6-dione respectively[24-26]. The ability to absorb light efficiently over a wide spectral range and a strong electron donating ability as well as the rigid backbone structure is especially advantageous for organic dye used in dye sensitized solar cell and hence high efficiencies of up to 8.9 % have been obtained using these dyes such as C243 dye [27,28]. However, no DTCTT based donor molecule for sm-OPV has yet been reported.

In this chapter, the synthesis and application of novel small molecular donor material for sm-OPV incorporating a DTCTT unit di(HTh2BT)DTCTT, referred as the DTCTT donor in the following discussion, is reported and their properties are compared to the structural analogue di(HTh2BT)IDT, referred as the IDT donor (Fig. 4.1). It is especially interesting to compare the effect of incorporating thienothiophene unit in place of benzene in the molecular structure due to the advantages mentioned earlier. It is expected that this modification will improve the hole mobility of the film, leading to better OPV performance in device. Also, structural analysis of the molecular form will

provide more reliable evidence than the polymer form for the elucidation of the relationship between a molecular structure and the device performance. The structure is based on the conventional D_1-A-D_2-A-D_1 design with DTCTT as the central donor unit, BT units as the acceptors, and bithiophenes as terminal donor moieties. Octylphenyl rings were introduced onto the sp3 carbon of the cyclopentadienes within the DTCTT unit, to simultaneously suppress the strong π–π stacking and increase the solubility. Such aryl substituents will also increase the photostability of the unit as has been demonstrated in bridged phenylene units in OLED materials[29]. The impact of thienothiophene unit in the the DTCTT donor on its optoelectronic properties and the device performance will also be presented. A comparison will be made with the IDT analogue that contains a benzene unit.

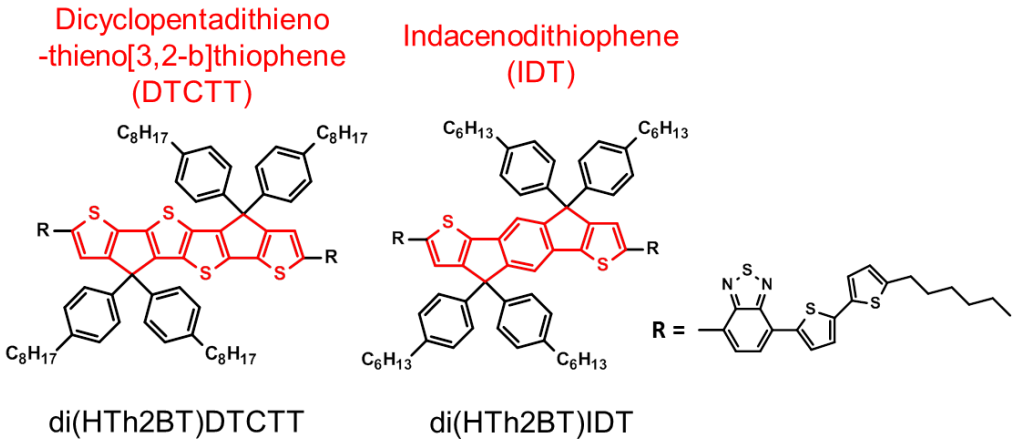

Fig. 4.1 Chemical structure of di(HTh2BT)DTCTT and di(HTh2BT)IDT

4.2 Synthesis

The synthesis of the novel donor molecule is outlined in 4.1. Stille coupling of 4,8-dibromobenzo[2,1,3]thiadiazole and 5-tributylstannyl-5'-hexyl-2,2'-bithiophene produced the intermediate 1. Initially, Stille coupling reaction was used to couple this bromo compound with distannylated-IDT, but the reaction

yield was less than 15%, even after refluxing for more than a day, and protonated IDT compounds were detected in the product mixture. It has been reported that protonation resulting from a metal-halogen exchange reaction can take place during metal catalyzed coupling reactions of thiophenes stannylated at the alpha position[30]. Indeed, distannyl-IDT is very sensitive in acidic media

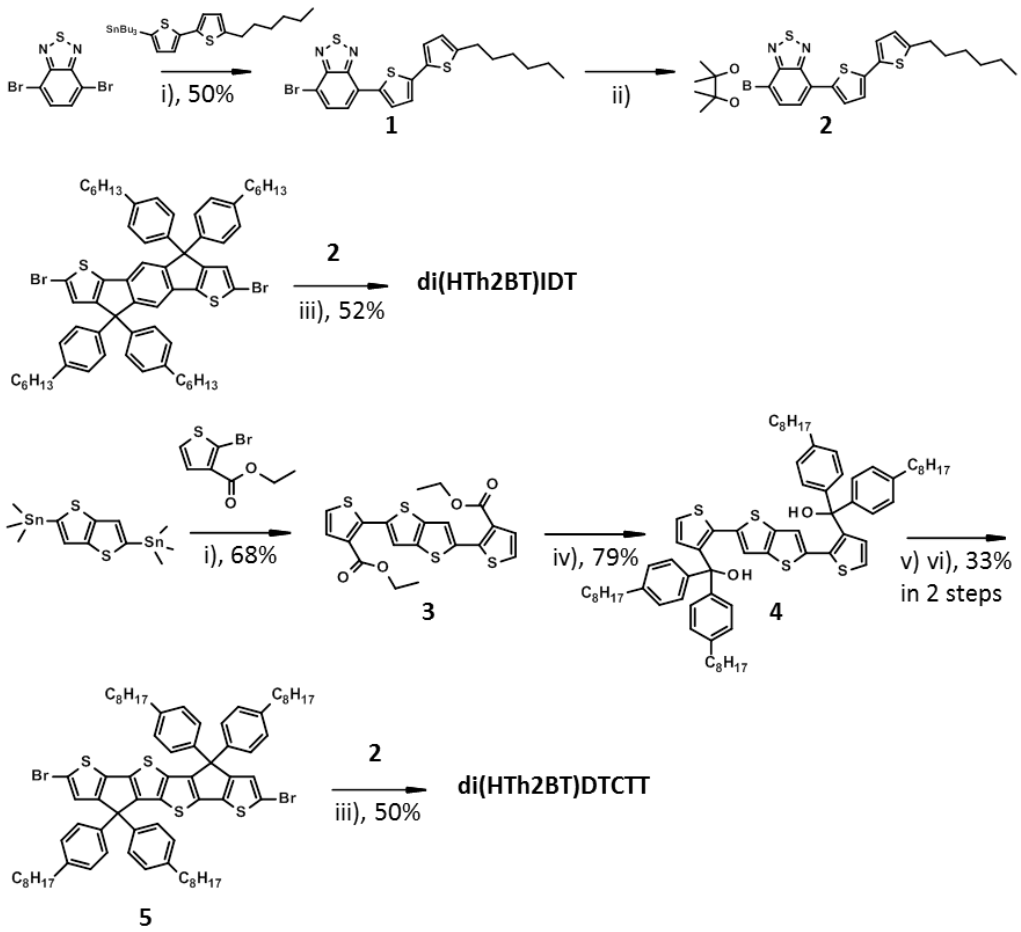

Scheme 4.1 Synthesis of di(HTh2BT)IDT and di(HTh2BT)DTCTT i)$Pd(PPh_3)_4$, Toluene, 80 °C ii)B_2pin_2, $Pd(dppf)Cl_2$, KOAc, Toluene, 80 °C iii)$Pd(PPh_3)_4$, K_2CO_3, THF, 80 °C iv)OctPhMgBr, THF, reflux v)Amberlyst, Toluene, reflux vi)NBS, Chloroform, 0 °C

such as chloroform, which produce partially protonated compounds. To promote this Stille coupling, microwave irradiation might be able to help to complete the reaction before protonation can occur but with no guarantee of success as the exchange reaction might also be accelerated by the microwave irradiation[31]. Instead, Suzuki coupling between dibromo-IDT and compound 2 was carried out. The bromo group compound 2 was transformed to a pinacol boronate by the Suzuki-Miyaura borylation reaction. This reaction was almost complete within 1 h and the dark purple powder of the IDT donor was obtained with good yield (52%).

The synthesis of DTCTT core was performed using a published procedure[24,25]. In this synthesis, di(trimethylstannyl)thienothiophene was coupled with 2-bromo-3-thiophene carboxylate to obtain precursor 3. Four octylbenzenes were introduced by reacting 3 with freshly prepared 4-octyl-phenyl magnesium bromide to obtain precursor 4. Cyclization was performed using an acidic Amberlyst catalyst but the product was found to be unstable and so it was immediately brominated to give dibromo-DTCTT with a reaction yield of 33 % for the 2 steps. This bright yellow powder was stable when stored at 5 °C. The DTCTT donor was synthesized using the same procedure as that for the IDT donor and dark greenish powder was collected with a reaction yield of 50 %.

4.3 Optical and Electrochemical Property

The absorption spectra were recorded for the dilute chloroform solutions and of films spin-cast from chloroform solution (Fig. 4.2a and b). The cyclic voltammetry was performed in dichloromethane solution under nitrogen atmosphere to examine the electrochemical properties (Fig. 4.2c). The parameters obtained are summarized in Table 4.1. The IDT donor can harvest light over a wide range of the visible spectrum. The λ_{max} is 586 nm for the solution and 611 nm for thin films which values matched well with the reported

values[8]. By comparison, the thienothiophene analogue the DTCTT donor showed red-shifted spectra with the absorption maxima of 634 nm and 670 nm for the solution and the thin film, respectively. The absorption coefficient calculated from the solution spectra is also higher (10.7×10^4) than that of the IDT (8.4×10^4), indicating thienothiophene enhances the absorptivity. A clear difference was observed in the behavior of annealed films in that no spectral changes were seen for a film of the IDT donor whereas the absorption maximum of the annealed film of the DTCTT donor was red-shifted by 29 nm to 699 nm. This data corresponds well with the differential scanning calorimetry (DSC) data which will be discussed later. Both the absorption and DSC data confirmed that the thienothiophene moiety significantly affected the crystallinity due to better π–π stacking resulting in the formation of aggregates. The bandgap calculated from the absorption onset in the unannealed thin film was 1.83 eV for the IDT donor and 1.66 eV for the DTCTT donor, which indicating both compounds are suitable for high efficiency solar cells.

Table 4.1 Optical and electrochemical properties of di(HTh2BT)IDT and di(HTh2BT)DTCTT.

	λ_{max} solution [nm]	ε [$M^{-1}cm^{-1}$]	λ_{max} film [nm]	λ_{on} [nm]	E_g [eV][a]	E_{ox} [V vs Fc/Fc^+]	HOMO [eV][b]	LUMO [eV][c]
di(HTh2BT) IDT	586	8.38×10^4	611 (611)[d]	677 (677)[d]	1.83 (1.83)[d]	0.375	-5.18	-3.35
di(HTh2BT) DTCTT	634	10.7×10^4	670 (699)[d]	747 (766)[d]	1.66 (1.62)[d]	0.15	-4.95	-3.29

[c]calculated by onset wavelength in film state. [b]estimated by oxidization potential [c]calculated by LUMO = HOMO + E_g [d]data obtained from annealed sample (100 °C for di(HTh2BT)IDT and 130°C for di(HTh2BT)DTCTT sample)

The HOMO/LUMO level was estimated from the optical absorption data and the oxidization peak on cyclic voltammogram.

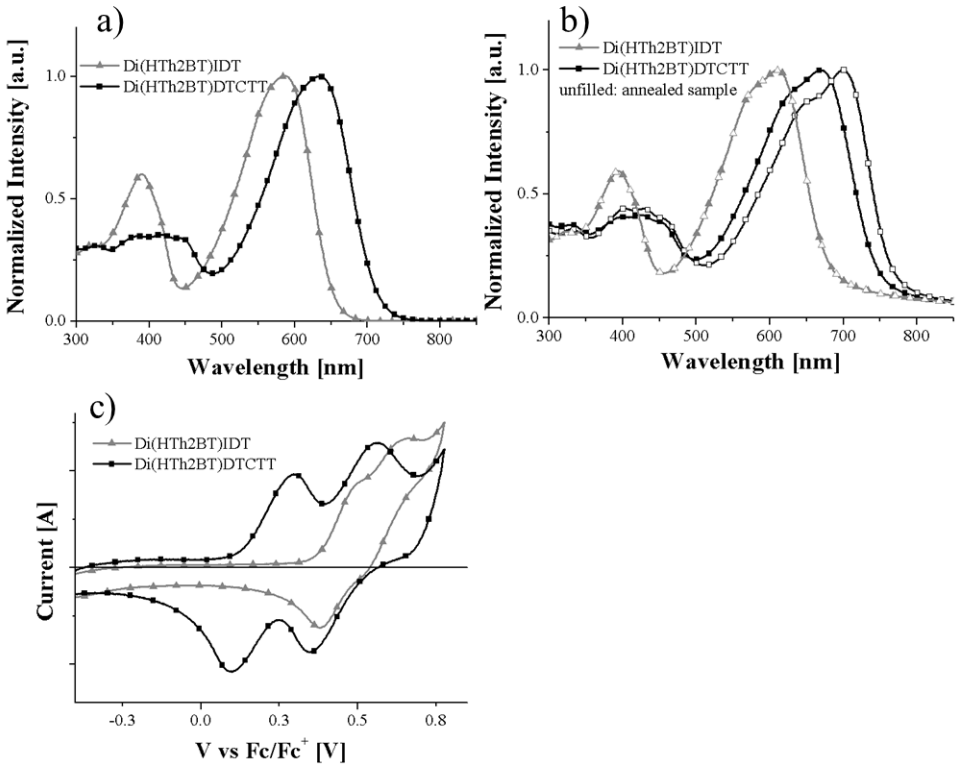

Fig. 4.2 UV-vis absorption spectra a) in chloroform and b) in film (unfilled symbol: annealed film), and c) Cyclic voltammogram in dichloromethane (grey triangle: di(HTh2BT)IDT black square: di(HTh2BT)DTCTT). Film was prepared by spincoating from chloroform solution.

Ferrocene/Ferrocenium (Fc/Fc^+) redox couple was used as an internal reference with an absolute redox potential of 4.8 eV below the vacuum level. HOMO level of the DTCTT donor was estimated to be -4.95 eV, which is ca. 0.2 eV higher than that of the IDT donor: -5.18 eV, while the LUMO level appeared to be the same. Density Functional Theory (DFT) calculations were carried out to simulate the molecular orbital (Fig. 4.3). The result revealed that the HOMO is distributed all over the conjugated system whereas the LUMO level is localized on the BT moiety to a certain degree, indicating the HOMO is affected by the strong electron-donating ability of the thienothiophene core whereas the LUMO level is mainly determined by the BT moiety.

	di(HTh2BT)DTCTT	di(HTh2BT)IDT
LUMO	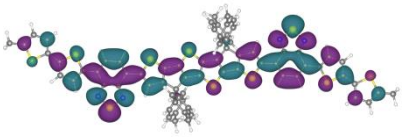	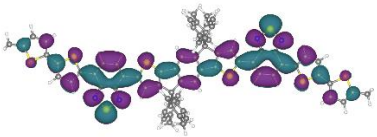
HOMO	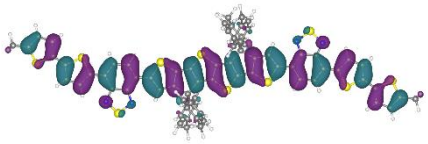	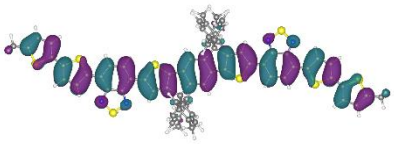

Fig. 4.3 Electronic cloud distribution of LUMO and HOMO levels for di(HTh2BT)DTCTT and di(HTh2BT)IDT calculated by B3LYP/6-31g(d,p) method.

4.4 Structural analysis in thermodynamic and electronic properties

Thermal properties of the molecules were analyzed using DSC (Fig. 4.4) and TGA (Fig. 4.5); the temperatures for the various transitions and decomposition are summarized in Table 4.2. The IDT donor showed a melting peak at 115 °C on the first heating cycle and a glass transition at 71 °C on the cooling cycle. On the second heating cycle, no melting peak was observed. Thus, it formed a glass-super cooling phase in the solid state, indicating the amorphous nature of the IDT. The DTCTT donor showed a melting peak at 235 °C on the first heating cycle and this is a much higher than that observed for the IDT donor. Besides the melting peak and a crystallization peak at around 230 °C, weaker peaks were observed on cooling and on second heating. Based on the images obtained under a polarized optical microscope on hot plate, it can be concluded these originate from solid-to-solid phase transitions. It is worth noting that these phase transitions were reversible and changing scanning speed from 10 °C to 1 °C/min did not change this behavior. Investigation of polymorphic structure gives insight of self-assembly structure and associated intermolecular

interaction. Detailed structural analysis of this phenomenon together with other derivatives will be presented in the next chapter. To our surprise, incorporation of the thienothiophene moiety, compared to the case of benzene, completely changed the self-organization character of the molecules from amorphous to crystalline even in the presence of bulky phenyl groups on the sp3 carbon. Both compounds have decomposition temperatures of over 400 °C, implying that they are stable under the PV operating conditions.

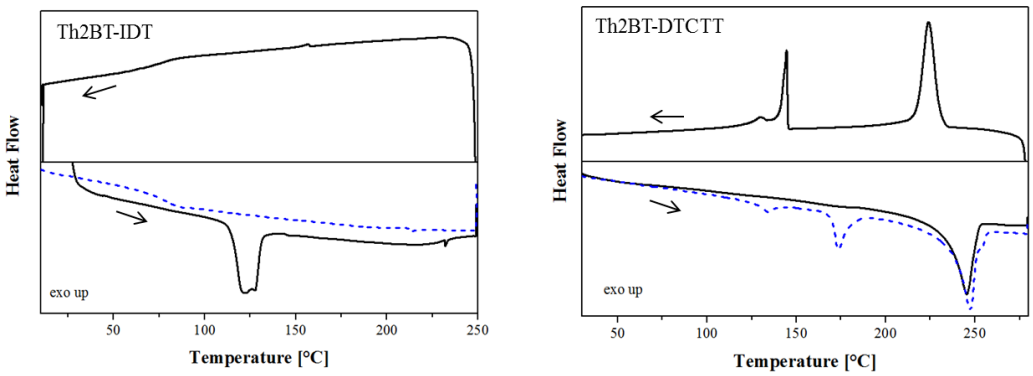

Fig. 4.4 Differential scanning calorimetry (DSC) of di(HTh2BT)IDT (left) and di(HTh2BT)DTCTT (right); dotted blue line is the 2nd heating cycle.

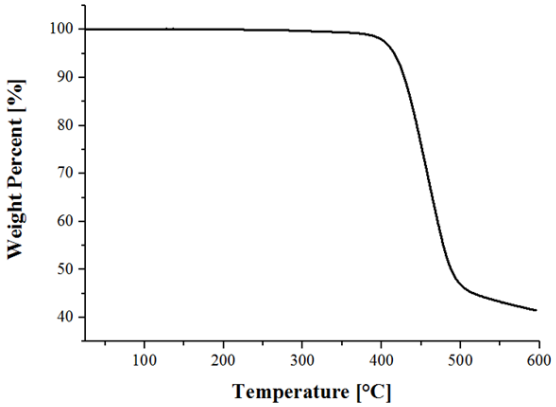

Fig. 4.5 Thermal gravimetric analysis graph of di(HTh2BT)DTCTT.

Table 4.2 Thermal properties of di(HTh2BT)IDT and di(HTh2BT)DTCTT

	1st Heating °C [kJ/mol]	Cooling °C [kJ/mol]	2nd Heating °C [kJ/mol]	T_{dcmp} °C
di(HTh2BT)IDT	T_m: 114.9 [18.2]	T_g: 70.8	T_g: 79.0	430[a]
di(HTh2BT)DTCTT	T_m: 234.9 [43.3]	T_{cr}: 230.3 [39.4]	T_{tr1}: 127.6 [2.60]	420[b]
		T_{tr}: 145.2 [18.3]	T_{tr2}: 169.8 [12.3]	
			T_m: 237.3 [44.7]	

T_{dcmp}: decomposition temperature, T_m: melting temperature, T_g: glass transition temperature, T_{cr}: crystallization temperature, T_{tr}: phase transition temperature

[a]taken from ref[8]. [b]measured from TGA under nitrogen atmosphere

In order to evaluate the difference in crystallinity and the effect on charge transport, hole mobility measurement was conducted. The hole mobilities of the DTCTT donor and the IDT donor in pristine film-state were estimated by fitting the dark current to space charge limited current (SCLC) model using hole-only devices with the configuration of ITO/PEDOT:PSS/pristine film/Au. Square root of the dark current in saturated current region under high bias voltage was found to vary proportionally to V (Fig. 4.6). This indicates the operation condition of space-charge-limited-current. The hole mobility μ_0 at zero field was obtained by fitting the experimental dark current to the Mott–Gurney equation (1)[32].

$$J = \frac{9}{8}\varepsilon_0\varepsilon_r\mu_0 \exp\left(0.89\beta\sqrt{\frac{V-V_{bi}}{L}}\right)\frac{(V-V_{bi})^2}{L^3} \qquad (1)$$

Given that the dielectric constant of the material, ε_r, is 3 (assumed from typical value of organic semiconductors), the hole mobility of the DTCTT donor and the IDT donor in pristine film are estimated to be 1.6 x 10^{-3} and 7.3 x 10^{-5} $cm^2/V{\cdot}s$, respectively. The hole mobility of the DTCTT donor is one order of magnitude higher than that of the IDT donor. This is consistent with the higher degree of order in the crystalline film of the DTCTT donor compared to the amorphous film of the IDT donor. These improvements in solid-state

organization with the incorporation of the thienothiophene moiety have a strong implication for PV applications as they can potentially lead to stronger absorption and also better charge transport.

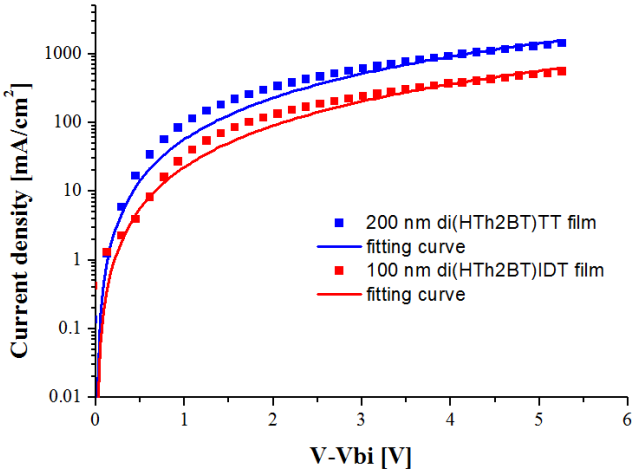

Fig. 4.6 Dark J-V curves of hole-only devicescomposed of di(HTh2BT)DTCTT with thickness of 200 nm (blue square) and di(HTh2BT)IDT with thickness of 100 nm (red square) pristine film, respectively. The solid lines are fit to the experimental data according to the equation (1).

4.5 OPV device performance

Both compounds were blended with $PC_{71}BM$ and incorporated into bulk heterojunction solar cell devices with the following device structure: ITO/PEDOT:PSS/Active layer/TiOx/Al. In this device architecture, TiOx interlayer[33] was included as an electron transporting interlayer. The device optimization was carried out by varying the donor-acceptor ratio, solvent system, and spincoating condition. Optimum result was obtained with donor-acceptor ratio of 1:3 (wt/wt), 15 mg/ml in anhydrous chloroform:oDCB = 9:1, and dynamic spincoat at 1500 rpm, which current-voltage curve is shown in Fig. 4.7 and the parameters obtained are listed in Table 4.3. The solar cell with the IDT donor and PCBM acceptor 1:3 wt ratio was also prepared according to

published literature[8] and very similar values were obtained to those previously reported J_{sc} of -9.3 mA/cm^2 and V_{oc} of 0.94 V, respectively with PCE of 3.2%. As for the device fabrication of the DTCTT donor, a range of donor-acceptor ratio from 1:1 to 1:4 (wt/wt) was investigated. At large donor ratios, the device performance was poor (at 1:1 ratio, PCE of 0.72 % with J_{sc} of -2.8 mA/cm^2, V_{oc} of 0.73 and FF of 0.34). The best result was obtained for the donor-acceptor ratio of 1:3 – PCE of 2.6% with a J_{sc} of -8.8 mA/cm^2, V_{oc} of 0.74 and FF of 0.41. Compared to the reported DTCTT-BT copolymer mentioned earlier in the introduction, comparable J_{sc} is obtained but the V_{oc} is increased by 0.15 V (V_{oc} of 0.59 V) for DTCTT with hexyl phenyl side groups and 0.1 V (V_{oc} of 0.64 V) for DTCTT with octyloxy phenyl side groups[24,25]. There is a general trend for small molecular donors of showing higher V_{oc} than the analogous polymer[34,35]. Further optimization carried out by annealing at various temperatures and using diiodooctane (DIO) additive did not result in better performance.

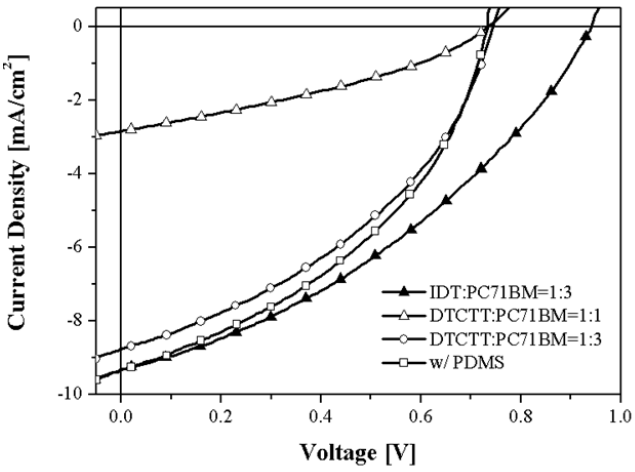

Fig. 4.7 OPV device performance**:** Current density-voltage characteristics of each device in a structure of ITO/PEDOT:PSS/Active layer/TiOx/Al under the illumination of AM1.5G, 100 mW/cm^2.

Polydimethoxysiloxane (PDMS) was used to modify the viscosity of solution for the purpose of improving the film quality[36] and a slight improvement was obtained: PCE of 2.8 % with J_{sc} of -9.33 mA/cm^2, V_{oc} of 0.73, and FF of 0.42. Compared to parameters with the IDT donor, the J_{sc} is of comparable value but the V_{oc} is lower by 0.2 V, corresponding to the difference in the HOMO levels estimated by cyclic voltammetry. A low FF is the main cause for this rather low PCE value.

Table 4.3 Photovoltaic performance of the bulk heterojunction molecular donor/$PC_{71}BM$ devices

Active layer	D/A ratio	PCE [%]	J_{sc} [mA/cm^2]	V_{oc} [V]	FF
di(HTh2BT)IDT: $PC_{71}BM$	1:3	3.21 (3.00±0.11)	-9.32 (-8.94±0.25)	0.94 (0.94±0.00)	0.37 (0.36±0.01)
di(HTh2BT)DTCTT: $PC_{71}BM$	1:1	0.72 (0.68±0.02)	-2.84 (-2.67±0.07)	0.73 (0.73±0.01)	0.34 (0.35±0.00)
	1:3	2.63 (2.48±0.12)	-8.76 (-8.53±0.20)	0.74 (0.74±0.00)	0.41 (0.39±0.01)
w/ PDMS	1:3	2.84 (2.67±0.08)	-9.33 (-8.85±0.22)	0.73 (0.73±0.00)	0.42 (0.41±0.00)

[a]average values inside parenthesis were calculated from 8 devices

Active layer was prepared from chlorofrom:o-dichlorobenzene = 9:1 mixed solution (15 mg/ml at different D/A ratios) by spin-coating at 1500 rpm for 90 sec, resulting in ca. 100 nm thick layer. 0.2 mg/ml PDMS chloroform solution was used instead of pure chloroform in the case of PDMS treated film. More details of the device fabrication condition are available in page 32.

To investigate the causes of this low FF, XRD and AFM analysis were performed on thin films. The sample crystallinity in film state was measured using XRD (Fig. 4.8). The pristine film of the DTCTT donor showed a strong diffraction peak at 2θ = 3.65 °, whereas pristine film of the IDT donor showed no peak due to its amorphous nature. This is a direct evidence for induced crystallinity due to the incorporation of thienothiophene into the core structure. Annealing at 200 °C induced relaxation of the aggregation structure and two peaks at 2θ = 4.04 and 8.12 ° appeared, indicating lamellar structure (d = 2.2 nm). However, no peak was observed in the blend film with $PC_{71}BM$ for both

1:1 and 1:3 wt ratios. It seems $PC_{71}BM$ prevents the effective aggregation of the DTCTT donor. The lack of strong crystallinity in the blend film is thus believed to be the reason for the low fill factor as both high mobility value (>10^4 $cm^2/V \cdot s$) and balanced hole and electron transport properties are necessary to achieve a high fill factor [37].

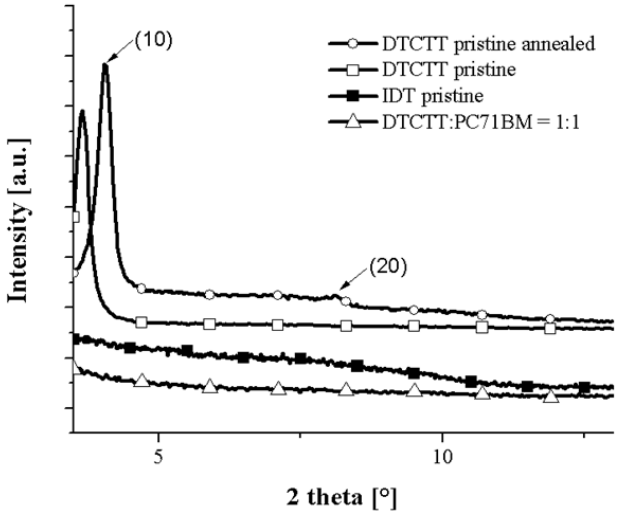

Fig. 4.8 Out-of-plane XRD patternsfor thin film of the DTCTT pristine film (square), the annealed film at 200 °C for 3 min (circle), the IDT pristine film (filled square), and the di(HTh2BT)DTCTT/$PC_{71}BM$ blend film with the ratio of 1 to 1 (triangle). All film was prepared by spincoating solution from chloroform:oDCB = 9:1 mixed solvent.

The surface morphology of the DTCTT donor in the film state was analyzed using AFM operating in tapping mode. Sample films were prepared by spin-coating on top of a PEDOT:PSS layer using the same deposition conditions as those used for the solar cell fabrication. The height image and phase image are shown (Fig. 4.9). The difference in donor-acceptor weight ratio can result in a large morphological variation. It seems that the DTCTT donor tends to form a rough surface as can be seen on the pristine film (RMS roughness factor of 14.2 nm). The blend film with $PC_{71}BM$ makes it smoother (2.38 nm for 1:1 ratio)

and finally a very smooth film (0.67 nm for 1:3 ratio) was obtained at the optimum donor-acceptor ratio. Many pores were observed in the blend film at 1:1 ratio. This rough morphology eventually leads to the direct contact between cathode and anode interlayer which may explain the large leakage current measured in the device with this blend ratio. The good film morphology for 1:3 D-A ratio film resulted in the best device performance with a high J_{sc} of about -9.0 mA/cm^2. The well-mixed morphology of donor and acceptor induce good exciton separation; the very smooth surface morphology also leads to enhanced charge extraction toward electrodes.

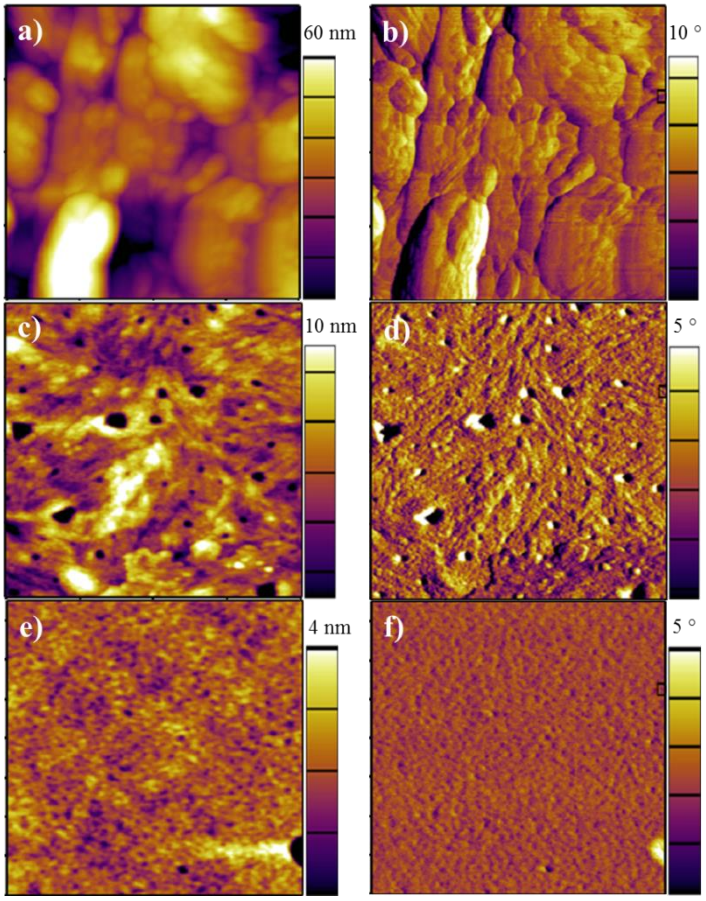

Fig. 4.9 AFM (2 x 2 μm) height and phase images of di(HTh2BT)DTCTT pristine film (a and b), blend film with $PC_{71}BM$ (1:1 wt/wt) (c and d), and (1:3 wt/wt) (e and f).

Finally, the EQE spectra of complete devices were compared between devices incorporated with the IDT donor and the DTCTT donor (Fig. 4.10). In the case of devices with the DTCTT donor sample, PDMS additive was used in active layer preparation. Both types of devices showed EQE response over a broad range of wavelength from 350 nm to 800 nm and this agrees very well to the UV-Vis absorption data. Red-shifted absorption profile of the DTCTT donor especially contributed to the higher EQE response over 670 nm. However, the EQE spectrum indicates the photo-generation takes place mainly from $PC_{71}BM$ exciton. This can be simply explained by UV-vis absorption spectra of the blend films (Fig. 4.11). Absorption spectrum of the 1:3 blend film matches well with the EQE response, indicating the amount of the DTCTT donor in film was not optimal. The 1:1 blend film has a balanced absorption spectrum contributed by both of $PC_{71}BM$ and the DTCTT donor, but the film quality was poor as was seen on AFM image. Further structural modification is necessary to promote an effective crystallization and uniform film morphology.

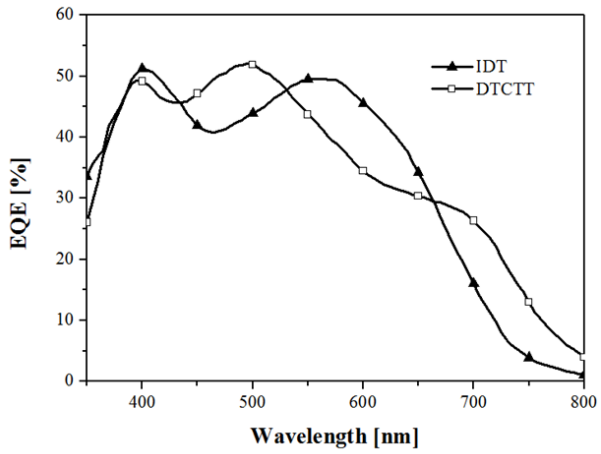

Fig. 4.10 EQE curves of the devices based on di(HTh2BT)IDT:$PC_{71}BM$ = 1:3 and di(HTh2BT)DTCTT:$PC_{71}BM$ = 1:3 with PDMS treatment.

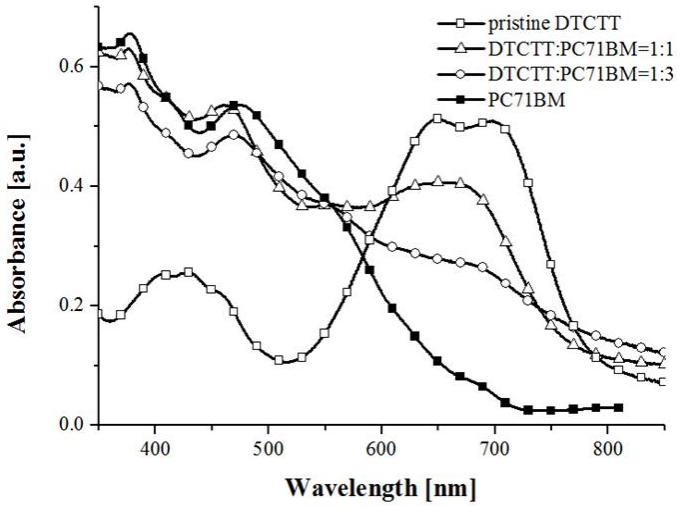

Fig. 4.11 UV-vis absorption spectra of the di(HTh2BT)DTCTT (square) and PC71BM (filled square) pristine film and the blend film with the ratio of 1 to1 (triangle) and 1 to 3 (circle).

4.6 Short summary

A novel molecular donor the di(HTh2BT)DTCTT with a DTCTT as a central building block has been synthesized and the properties were systematically investigated and compared to the analogous IDT-based material. Although the only structural difference is the incorporation of thienothiophene and benzene units, respectively, in the core structure, clear differences were observed in their structural, optical, electrochemical, thermal properties, and OPV device performance. The electron-rich TT core induced a red-shift in the absorption and a higher HOMO level. Furthermore, this new molecular donor material has higher thermal stability compared to the IDT donor and the new molecular structure promoted better crystallinity, possibly because of the strong S-S intermolecular interactions which produce greater overlap of frontier molecular orbitals. In OPV device performance, larger J_{sc} was expected based on the light absorption profile and the J_{sc} obtained was indeed a high value of -9.33 mA/cm^2. However that was only comparable to the device incorporated with the IDT

because of the rough surface film and the lack of effective crystallization. A rather low PCE of 2.84% was obtained in the devices. Increasing the low FF of 0.42 will be the key factor to contribute to the further development of these devices with the DTCTT donor. This improvement could be achieved by modifying the molecular structure to promote effective crystallization either by extending aromatic linker parts or fixing intramolecular conformation between DTCTT core and BT units. This ongoing modification work is explained in the chapter 6. Overall, enhanced crystallinity of the DTCTT is a promising feature as other efficient IDT-based OPV material improved their crystallinity by extending conjugation[10], replacing bulky phenyls on the sp3 carbon to flexible alkyl chains[11], and extending IDT backbone itself[38,39]. The results presented in this paper provide the definitive suggestions for further development of DTCTT based functional materials.

References:

[1] X. Guo, M. Zhang, J. Tan, S. Zhang, L. Huo, W. Hu, Y. Li, J. Hou, *Adv Mater* 24 **(2012)** 6536.

[2] D. Dang, W. Chen, S. Himmelberger, Q. Tao, A. Lundin, R. Yang, W. Zhu, A. Salleo, C. Müller, E. Wang, *Advanced Energy Materials* 4 **(2014)** 1400680.

[3] D.B. Sulas, K. Yao, J.J. Intemann, S.T. Williams, C.-Z. Li, C.-C. Chueh, J.J. Richards, Y. Xi, L.D. Pozzo, C.W. Schlenker, A.K.Y. Jen, D.S. Ginger, *Chemistry of Materials* 27 **(2015)** 6583.

[4] Y.-C. Chen, C.-Y. Yu, Y.-L. Fan, L.-I. Hung, C.-P. Chen, C. Ting, *Chemical Communications* 46 **(2010)** 6503.

[5] Y. Sun, G.C. Welch, W.L. Leong, C.J. Takacs, G.C. Bazan, A.J. Heeger, *Nat Mater* 11 **(2012)** 44.

[6] Z.B. Henson, K. Mullen, G.C. Bazan, *Nat Chem* 4 **(2012)** 699.

[7] Y. Chen, X. Wan, G. Long, *Accounts of Chemical Research* 46 **(2013)** 2645.

[8] W. Yong, M. Zhang, X. Xin, Z. Li, Y. Wu, X. Guo, Z. Yang, J. Hou, *Journal of Materials Chemistry A* 1 **(2013)** 14214.

[9] D. Liu, M. Xiao, Z. Du, Y. Yan, L. Han, V.A.L. Roy, M. Sun, W. Zhu, C.S. Lee, R. Yang, *Journal of Materials Chemistry C* 2 **(2014)** 7523.

[10] X. Liu, Q. Li, Y. Li, X. Gong, S.-J. Su, Y. Cao, *Journal of Materials Chemistry A* 2 **(2014)** 4004.

[11] J.-L. Wang, Q.-R. Yin, J.-S. Miao, Z. Wu, Z.-F. Chang, Y. Cao, R.-B. Zhang, J.-Y. Wang, H.-B. Wu, Y. Cao, *Advanced Functional Materials* 25 **(2015)** 3514.

[12] H. Bai, P. Cheng, Y. Wang, L. Ma, Y. Li, D. Zhu, X. Zhan, *J. Mater. Chem. A* 2 **(2014)** 778.

[13] Y. Lin, J. Wang, Z.G. Zhang, H. Bai, Y. Li, D. Zhu, X. Zhan, *Adv Mater* 27 **(2015)** 1170.

[14] Y. Lin, Q. He, F. Zhao, L. Huo, J. Mai, X. Lu, C.J. Su, T. Li, J. Wang, J. Zhu, Y. Sun, C. Wang, X. Zhan, *J Am Chem Soc* 138 **(2016)** 2973.

[15] W. Zhao, D. Qian, S. Zhang, S. Li, O. Inganäs, F. Gao, J. Hou, *Adv Mater* 28 **(2016)** 4734.

[16] J.-S. Wu, S.-W. Cheng, Y.-J. Cheng, C.-S. Hsu, *Chemical Society Reviews* 44 **(2015)** 1113.

[17] K. Takimiya, S. Shinamura, I. Osaka, E. Miyazaki, *Adv Mater* 23 **(2011)** 4347.

[18] W. Ni, M. Li, F. Liu, X. Wan, H. Feng, B. Kan, Q. Zhang, H. Zhang, Y. Chen, *Chemistry of Materials* 27 **(2015)** 6077.

[19] J.A. Love, I. Nagao, Y. Huang, M. Kuik, V. Gupta, C.J. Takacs, J.E. Coughlin, L. Qi, T.S. van der Poll, E.J. Kramer, A.J. Heeger, T.Q. Nguyen, G.C. Bazan, *J Am Chem Soc* 136 **(2014)** 3597.

[20] X. Zhu, B. Xia, K. Lu, H. Li, R. Zhou, J. Zhang, Y. Zhang, Z. Shuai, Z. Wei, *Chemistry of Materials* 28 **(2016)** 943.

[21] J. Wolf, M. Babics, K. Wang, Q. Saleem, R.-Z. Liang, M.R. Hansen, P.M. Beaujuge, *Chemistry of Materials* 28 **(2016)** 2058.

[22] L. Liang, J.-T. Wang, X. Xiang, J. Ling, F.-G. Zhao, W.-S. Li, *Journal of Materials Chemistry A* 2 **(2014)** 15396.

[23] W. Li, W. Deng, K. Wu, G. Xie, C. Yang, H. Wu, Y. Cao, *Journal of Materials Chemistry C* 4 **(2016)** 1972.

[24] H. Bronstein, R.S. Ashraf, Y. Kim, A.J. White, T. Anthopoulos, K. Song, D. James, W. Zhang, I. McCulloch, *Macromolecular Rapid Communications* 32 **(2011)** 1664.

[25] Y.J. Cheng, C.H. Chen, T.Y. Lin, C.S. Hsu, *Chem Asian J* 7 **(2012)** 818.

[26] B.C. Schroeder, R.S. Ashraf, S. Thomas, A.J. White, L. Biniek, C.B. Nielsen, W. Zhang, Z. Huang, P.S. Tuladhar, S.E. Watkins, T.D. Anthopoulos, J.R. Durrant, I. McCulloch, *Chem Commun (Camb)* 48 **(2012)** 7699.

[27] N. Cai, R. Li, Y. Wang, M. Zhang, P. Wang, *Energy & Environmental Science* 6 **(2013)** 139.

[28] H. Li, T.M. Koh, Y. Hao, F. Zhou, Y. Abe, H. Su, A. Hagfeldt, A.C. Grimsdale, *ChemSusChem* 7 **(2014)** 3396.

[29] A.C. Grimsdale, K. Leok Chan, R.E. Martin, P.G. Jokisz, A.B. Holmes, *Chem Rev* 109 **(2009)** 897.

[30] A. Pelter, I. Jenkins, D.E. Jones, *Tetrahedron* 53 **(1997)** 10357.

[31] T.S. van der Poll, J.A. Love, T.Q. Nguyen, G.C. Bazan, *Adv Mater* 24 **(2012)** 3646.

[32] Z.B. Wang, M.G. Helander, M.T. Greiner, J. Qiu, Z.H. Lu, *Journal of Applied Physics* 107 **(2010)** 034506.

[33] J.Y. Kim, S.H. Kim, H.H. Lee, K. Lee, W. Ma, X. Gong, A.J. Heeger, *Adv Mater* 18 **(2006)** 572.

[34] B. Walker, C. Kim, T.-Q. Nguyen, *Chemistry of Materials* 23 **(2011)** 470.

[35] J. Zhou, Y. Zuo, X. Wan, G. Long, Q. Zhang, W. Ni, Y. Liu, Z. Li, G. He, C. Li, B. Kan, M. Li, Y. Chen, *J Am Chem Soc* 135 **(2013)** 8484.

[36] K.R. Graham, J. Mei, R. Stalder, J.W. Shim, H. Cheun, F. Steffy, F. So, B. Kippelen, J.R. Reynolds, *ACS Appl Mater Interfaces* 3 **(2011)** 1210.

[37] C.M. Proctor, J.A. Love, T.-Q. Nguyen, *Adv Mater* 26 **(2014)** 5957.

[38] H.-C. Wang, L.-M. Tang, L. Zuo, H. Chen, Y.-X. Xu, *RSC Advances* 5 **(2015)** 80677.

[39] J.J. Intemann, K. Yao, F. Ding, Y. Xu, X. Xin, X. Li, A.K.Y. Jen, *Advanced Functional Materials* 25 **(2015)** 4889.

Chapter 5

Structural Investigation of self-assembled structures of the DTCTT and IDT-based small molecules

Findings obtained in the previous chapter suggested that the structural modification of the DTCTT-based small molecules is necessary to improve the device performance. In order to redesign, self-assembled structures of the derivatives of both the IDT and the DTCTT molecules with different side groups were investigated. For the IDT derivatives, the crystal structure indicated a lack of the π–π stacking and a disordered intramolecular conformation. This will explain why they form amorphous phase in thin-films. On the other hand, extensive X-ray diffraction studies revealed the slipped-stacked packing mode for the DTCTT derivatives. The reversible phase transition behavior of di(HTh2BT)DTCTT suggested the 1D organized structure, which was also shown in the thin-film GI-SWAXS results. The observed phenomenon could be the result of the combination of stabilized slipped-stacked packing and the flexibility of the side groups. This type of molecular self-assembly can result in structures that are efficient for charge carrier transport, as shown in the OFET device. The qualitative understanding obtained in this research provides insights for further molecular engineering.[2]

[2] This section published substantially as reference:
Y. Abe, V. Savikhin, J. Yin, C. Soci, A.C. Grimsdale, M.F. Toney, Y.M. Lam: Elucidating Molecular Design on Structural and Functional Properties of Fused Ladder Thienoarenes – Novel Reversible Crystal-to-crystal Phase Transition Behavior, *To be submitted.*

5.1 Introduction

Structure/property relationship of organic semiconductors has attracted much attention since the realization of their optoelectronic applications such as organic photovoltaics (OPV). The morphology of the self-assembled structures often plays a critical role in determining the electrical properties which in turn affects the device performance. Decades of intensive research on organic materials have contributed to the establishment of a set of molecular design rules for high performance solar cells. One example is the D-A-D-A-D type of small molecular donors used in sm-OPV devices[1,2]. This type of molecules have demonstrated an impressive device result of up to 10% in PCE[3-5]. Their solid-state structures have also been investigated by both experimental and computational methods[6-10]. The device performance could be further improve by controlling the solid-state structure and improving relevant properties such as charge transport properties. There are still many challenges lying ahead in the understanding of the organization of crystallinity and morphology over the entire device scale.

In conjugated organic materials, charge transport properties depend on the packing structure of the molecules, especially the packing manner of the π-orbital overlap. However, the packing structure is mainly stabilized by weak van der Waals interactions and often several crystalline packing states (polymorphs) are observed. The polymorphs of π-conjugated molecules vary in the degree of π-orbital overlap; hence each polymorph can have different electronic properties depending on their packing structure Those polymorphs have also been used as an interesting platform to investigate the intrinsic charge transport properties and their relationship with the packing structures[11-13]. A certain polymorphic structure can be induced by manipulating the crystallization conditions; and thus, attempts have been made to obtain the ideal polymorph with structure most suitable for charge transport. Organic

semiconductors such as pentacene and its derivatives have been intensively studied and their polymorphs can be induced by thermal annealing[14], use of different substrates[15], mechanical shearing[16], solvent system[17], and polymer additives[18].

In the previous chapter, it is pointed out that better device performance is possible if the crystallinity of the DTCTT-based small molecules can be further improved in BHJ film. Hence, it is necessary to modify the structures so as to encourage better packing. In addition, unique reversible phase transition behavior has been observed for the DTCTT donor. Detailed structural analysis will give an insight into how structural reorganization takes place between the different phases and which intermolecular interactions are involved in stabilizing the corresponding structures. A series of IDT and DTCTT-based derivatives were newly synthesized to investigate the effects of the different side groups and to help to promote a qualitative understanding of the effect of different central cores and the chemical structures (Fig. 5.1). In addition, their electrical properties were measured using the OFET devices. A discussion on the relationship between the thin film structures and the electrical properties is also provided.

For the IDT and DTCTT, the molecule with one thiophene (Th) unit in the side groups ($R = R_1$) is expected to have less structural freedom compared to the one with two Th units ($R = R_2$). In addition, an extended dodecyl alkyl groups ($R = R_3$) were introduced in place of the hexyl chains in DTCTT to see the effect on the reversible phase transition behavior. These IDT and DTCTT derivatives are interesting platforms to investigate the relationship between crystallinity and molecular structure as slight change in chemical structures could result in the formation of amorphous (glass), crystalline and the polymorphic states (reversible phase transition state).

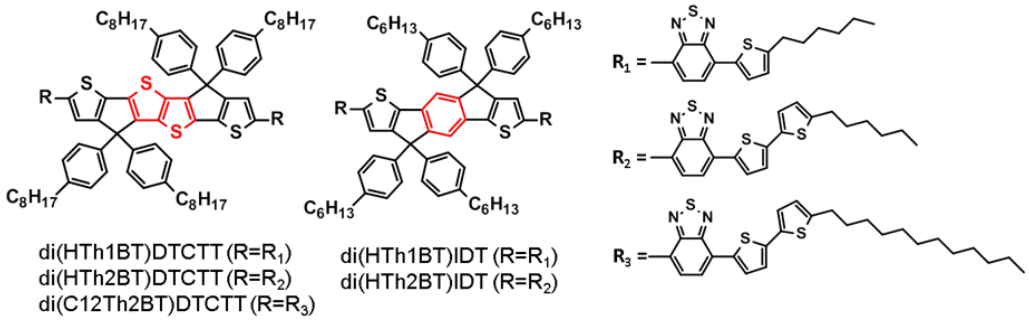

Fig. 5.1 Chemical structures of IDT and DTCTT derivatives

5.2 Synthesis

The synthetic scheme of the DTCTT and IDT derivatives is based on the similar scheme reported in the previous chapter and is shown in Scheme 5.1. Tributylstannyl-thiophenes were prepared and coupled with dibromo-benzothiadiazole by Stille reaction to yield compounds **1a-c**, whose bromo groups were then converted to pinacol borate to yield compounds **2a-c**. Each compound **2** was coupled with an IDT or DTCTT unit using the Suzuki reaction to form their respective derivatives, i.e., two IDT and three DTCTT derivatives. Note that the boronates **2** are unstable and can easily protonate in alkaline solution; and thus, potassium carbonate solution was injected into the reactant in the final step. The reaction was completed within an hour. Detailed experimental procedures are available in the Appendix.

5.3 Optical and Electrochemical Properties

UV-Vis absorption spectra and cyclic voltammograms of the derivatives are shown in Fig. 5.2. The corresponding optical and electrochemical parameters are summarized in Table 5.1. Compared to their Th2 counterparts di(HTh2BT)-IDT/DTCTT (R = R_2), the Th1 side group derivatives, i.e., di(HTh1BT)-IDT/DTCTT (R = R_1), showed a more blue-shifted absorption spectra in both solution and thin film. As for the IDT derivatives, a blue shift of 19 and 55 nm

was observed for solution and thin film respectively; for the DTCTT derivatives, it was 23 and 35 nm, respectively. The blue shift is attributed to the decrease in the conjugation length of the thiophene side groups. The spectra of the C12 derivative of DTCTT, i.e., di(C12Th2BT)DTCTT (R = R_3), does not show any shift compared to its C6 derivative (R = R_2). In thin-film state, the shape of the absorption spectra is also contributed by the solid-state structure of the samples. It seems that the Th1 derivatives of both IDT and DTCTT (R = R_1) are less likely to form ordered structures in thin film as evidenced from the broad and featureless shape of the spectra.

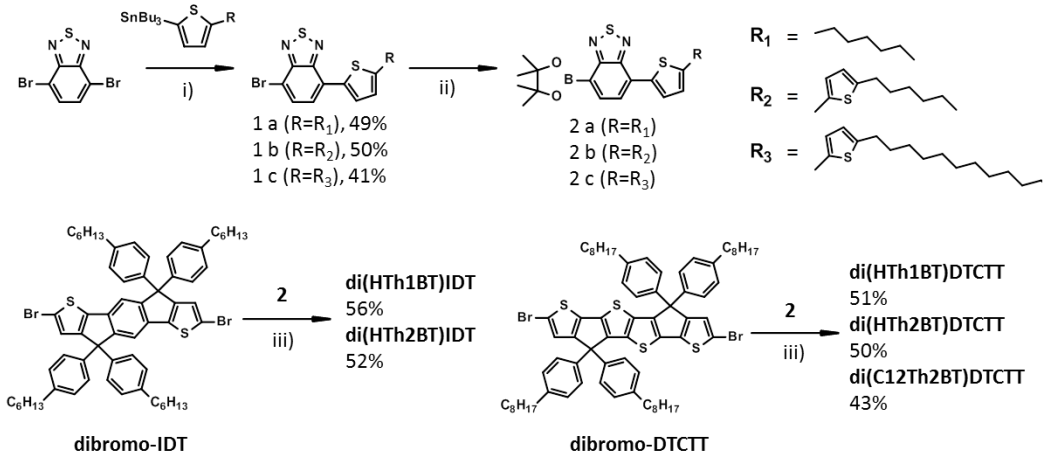

Scheme 5.1 Synthesis of IDT and DTCTT compounds i)$Pd(PPh_3)_4$, Toluene, 80 °C ii)B_2pin_2, $Pd(dppf)Cl_2$, KOAc, Toluene, 80 °C iii)$Pd(PPh_3)_4$, K_2CO_3, THF, 80°C

Cyclic voltammetry in dichloromethane solution were carried out and the oxidization peaks are shown in Fig. 5.2c. The variation of the side groups, i.e, the number of thiophene units and the length of the alkyl chains, appears to have no significant effect on the oxidization potentials and hence little effect on HOMO levels of both IDT and DTCTT derivatives. On the other hand, the LUMO levels that are calculated from the optical band gaps taken from thin film absorption spectra indicate that the Th1 derivatives (R = R_1) have higher energy levels. Considering the molecular orbital calculation in the previous

section of 4.3, the HOMO level is attributed to the central IDT/DTCTT moiety while the LUMO level can be attributed to the benzothiadiazole (BT) unit. Thus, it can be understood that the Th1 derivatives (R = R_1), which are less electron-inductive than Th2 derivatives (R = R_2), render the BT unit more electronegative, hence resulting in an increase in the LUMO level compared to the Th2 derivatives. The HOMO levels are not affected by Th units as they come from the IDT/DTCTT moiety.

5.4 Thermodynamic properties and polarized optical microscope image of the reversible phase transition behavior

The variation in the backbone structure of both IDT and DTCTT derivatives was found to impart distinct thermal behaviors, as observed in the differential scanning calorimetry spectra (DSC) shown in Fig. 5.3 and the thermodynamic properties are summarized in Table 5.2. Both IDT derivatives show glass transition temperature of around 70 °C on cooling after their initial melting at around 110 °C, indicating their amorphous nature. On the other hand, the DTCTT derivatives have crystalline nature as recrystallization peaks can be observed after their initial melting (melting at 245, 235, 221 °C and crystallization at 226, 230, 203 °C for R = R_1, R_2, R_3 derivatives, respectively). Besides, cooling at 10 °C/min after melting also induces additional phase transition peaks for the R = R_2 and R_3 derivatives. These transition peaks appear reversibly even on the 3rd and 4th heating and cooling cycle. Initially, this behavior was thought to be a thermotropic liquid crystal phase transition but the observation under polarized optical microscope (POM, Fig. 5.4 and Fig. 5.5) indicates this is a crystal-to-crystal reversible phase transition. From low to high temperature, each phase is assigned as L, H1, and H2 phases before melting into an isotropic liquid. These structure assignments are based on X-ray diffraction results presented in detail in the following discussion.

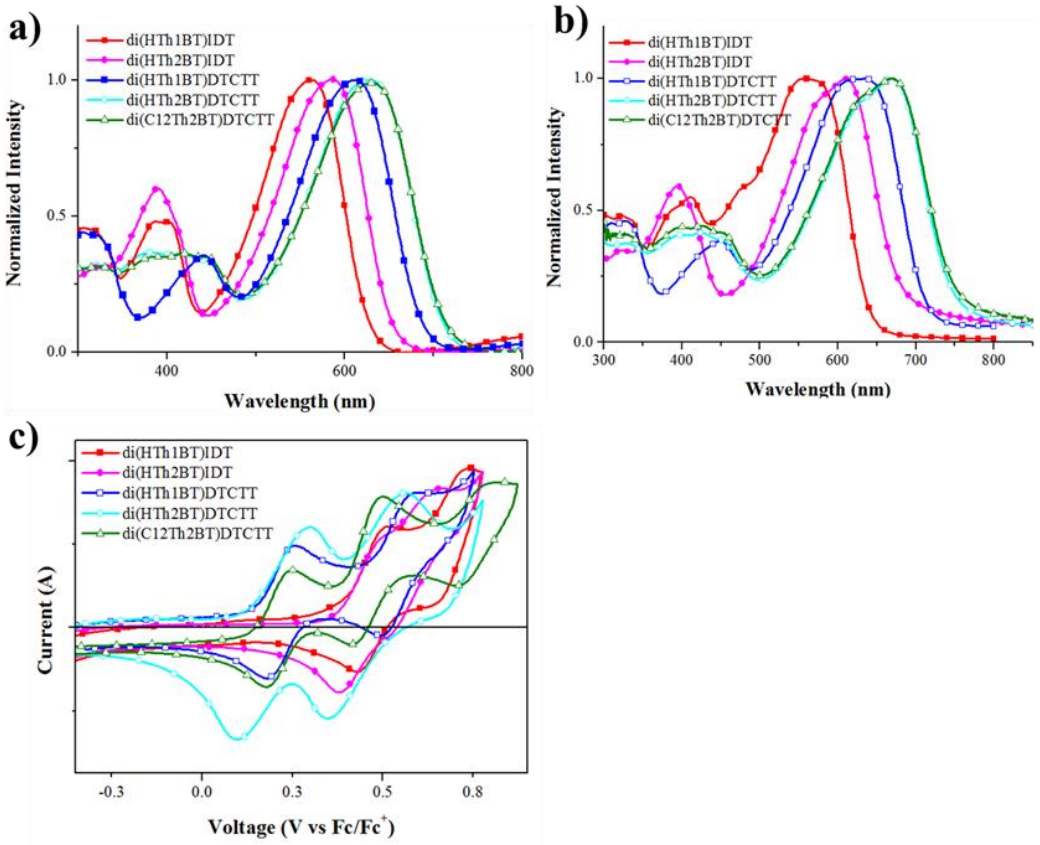

Fig. 5.2 UV-vis absorption spectra of IDT and DTCTT derivatives a) in chloroform solution and b) in thin film, and c) Cyclic voltammogram in dichloromethane. Film was prepared by spincoating from chloroform solution. Each color represents a derivative of the IDT and the DTCTT.

Table 5.1 Optical and electrochemical properties of the IDT and DTCTT derivatives

	λ_{max} CHL [nm]	λ_{max} film [nm]	λ_{on} film [nm]	E_g [eV][a]	E_{ox} [V vs Fc/Fc+]	HOMO [eV][b]	LUMO [eV][c]
di(HTh1BT)IDT	563	556	640	1.94	0.39	5.19	3.25
di(HTh2BT)IDT	586	611	677	1.83	0.38	5.18	3.35
di(HTh1BT)DTCTT	611	635	713	1.74	0.15	4.95	3.21
di(HTh2BT)DTCTT	634	670	747	1.66	0.15	4.95	3.29
di(C12Th2BT)DTCTT	632	668	745	1.66	0.15	4.95	3.29

[a]calculated from the onset wavelength in film state. [b]estimated from oxidization potential using -4.8 eV to vacuum as a reference Fc/Fc+ redox potential [c]calculated by LUMO = HOMO + Eg

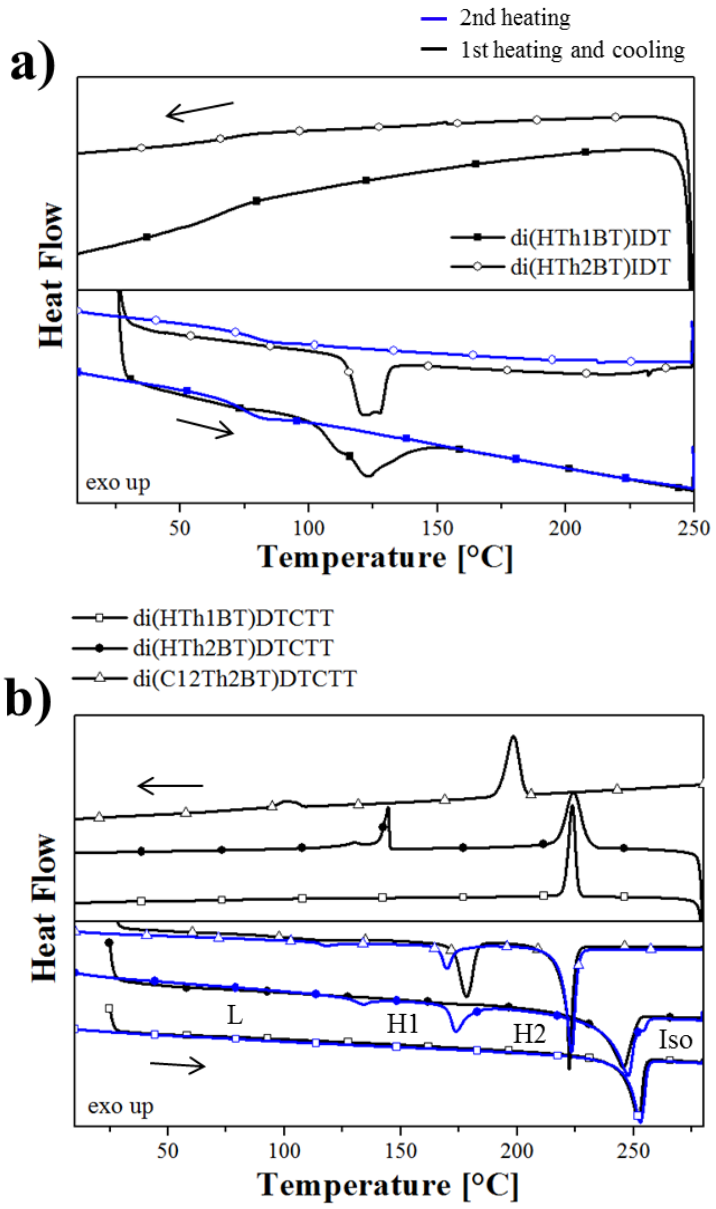

Fig. 5.3 Differential scanning calorimetry (DSC) of IDT derivatives (a) and DTCTT derivatives (b); black line is the first heating and cooling cycle and the blue line is the second heating cycle, scanned at 10 °C/min rate.

Table 5.2 Thermodynamic data for thermotropic phase transition of IDT and DTCTT derivatives

	1st Heating °C [kJ/mol]	Cooling °C [kJ/mol]	2nd Heating °C [kJ/mol]
di(HTh1BT)IDT	T_m: 108.4 [12.3]	T_g: 72.4	T_g: 74.6
di(HTh2BT)IDT	T_m: 114.9 [18.2]	T_g: 70.8	T_g: 79.0
di(HTh1BT)DTCTT	T_m: 245.1 [40.4]	T_{cr}: 226.0 [41.2]	T_m: 246.7 [39.7]
di(HTh2BT)DTCTT	T_m: 234.9 [43.3]	T_{cr}: 230.3 [39.4] T_{tr}: 145.2 [18.3]	T_{tr1}: 127.6 [2.60] T_{tr2}: 169.8 [12.3] T_m: 237.3 [44.7]
di(C12Th2BT)DTCTT	T_{tr}: 172.7 [35.1] T_m: 221.0 [54.9]	T_{cr}: 203.0 [52.3] T_{tr}: 108.0 [6.71]	T_{tr1}: 113.4 [2.16] T_{tr2}: 166.1 [11.0] T_m: 218.6 [55.2]

T_m: melting temperature, T_g: glass transition temperature, T_{cr}: crystallization temperature, T_{tr}: phase transition temperature

Under cross polarization filters, the film of di(HTh2BT)DTCTT (R = R_2) was placed on a hot plate (Fig. 5.4 at 30 °C) and was heated up to melting at 270 °C (Fig. 5.4 at 270 °C). No polarized light was observed at this temperature, indicating an isotropic liquid state. On cooling, it became crystallized and showed a color change at around 130 °C, indicating phase transition behavior and the reorganization of molecular alignment at this temperature. On the second heating, similar phase transition behavior was observed at 130 °C and further heating up to 170 °C resulted in cracks in crystals (Fig. 5.4 at 170 and 200 °C). Those three phase transition peaks of L, H1, and H2 are observed on DSC graphs (mixture of H2/H1/L transition at 145–125 °C on cooling, L/H1 transition at 128 °C and H1/H2 transition at 170 °C on second heating). It is worthwhile to note that cooling speed was found to significantly affect the formation of these phases. For di(HTh2BT)DTCTT, faster cooling rate than 30 °C/min induced an amorphous-like texture which did not show the structural reversibility when observed under the POM and XRD.

The di(C12Th2BT)DTCTT (R = R_3) also exhibit similar three phases on DSC graph (mixture of H2/H1/L transition at 108–100 °C on cooling, L/H1 transition at 113 °C and H1/H2 transition at 166 °C on heating) but no obvious morphological change was observed in the POM images (Fig. 5.5). This implies the structural reorganization takes place in a different manner from that of di(HTh2BT)DTCTT. The di(C12Th2BT)DTCTT also showed scanning rate-dependent DSC behavior. Compared to the two scanning rates, 10 °C/min and 2°C/min, the transition peak at 2 °C/min (Fig. 5.6) on cooling is more obvious and the H1/H2 transition peak implies the formation of an additional metastable state between H1 and H2 phases.

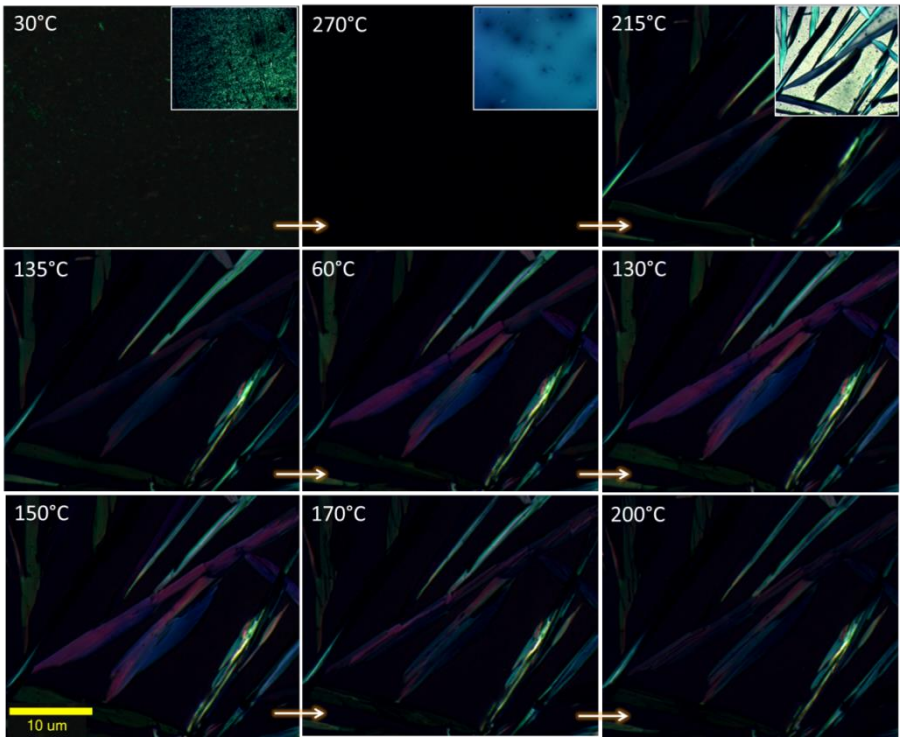

Fig. 5.4 Polarized optical microscope image of di(HTh2BT)DTCTT at 1st heating, cooling, and 2nd heating (thin film at 30 °C, isotropic liquid at 270 °C, cooling down to 60 °C, and 2nd heating up to 200 °C). Inset is the image under bright light.

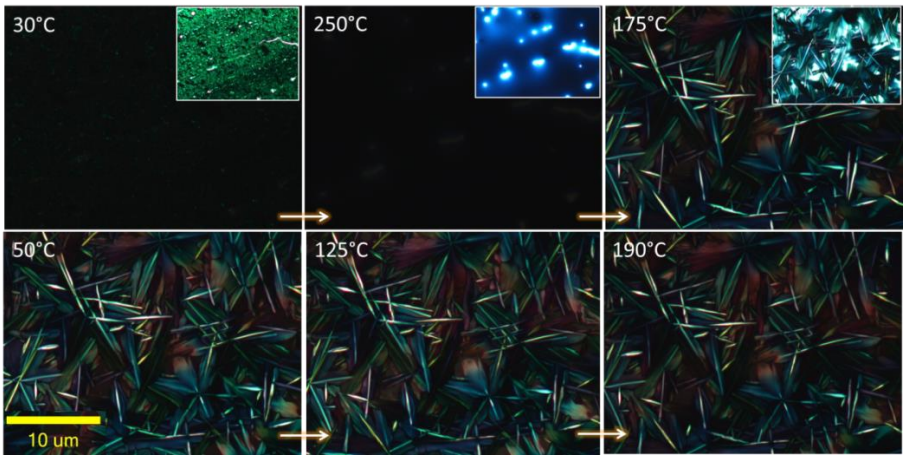

Fig. 5.5 Polarized optical microscope image of di(C12Th2BT)DTCTT at 1st heating, cooling, and 2nd heating cycle (thin film at 30 °C, isotropic liquid at 250 °C, cooling down to 50 °C, and heating up to 190 °C). Inset is the image under bright light

.

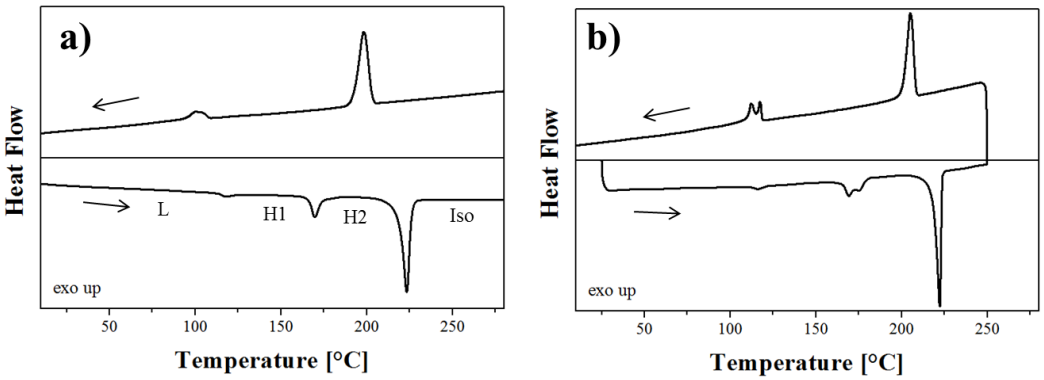

Fig. 5.6 Differential scanning calorimetry of di(C12Th2BT)DTCTT, scanned at a) 10 °C/min and b) 2 °C/min rate.

5.5 Structural Analysis

Detailed structural analysis was conducted in order to elucidate the self-assembled structure of the IDT and the DTCTT derivatives. Special focus was placed on the difference between the amorphous IDT and crystalline DTCTT core structures as well as the reversible crystal-to-crystal phase transition behavior of di(HTh2BT)DTCTT.

5.5.1 X-ray diffraction of IDT derivatives

Powder XRD and thin-film XRD (out-of-plane) were performed on di(HTh1BT)IDT and di(HTh2BT)IDT and the results are shown in Fig. 5.7. In a series of purification steps, the IDT derivatives were recrystallized with acetone/chloroform system; acetone is a poor solvent and chloroform is a good solvent for the compounds. The obtained crystals were ground and measured with powder XRD to get crystalline diffraction patterns. As for di(HTh1BT)IDT, a large single crystal suitable for X-ray crystallography was obtained using solvent vapor diffusion of the acetone/chloroform system.

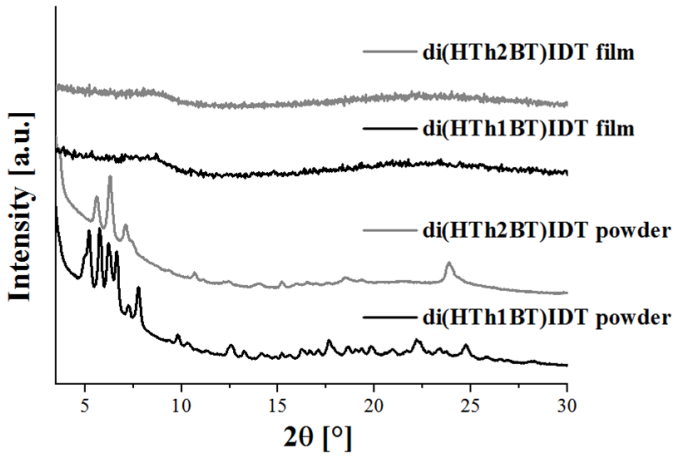

Fig. 5.7 XRD patterns of IDT derivatives in powder and thin film states

On the other hand, featureless diffraction patterns were recorded from the thin film samples which were made by spin-coating from the chloroform solutions, indicating amorphous structure. As previously indicated in the DSC data, the IDT derivatives show amorphous behavior. Thus, thermal annealing and solvent vapor annealing were found to have no effect on the diffraction patterns. The difficulty of the IDT derivatives to form ordered structures in thin film originates from the presence of four hexylphenyl groups on the sp3 carbon of the IDT moiety which hinder strong π–π stacking. Poor solvent, such as acetone, is thus necessary to induce nucleation through solvent-solute interaction and/or solvophobic effect[19-21].

Molecular self-assembled structure of di(HTh1BT)IDT was studied using single crystal XRD (Fig. 5.8). The molecule has an inversion center on the central benzene ring and half of the molecular structure is solved as an asymmetric unit. The crystal is monoclinic system with space group *C2/c* (a = 23.73, b = 27.78, c = 38.16 Å; b = 100.1 °; volume = 24768 $Å^3$). Three structural isomers are obtained which have different rotation angles among IDT, BT, and Th (Fig. 5.8a). Conformation of π-conjugated system is known to greatly affect the optical and electrical properties and planarizing the conformation is expected to give better photovoltaic device performance[22,23]. Coughlin and coworkers studied the rotational free energy of similar compounds and discussed its relationship with the structural factors [6,7]. Multiple nonbonding interactions such as π–π interactions, steric hindrance, and electrostatic forces compete with each other and when all the constitute goes to stabilizing the rotation, the "conformational lock" occurs. Three rotational isomers are formed in the di(HTh1BT)IDT crystal implying that the intermolecular interactions are so weak that it allows the metastable state of rotational isomers to form. The trimer structure in Fig. 5.8b shows the lack of π–π stacking despite the elongated conjugation length. In fact, one of the rotational isomers which sulfur atoms of the IDT, BT, and Th units form the anti-conformation has a high dihedral angle

of 38.3 ° and the entire molecule has a distortion along the long-axis (Fig. 5.8c). Taking a closer look at the intermolecular interactions, the S–S interactions between BT-BT and BT-IDT and Th-Th seem to play a key role in stabilizing the trimer structure instead of the π–π or CH-π interactions. Incorporation of heteroatoms larger than carbon facilitate the overlap of π-orbital; especially the S-S interaction is known to enhance the hole mobility through this π-orbital overlap effect[24-26]. The crystal structure suggests the critical role of sulfur atoms on the molecular self-assembled structure as has been observed in the other molecular systems[8].

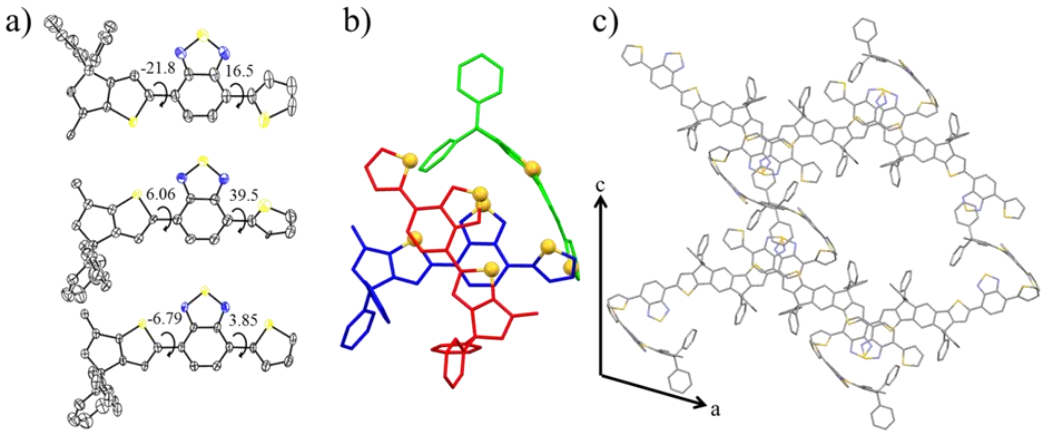

Fig. 5.8 Model structures solved by single crystal x-ray diffraction of di(HTh1BT)IDT: a)ORTEP image of crystallographically independent molecular units with ellipsoids drawn at 50% probability b) trimer structure with sulfur atoms in ball-and-stick model c) molecular packing structure perpendicular to b-axis. C, N, S atoms are shown as black, blue, and yellow, respectively. Alkyl chains and protons are omitted for clarity.

5.5.2 X-ray diffraction of DTCTT derivatives in crystal

Similar to the IDT derivatives, the DTCTT derivatives were also crystalized in the acetone/chloroform solvent vapor diffusion system and the ground crystals were used as samples for powder XRD. As shown in the XRD spectra (Fig. 5.9), both di(HTh1BT)DTCTT and di(HTh2BT)DTCTT show similar diffraction patterns. Major peaks of di(HTh1BT)DTCTT are seen at 2θ = 4.97, 8.29, 9.82, and 20.0 ° which corresponds to d spacing of 17.8, 10.7, 9.0, and 4.44 Å. For di(HTh2BT)DTCTT, peaks are seen at 2θ = 4.87, 8.40, and 20.1 ° which correspond to d-spacing of 18.1, 10.5, and 4.42 Å. On the other hand, di(C12Th2BT)DTCTT have a different XRD pattern, suggesting they form a different packing structure from them as molecules tend to minimize unfilled space. The elongated structure of di(C12Th2BT)DTCTT may change their crystal structure to accomodate the long dodecyl side chains.

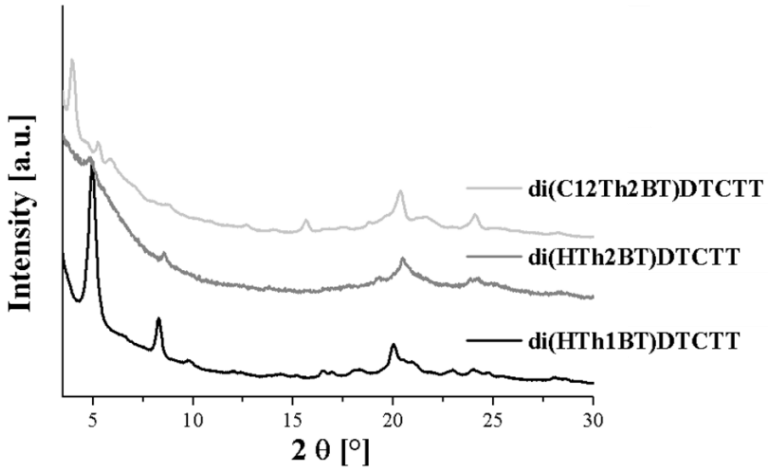

Fig. 5.9 Powder XRD patterns of DTCTT derivatives. The powder was prepared by grinding the crystals prepared from solvent vapor diffusion method with acetone/chloroform.

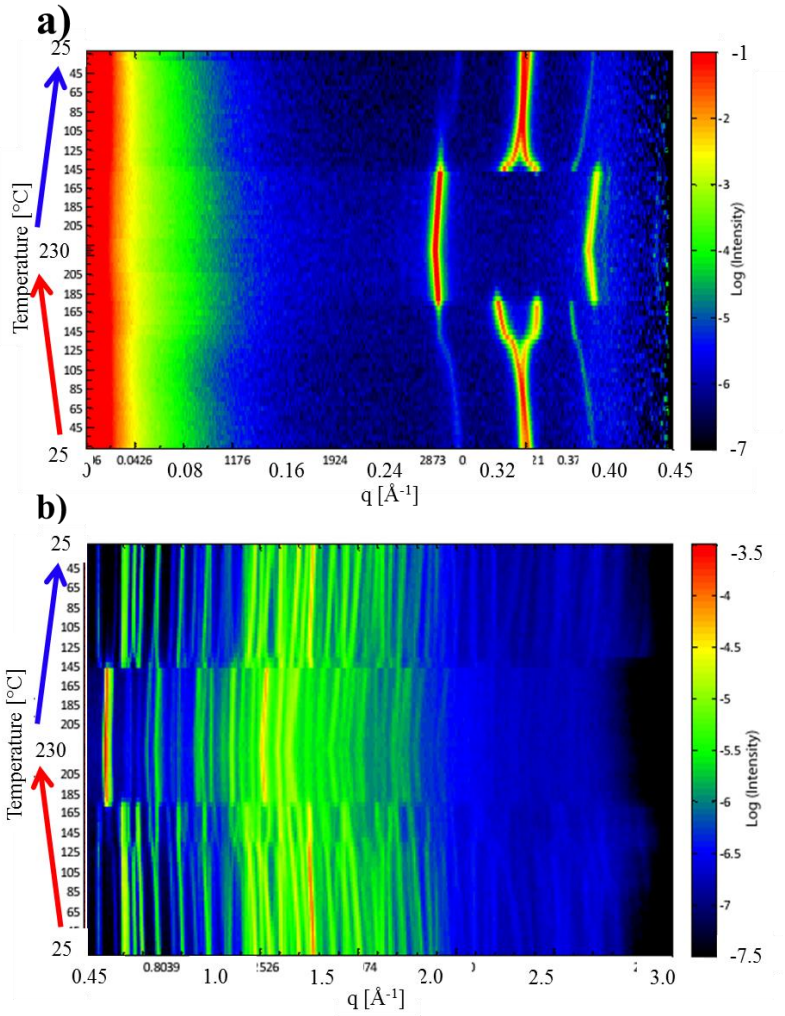

Fig. 5.10 X-ray scattering image of di(HTh2BT)DTCTT in the a) small angle regime and b) wide angle regime in color map at different temperatures. Scattering patterns were recorded by changing temperatures in a cycle of heating at 25 °C to 230 °C (before melting temperature) and cooling at 230 °C to 25 °C with a 5 °C step. Sample was prepared by first melting before slow cooled at rate of 10 °C/min. The intensity is depicted with color bar in logarithmic scale on each region.

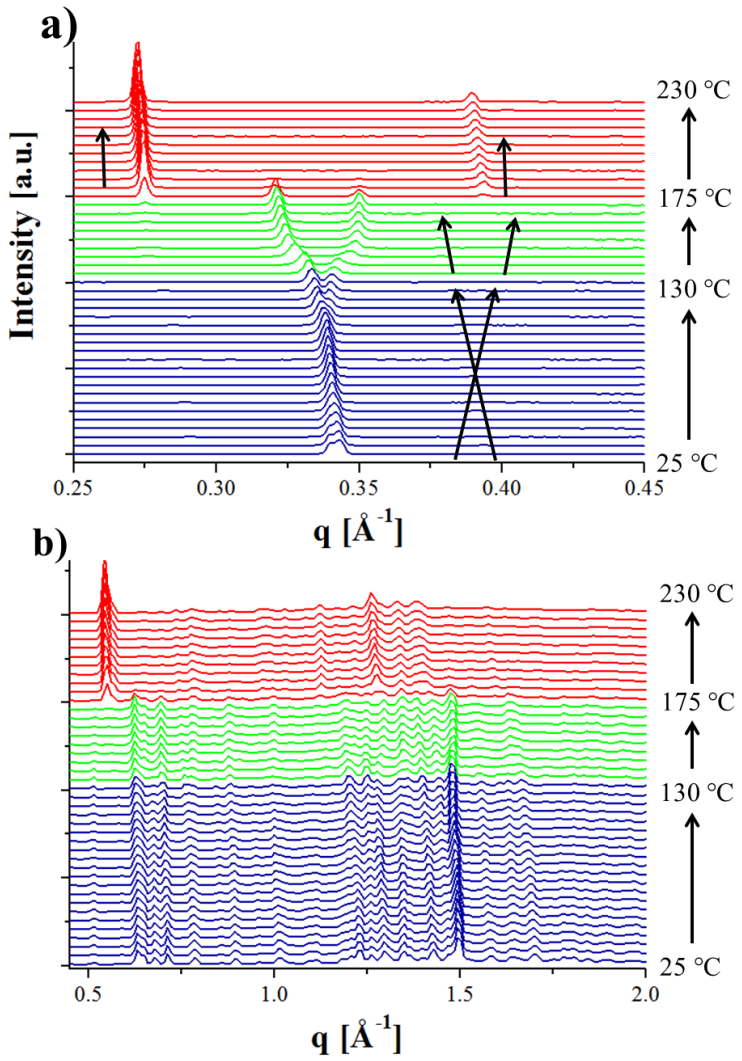

Fig. 5.11 X-ray scattering patterns of di(HTh2BT)DTCTT in the a) small angle regime and b) wide angle regime when heating from 25 °C to 230 °C with a 5 °C step (blue, green, and red color correspond to L, H1, and H2 phase, respectively). The intensity vs scattering vector q plots are derived from Fig. 5.10

The temperature-variable small and wide angle X-ray scattering (SWAXS) was performed to investigate the reversible phase transition behaviour of di(HTh2BT)DTCTT (R = R_2). The sample was firstly melted at 270 °C on a hot plate and then cooled at a rate of 10 °C/min, the same conditions as in the DSC

measurements presented earlier. The diffracted X-rays were recorded using a 2D detector and the diffractogram was generated by integrating their intensities with respect to the scattering vector. The diffraction was recorded at varying temperatures (from 25 to 230 °C and back to 25 °C) at a 5 °C step. As shown in the color map (Fig. 5.10), the three phases are clearly observed (L, H1, H2, and back to H1, L phases), corresponding well with the transitions seen in the DSC studies. For clarity, the diffraction patterns of only the heating up cycle, from 25 °C to 230 °C, are plotted in Fig. 5.11. At 25 °C which corresponds to the L phase, two peaks (q = 3.40 and 3.42 $Å^{-1}$) appears in the small angle regime. Upon heating, these peaks shift in a crossed manner, that is, one of the two peaks at 25 °C shifts to wide angle and another shifts to the other direction, even before the phase transition occurs. This shift of the peaks indicates the shrinkage and expansion of the lattice parameters. Around 130 °C, the phase transition from L to H1 phase takes place. However, the peaks at small angle regime still exhibit a continuous structural change throughout the heating process, and both peaks separate out further (q = 3.24 and 3.45 $Å^{-1}$) at 150 °C. Above 175 °C, a drastic structural change takes place and new peaks appeared (q = 2.73 and 3.89 $Å^{-1}$). Peaks in the wide angle regime (q = 1.25 – 1.5 $Å^{-1}$), which correspond to short-range order of aromatic groups (d = 4.19 – 5.03 Å), also changed their patterns, indicating a change in the packing mode. Over the whole temperature range, all the peaks in the small-angle regime have considerably higher intensity than those in the wide-angle regime, which implies a strong long-range order but weak short-range ordering. This feature, together with the fact that L to H1 phase transition takes place in a continuous manner, showed that this structural reorganization has very strong similarity to that of liquid crystalline materials. Attempts to assign each phase were made and are discussed in section 5.6.

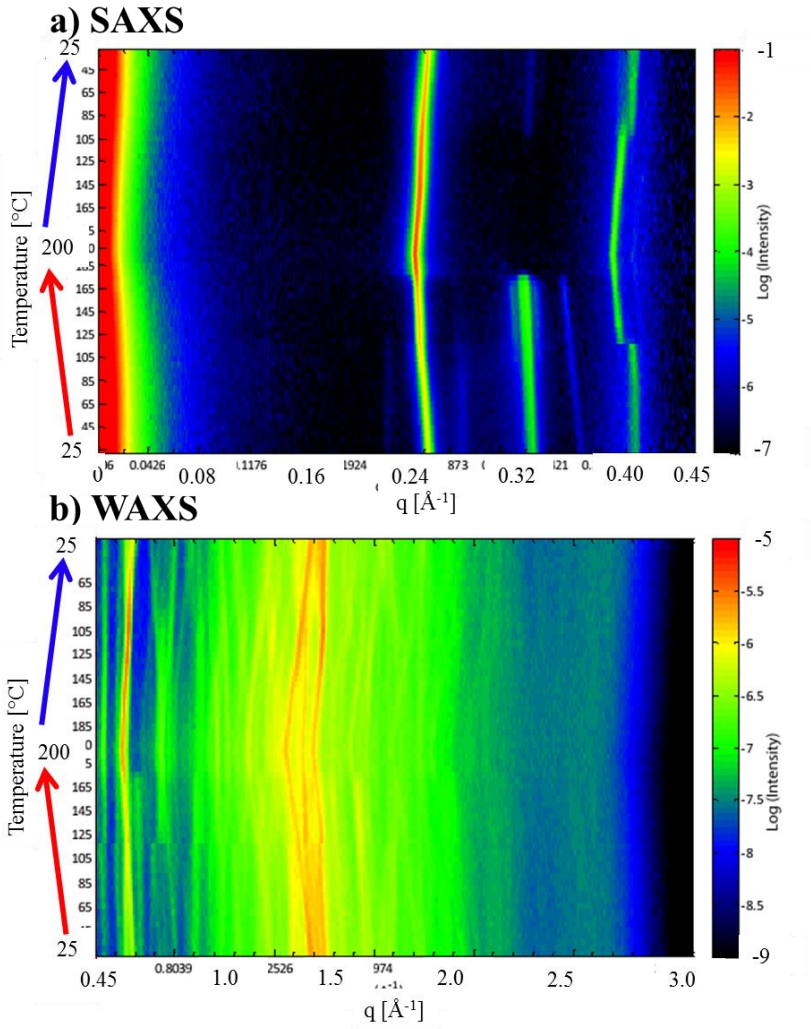

Fig. 5.12 X-ray scattering image of di(C12Th2BT)DTCTT in the a) small angle regime and b) wide angle regime in 2D plot at different temperatures vertical. Scattering patterns were recorded by changing temperature in a cycle of heating at 25 °C to 200 °C (before melting temperature) and cooling at 200 °C to 25 °C by 5 °C step. Sample was prepared by melt to slow cooling at rate of 10 °C/min beforehand. Intensity is depicted with color bar in logarithmic scale on each region.

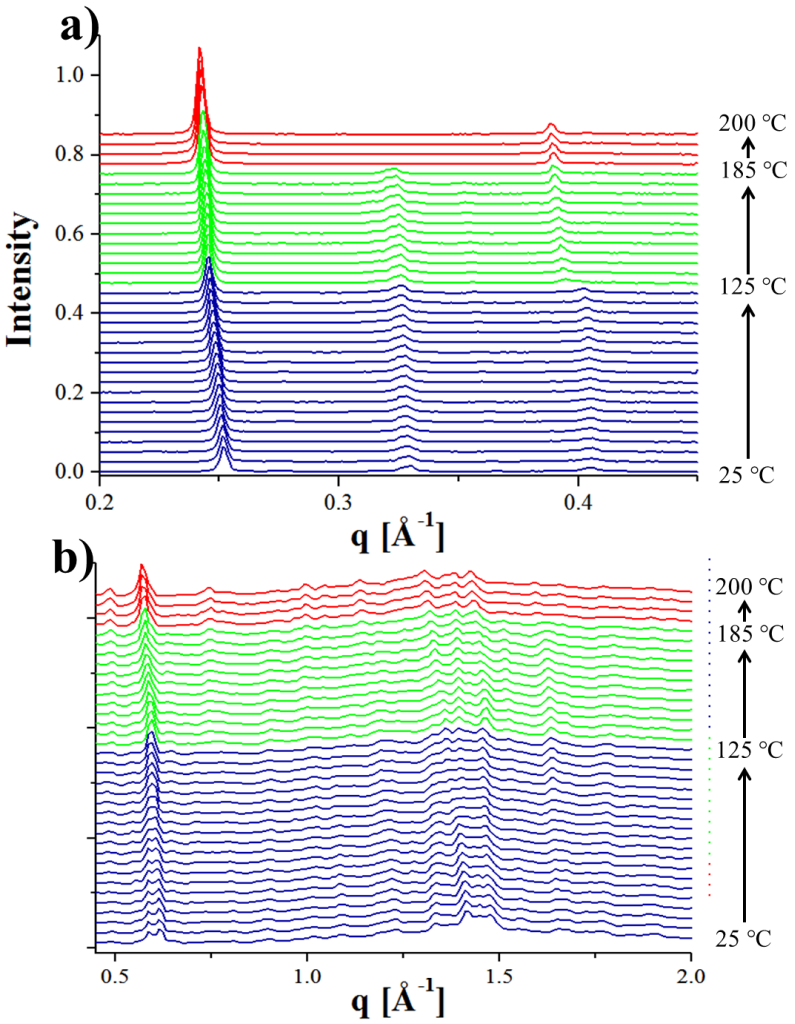

Fig. 5.13 Transmission X-ray scattering of di(HTh2BT)DTCTT in small angle and wide angle region at heating from 25 °C to 200 °C with a 5 °C step (blue, green, and red color correspond to L, H1, and H2 phase, respectively). The the intensity vs scattering vector q plots are derived from Fig. 5.12

The same measurement was performed for di(C12Th2BT)DTCTT (R = R_3). The sample was first melted at 250 °C and cooled at a rate of 10 °C/min, and then, the X-ray diffraction patterns were recorded during heating and cooling cycle (25 to 200 and back to 25 °C) (Fig. 5.12). Three major peaks (q = 0.25, 0.33, and 0.41 Å^{-1}) appear in the small angle regime at 30 °C, which gradually shifts to lower angle upon heating. At 125 °C, the phase transition from L to H1

takes place and the peak at 0.41 $Å^{-1}$ shows discontinuity (q = 0.24, 0.32, and 0.39 $Å^{-1}$ at 150 °C). Upon further heating, the phase transition of H1/H2 takes place and the middle peak disappears (q = 0.24 and 0.39 $Å^{-1}$ at 200 °C). This diffraction pattern of the H2 phase resembles that of di(HTh2BT)DTCTT at the high temperature. At the temperature, alkyl chains gains sufficient flexibility and freedom to move and thus, intermolecular interactions between the backbone structures become dominant for stabilizing the structure. Less contribution from the alkyl chains is assumed to result in the similar packing structure. On the cooling cycle, however, the middle peak intensity remains weak and distinct reversibility was not observed. In this measurement, cooling rate of 10 °C/min was applied to the sample but di(C12Th2BT)DTCTT showed scan-rate dependence in the DSC measurement. It seems the packing structure of di(C12Th2BT)DTCTT reorganizes more slowly compared to that of the di(HTh2BT)DTCTT. Due to the complexity of this kinetical factor, we mainly focused on the structural assignment of di(HTh2BT)DTCTT in the following discussion.

5.5.3 GI-SWAXS of di(HTh2BT)DTCTT in thin film

In the temperature variable SWAXS measurement of di(HTh2BT)DTCTT, clear and drastic reversible phase transition behavior was observed. In order to elucidate the self-assembled structure of the molecule in detail, Grazing-incidence small and wide angle X-ray scattering (GI-SWAXS) was performed on the thin film sample of di(HTh2BT)DTCTT. The thin film was prepared from chloroform:oDCB = 9:1 solution and was spin coated on silicon substrates at 1000 rpm (as-spun sample) and annealed at 200 °C for 5 min (annealed sample). The measurement was conducted at the Stanford Linear Accelerator Center (SLAC) using synchrotron X-ray source. In this set up, incident X-ray beam is irradiated onto the thin film sample at an angle close to the critical angle of the substrate, and the diffracted X-rays are collected to form 2D

patterns to in an attempt to elucidate any anisotropy in the sample. The as-spun film (Fig. 5.14a) diffracted a strong peak observed at d = 23.9 Å along Qz, or out-of-plane direction.

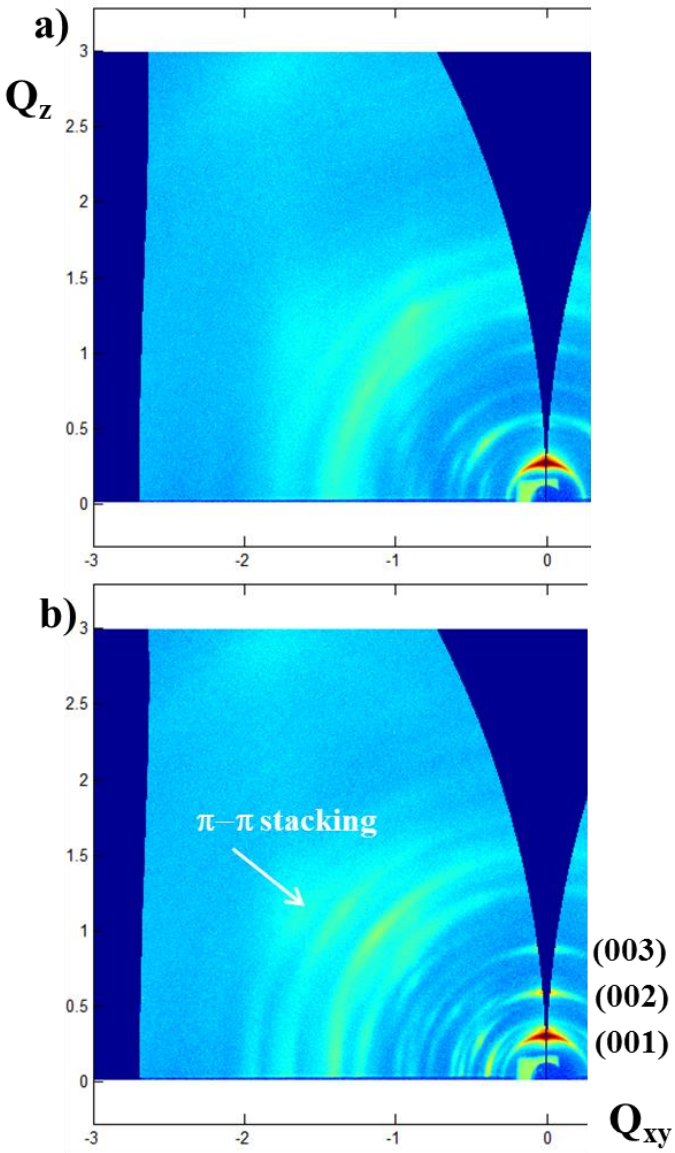

Fig. 5.14 2D GI-SWAXS diffraction patterns of di(HTh2BT)DTCTT of: a) as spun film and b) annealed film. The samples were prepared by spincoating from chloroform:oDCB = 9:1 solution and thermal annealing was done at 200 °C for 5 min. (Data was collected by Victoria Savikhin, Stanford SLAC)

Short-range peaks corresponding to distances of 3.5–5 Å, which are typical π–π stacking distances for aromatic molecules, are observed in between the Qxy-Qz directions and no such peaks are observed on the axis. These results imply that the molecules adopt an edge-on mode of packing structure with the π–π stacking in slip-stacked manner. In the annealed film (Fig. 5.14b), it is clear that molecular reorganization takes place as shown by the peak patterns becoming more distinctive. The strong peak along the out-of-plane direction (d = 23.9 Å in as-spun film) shifts to d = 21.4 Å with obvious multiples along the direction, indicating the lamellar structure of (001), (002) and (003) reflections. Broaden peaks (d = 3.5–5 Å in as-spun film) become more intense along a tilted direction with a certain degree of smearing. The annealed sample gives an insight into the thermodynamically stable form of the molecule. Thermal energy allows molecules to reorient into an ordered packing structure, having both a long-range lamellar structure and a short-range slip-stacked mode of π–π stacking.

5.6 Structural analysis of the molecular self-assembled structure of di(HTh2BT)DTCTT in the reversible phase transition states

Various X-ray diffraction techniques have been used to investigate the solid-state structure of di(HTh2BT)DTCTT in both powder and thin film forms. Temperature-variable XRD measurement revealed a unique reversible phase transition behavior with a continuous structural reorganization of L/H1 phase transition. GI-SWAXS data indicates a slipped-stacked type π–π stacking and lamellar structure in the out-of-plane direction. These results indicate a one-dimensional self-assembly to form the ordered structures (Fig. 5.15). In this section, the packing structure in the L, H1, and H2 of di(HTh2BT)DTCTT are discussed. The single unit of the molecular structure was optimized using DFT method with a hybrid function of B3LYP/6-31G(d,p). As shown in Fig. 5.15a, from the modeling, the molecule is found to have long axis of 49 Å along the

conjugation length and a short axis of 23 Å along the direction of the octyl phenyl groups. Since the structure has the flexibility in both conjugation length and alkyl chain directions, the shape of the unit structure can be represented as an ellipsoid. GI-SWAXS results indicate that molecules self-assemble in a slipped-stacked manner to form lamellar structures in the out-of-plane direction with a d-spacing of 21.4 Å for the annealed sample in thin film. Thus, it can be assumed that those molecular ellipsoids self-assemble to form one dimensionally organized structure with a diameter indicated by d (Fig. 5.15b) in thin film.

Several attempts were made to grow a large single crystal suitable for X-ray crystallography, but only small crystals were obtained. However, fiber-like crystals could be observed under atomic force microscope (AFM) (Fig. 5.16). It is worth noting that AFM only provides the surface information of the crystalline sample. Nonetheless, fiber-like crystals can be observed. The crystals were grown from mixed acetone and chloroform solution and were deposited on a glass substrate for measurement. Both height and phase images show in Fig. 5.16. The AFM image shows that these are the aggregation of fiber-like crystals, and these crystals have diameters of which are 50–200 nm. Crystals of π–conjugated molecules tend to grow along the π–stacking direction[27]. The crystal growth of di(HTh2BT)DTCTT is also assumed to be driven by the slipped-stacked π–π stacking which is clear difference from the di(HTh1BT)IDT crystal structure. The S-S interaction seems to play important contribution to stabilize the packing. The slipped-stacked dimer structure was also modelled using DFT calculation with the dispersion-corrected WB97XD function as a basis set. This function is suitable for calculating the intermolecular interaction accurately, especially for polycyclic aromatic hydrocarbons[28]. The 1D organized geometry shown in Fig. 5.15 with a diameter (d) of 23 Å was used as the initial coordination. The diameter was extracted from the diffraction peak in H2 phase.

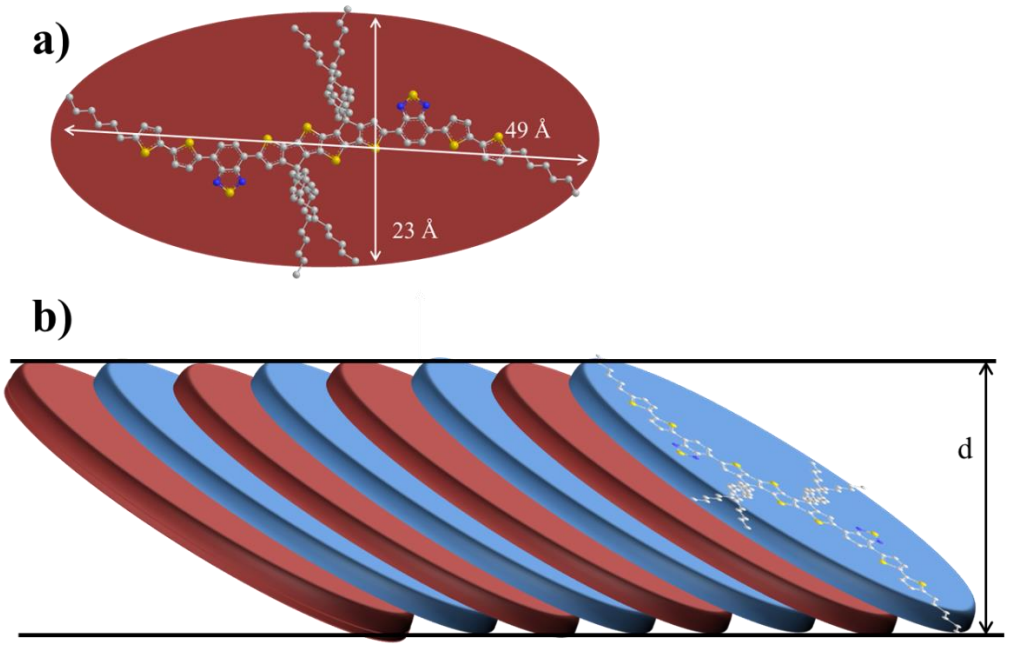

Fig. 5.15 Schematic illustration of the molecular self-assembly: a) optimized geometry of di(HTh2BT)DTCTT and b) plausible 1D organized molecular self-assembly of di(HTh2BT)DTCTT.

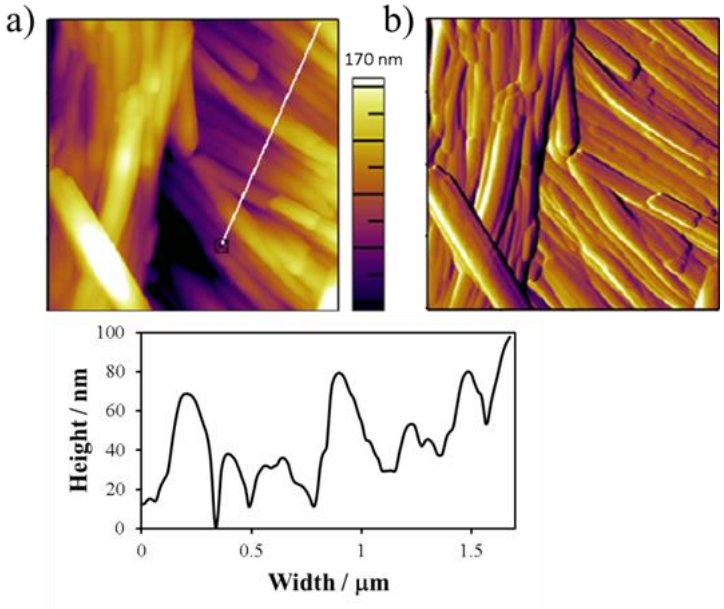

Fig. 5.16 AFM image (2 x 2 µm) of di(HTh2BT)DTCTT crystal prepared by solvent vapor diffusion with acetone/chloroform a) height image b)phase image c) cross sectional height image of the while line in a).

At high temperatures, alkyl chains have a high flexibility and the structure is believed to be more suitable geometry for the molecular simulation. A stable dimer structure is successfully stabilized and shown in Fig. 5.17. In the stabilized structure, the dimer has a close proximity on the central area. However, the distortion of the aromatic backbone is also observed and the end part of the side groups seems to have high flexibility as seen from the large distortion on the thiophenes.

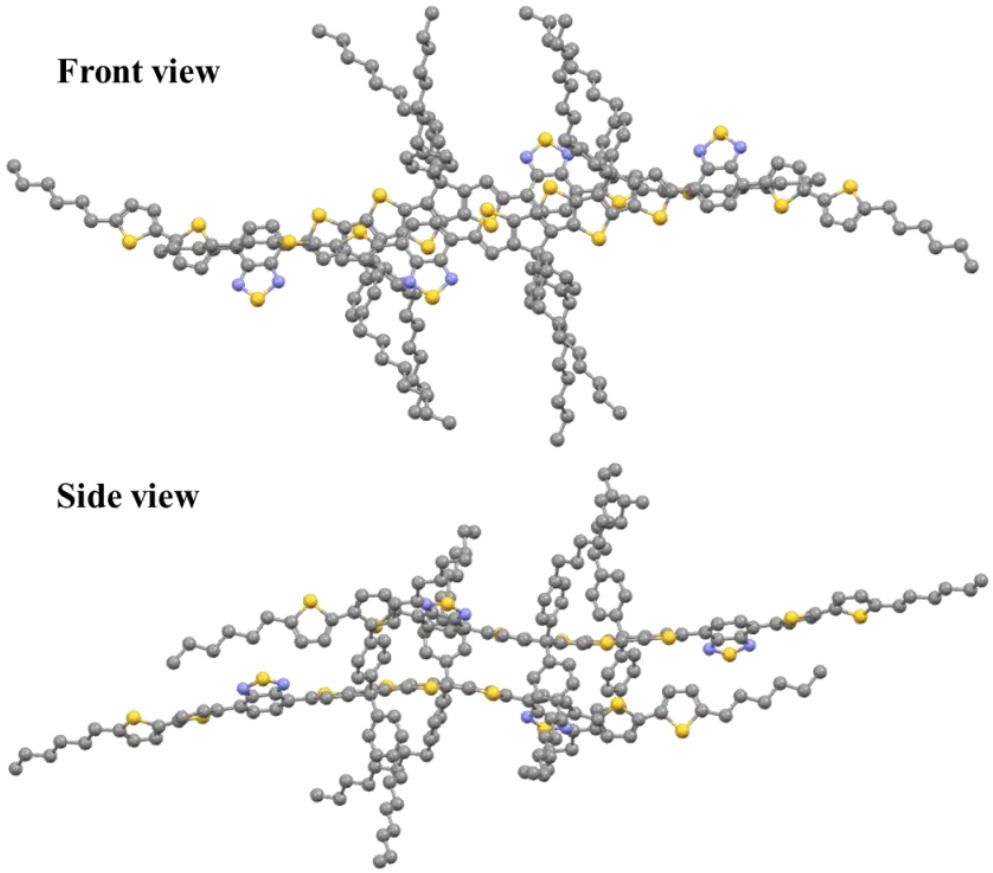

Fig. 5.17 Slipped-stacked dimer structure of di(HTh2BT)DTCTT. The structure was optimized using DFT calculation with WB97XD/6-31(d,p) as basis set. The 1D organized structure with the diameter 23 Å was used as an initial coordination.

The combination of the strong interaction between the central cores and high flexibility on the end parts of the side groups could be the reason for the unique reversible phase transition behavior. The fact that the Th1 derivative, di(HTh1BT)DTCTT, did not show such a phenomenon indicates that an additional thiophene ring plays a key role in imparting structural flexibility beneficial for the molecular reorganization.

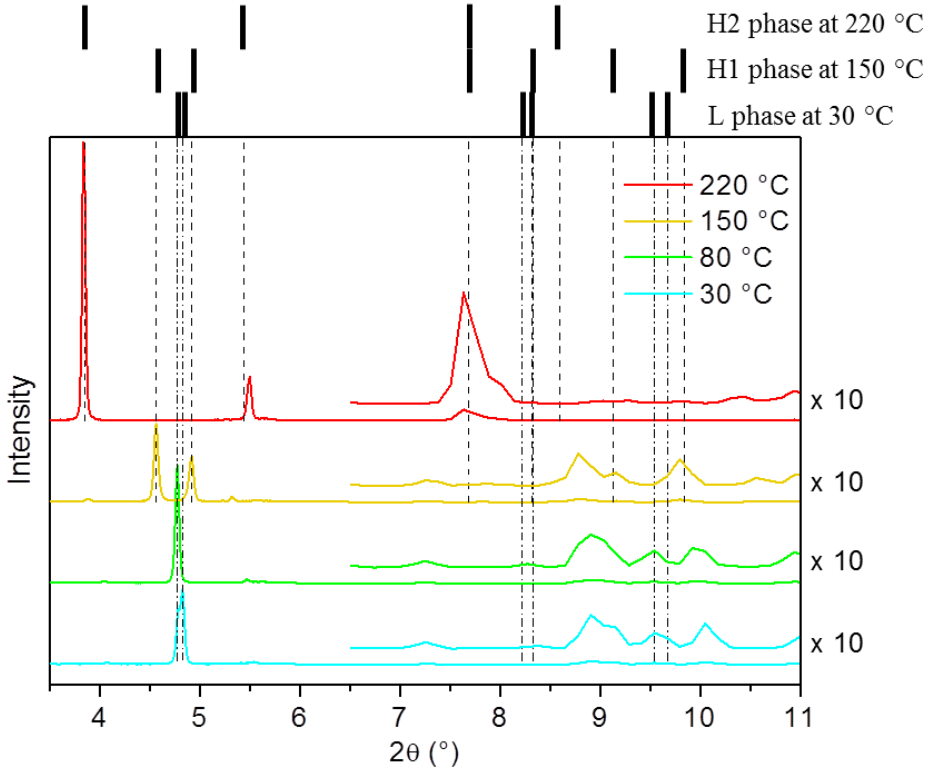

Fig. 5.18 Intensity vs 2θ plot of SWAXS data of di(HTh2BT)DTCTT at different temperatures. The data was taken from Fig. 5.11 and the calculated peak positions with each space group are shown as black lines.

Finally, the packing structures of the three phases (L, H1, and H2 phases) were analysed using structural data obtained in the temperature variable SWAXS measurement. Keeping the above discussion in mind, it is rational to think that the molecules form the 1D structure in each phase.

Table 5.3 X-ray diffraction data of di(HTh2BT)DTCTT at each temperature: the comparison of experimental and simulated phase from each space grouop

Phase	d_{obs}/ Å	d_{calcd}/ Å	Millar indices
L at 30 °C	18.5	18.5	(11)
C2mm	18.4	18.3	(20)
a= 36.6 Å	12.2	10.8	(02)
b= 21.5 Å	9.54	10.6	(31)
	9.27	9.27	(22)
	8.8	9.15	(40)
H1 at 150 °C	19.4	19.4	(11)
C2mm	18.2	18	(20)
a= 36.0 Å	12.2	11.5	(02)
b= 23.0 Å	10.1	10.6	(31)
	9.65	9.69	(22)
	9.03	9	(40)
H2 at 220 °C	23	23	(11)
P4mm	16.1	16.3	(20)
a= 23.0 Å	11.6	11.5	(02)
	11	10.3	(31)

In addition, the continuous phase transition behavior from L to H1 phase resembles the typical behavior observed for columnar liquid crystals[29-31]. In such systems, hexagonal (100) peak splits into tetragonal (110) and (200) peaks depending on the temperature. Thus, the diffraction patterns of di(HTh2BT)DTCTT crystal can be reasonably assumed as columnar phase with 2D symmetry (Fig. 5.18 and Table 5.3). Based on the assignment, the plausible packing structures of each phase are illustrated in Fig. 5.19. The L phase at 30 °C is a centred-rectangular phase (C2mm) with the lattice parameter a = 36.6 Å and b = 21.5 Å. Upon heating, the shrinkage of the a-axis and the expansion of b-axis take place and continuously transform to H1 phase with a = 36.0 Å and b = 23.0 Å at 150 °C. The diameter of the column is calculated to be around 21.5–23.0 Å, which is in good agreement with the slipped stacked geometry. The H1/H2 transition is a more dramatic transition and the H2 phase is assigned

as 2D rectangular shape with a = 23.0 Å at 220 °C. In this case, clusters of columns need to move among themselves to accommodate the molecular reorganization during the phase transition. Such a drastic motion is also assumed to induce mechanical stress and strain, and the cracks observed in the POM image can be attributed to this stress. It is worth noting that diameter of the column did not change (23 Å) but the peaks in the wide-angle region shifted to lower angle. This indicates that the molecules slip-stack differently but still maintain a 1D organization. As a whole, the columnar liquid crystal-like phase transitions can explain the reorganization of the packing structure and it matches well with the other experimental results with some unassigned. The three dimensional packing structure and structural defects such as rotational isomers could be the reason for the observed deviation. The XRD patterns of di(C12Th2BT)DTCTT can be also assigned as the similar columnar phases.

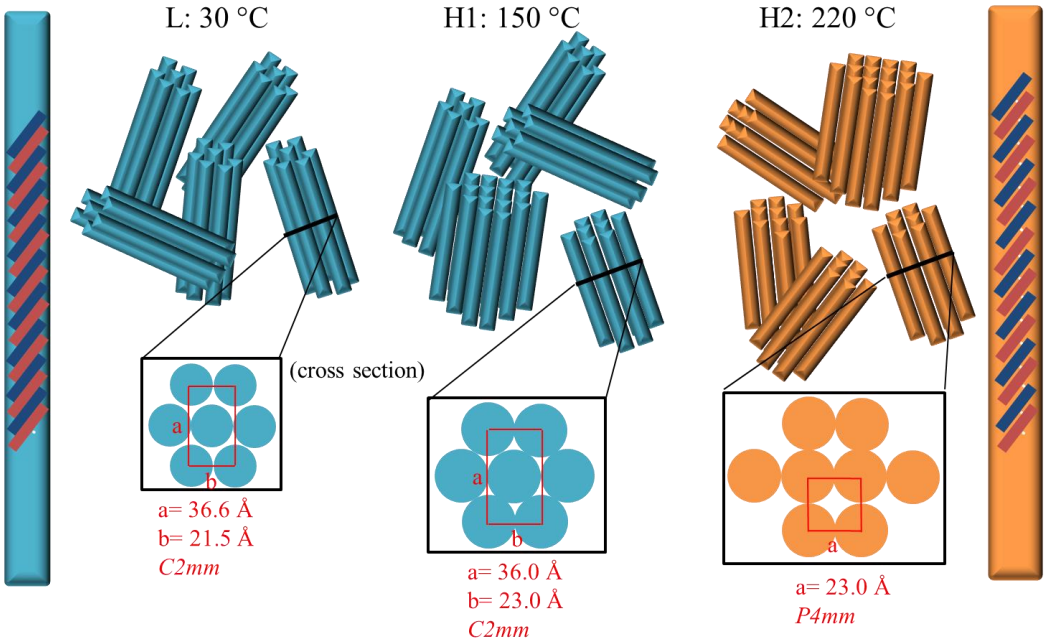

Fig. 5.19 Plausible explanation of reversible phase transition behavior of di(HTh2BT)DTCTT in L, H1, and H2 phase. The blue and orange columns represent the slipped-stacked form of the molecular self-assembly.

This unique solid-state character of DTCTT derivatives arises from the molecular structure which provides the combination of attractive forces through the core-core interaction, repulsive forces from bulky phenyl side groups, and rotational freedom of the thiophene end groups.

5.7 Charge transport properties

As seen in the previous section, hierarchical ordered structures can be observed for the derivatives of DTCTT. It will be useful to compare how structural order contributes to charge transport properties as this is an important property for its application in OPV. In order to investigate the effects of molecular structures and morphology on the transport properties, hole mobility of di(HTh2BT)IDT, di(HTh2BT)DTCTT and di(C12Th2BT)DTCTT was measured using OFET devices. The bottom-gate and bottom-contact device configuration with Au electrodes on doped-silicon substrate was used. The substrates were first treated with hexamethyldisilazane (HMDS) prior to the deposition of the solutions dissolved in chloroform: oDCB = 9:1 ratio. The devices were prepared and tested inside a glove box. After the devices were tested, they were subsequently annealed at 100 °C for di(HTh2BT)IDT and 200 °C for both DTCTT samples and then, tested again. Transfer characteristics of as-spun and annealed samples are shown in the a), c), e) and Output characteristic of annealed samples are shown in b), d), f) of Fig. 5.20 for di(HTh2BT)IDT, di(HTh2BT)DTCTT, di(C12Th2BT)DTCTT, respectively. The mobility values were calculated from the slope of the curve in the transfer characteristics using the Shockley equation[29] as discussed in Chapter 3. Comparing the as-spun samples and annealed samples, hole mobility values do not change significantly. However, annealed samples show high reproducibility among the different devices, presumably due to a more uniform molecular organization. All output characteristics exhibit typical transistor-like behavior with saturation at high drain-source voltage. Four devices with a channel length of 20 μm were

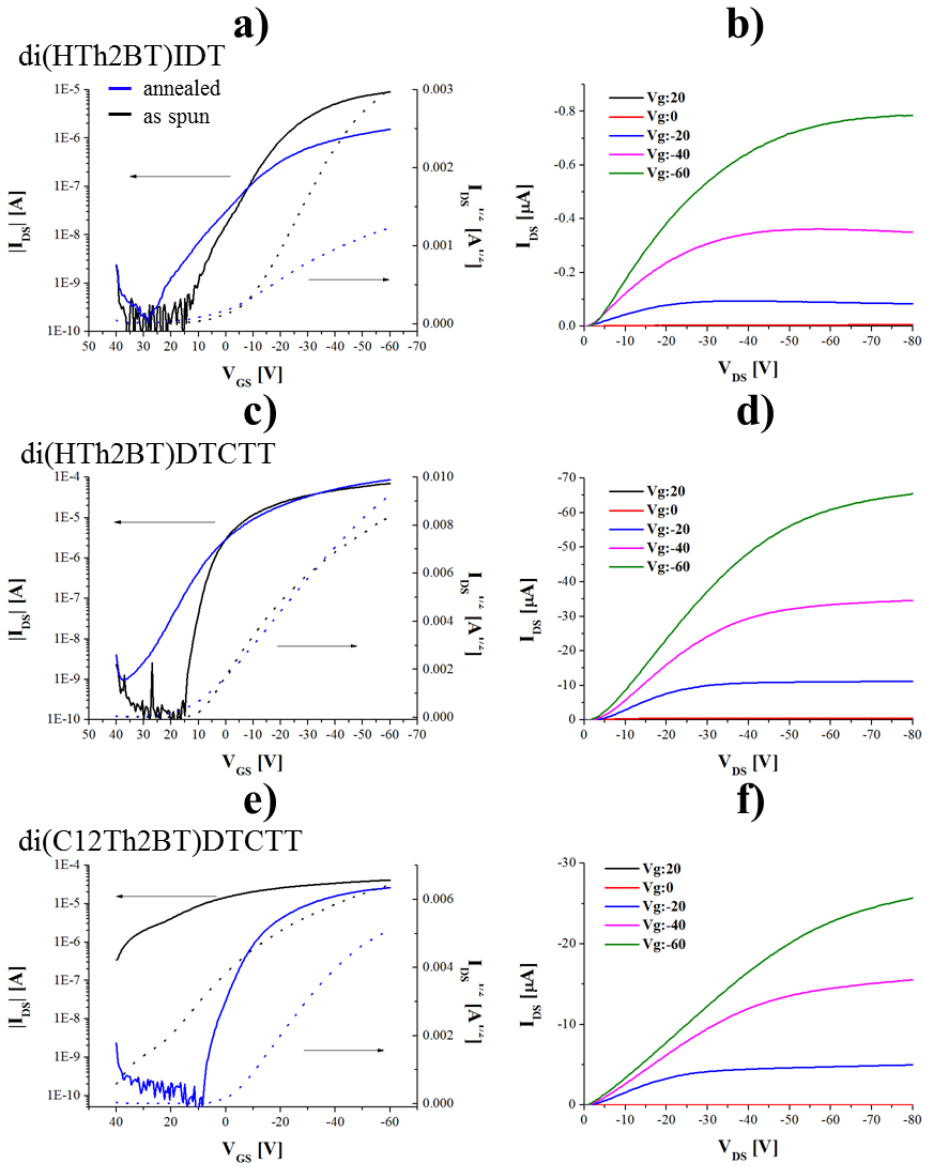

Fig. 5.20 OFET characteristics of di(HTh2BT)IDT, di(HTh2BT)DTCTT and di(C12Th2BT)DTCTT in thin film of a,c,e) Transfer characteristic of both the as spun film (black) and the annealed film (blue) and b,d,f) Output characteristic of annealed samples. Thermal treatment at 100 °C for di(HTh2BT)IDT and 200 °C for both the DTCTT derivatives were applied for annealed samples.

prepared and their average mobility values are 3.0 x 10^{-4}, 1.9 x 10^{-2}, and 1.0 x 10^{-2} $cm^2/V \cdot s$ for the di(HTh2BT)IDT, di(HTh2BT)DTCTT, and di(C12Th2BT)DTCTT, respectively. For di(HTh2BT)IDT, the value is typical for amorphous materials,[30] correlating well with the amorphous nature shown by XRD measurements. For both DTCTT derivatives, higher hole mobility values were obtained. Considering these are only preliminary results without any optimization, the increase of two order in magnitude is an encouraging result. This is attributed to the extended conjugation of fused-ladder type DTCTT backbone structure as well as the more favorable 1D organized structure. Recently, H. Iino and co-workers demonstrated a spincoating optimization strategy to access the Smetic E (SmE) phase of a liquid crystalline material[31]. The SmE phase has one of the most ordered packing structure among the other mesophases and they could achieve enhanced charge career mobility value. It will be interesting to see the effect of different 1D organization structure for the DTCTT derivatives can give rise to earn better charge transport behavior, which will be part of the future work of this study.

5.8 Short summary

We have made fused-ladder thienoarenes, the DTCTT and IDT, substituted with benzothiadiazole and alkyl thiophene side groups. DSC measurement revealed the rich solid-state phases of the system depending on the central core and end group structures. The crystal structure of di(HTh1BT)IDT solved by single crystal XRD explained an amorphous nature of the IDT-based molecules; the bulky hexylphenyl side groups result in a distorted intramolecular conformation and the lack of the $\pi-\pi$ stacking. The S-S interactions seem to play an important role in stabilizing the structure of this molecular system having highly bulky side groups. On the other hand, the crystallinity of the DTCTT derivatives extended due to the incorporation of thienothiophene unit.

In the presence of the flexible side groups (R = R_2 and R_3), an unusual reversible phase transition behavior was observed. The crystal-to-crystal phase transitions with continuous (L/H1) and discontinuous (H1/H2) phase transition were investigated in detail. Both experimental and computational results revealed the slip-stacked mode of π-stacking, forming columnar 1D organization, and each phase was assigned with 2D symmetricity of the structure. A combination of both the strong core-core interactions in the slip-stacked form and the flexibility of side groups was assumed to be the key factor for enhancing the molecular reorganization. The 1D organization and lamellar structures formed parallel to substrate is favorable to charge transport in the thin film. As a result, the hole mobility of 1.9 x 10^{-2} $cm^2/V{\cdot}s$ was obtained for the di(HTh2BT)DTCTT in OFET device, which is two order of magnitude higher than 3.0 x 10^{-4} $cm^2/V{\cdot}s$ of amorphous di(HTh2BT)IDT film. It is believed that this research opens up an interesting possibility of developing stimuli-responsive organic semiconductors.

CCDC 1504077 contains the supplementary crystallographic data for this paper. This data can be obtained free of charge from The Cambridge Crystallographic Data Centre via www.ccdc.cam.ac.uk/data_request/cif.

Reference:

[1] Z.B. Henson, K. Mullen, G.C. Bazan, *Nat Chem* 4 **(2012)** 699.

[2] Y. Chen, X. Wan, G. Long, *Accounts of Chemical Research* 46 **(2013)** 2645.

[3] Y. Liu, C.C. Chen, Z. Hong, J. Gao, Y.M. Yang, H. Zhou, L. Dou, G. Li, Y. Yang, *Sci Rep* 3 **(2013)** 3356.

[4] T.S. van der Poll, J.A. Love, T.Q. Nguyen, G.C. Bazan, *Adv Mater* 24 **(2012)** 3646.

[5] B. Kan, Q. Zhang, M. Li, X. Wan, W. Ni, G. Long, Y. Wang, X. Yang, H. Feng, Y. Chen, *J Am Chem Soc* 136 **(2014)** 15529.

[6] J.E. Coughlin, A. Zhugayevych, R.C. Bakus, T.S. van der Poll, G.C. Welch, S.J. Teat, G.C. Bazan, S. Tretiak, *The Journal of Physical Chemistry C* 118 **(2014)** 15610.

[7] T.S. van der Poll, A. Zhugayevych, E. Chertkov, R.C. Bakus, 2nd, J.E. Coughlin, S.J. Teat, G.C. Bazan, S. Tretiak, *J Phys Chem Lett* 5 **(2014)** 2700.

[8] A. Zhugayevych, O. Postupna, R.C. Bakus Ii, G.C. Welch, G.C. Bazan, S. Tretiak, *The Journal of Physical Chemistry C* 117 **(2013)** 4920.

[9] J.A. Love, C.M. Proctor, J. Liu, C.J. Takacs, A. Sharenko, T.S. van der Poll, A.J. Heeger, G.C. Bazan, T.-Q. Nguyen, *Advanced Functional Materials* 23 **(2013)** 5019.

[10] C.M. Proctor, J.A. Love, T.-Q. Nguyen, *Adv Mater* 26 **(2014)** 5957.

[11] H. Chung, Y. Diao, *Journal of Materials Chemistry C* 4 **(2016)** 3915.

[12] T. Wombacher, A. Gassmann, S. Foro, H. von Seggern, J.J. Schneider, *Angew Chem Int Ed Engl* 55 **(2016)** 6041.

[13] L. Zhang, N.S. Colella, B.P. Cherniawski, S.C. Mannsfeld, A.L. Briseno, *ACS Appl Mater Interfaces* 6 **(2014)** 5327.

[14] G.E. Purdum, N. Yao, A. Woll, T. Gessner, R.T. Weitz, Y.-L. Loo, *Advanced Functional Materials* 26 **(2016)** 2357.

[15] A.O.F. Jones, B. Chattopadhyay, Y.H. Geerts, R. Resel, *Advanced Functional Materials* 26 **(2016)** 2233.

[16] Y. Diao, K.M. Lenn, W.Y. Lee, M.A. Blood-Forsythe, J. Xu, Y. Mao, Y. Kim, J.A. Reinspach, S. Park, A. Aspuru-Guzik, G. Xue, P. Clancy, Z. Bao, S.C. Mannsfeld, *J Am Chem Soc* 136 **(2014)** 17046.

[17] J. Chen, M. Shao, K. Xiao, A.J. Rondinone, Y.-L. Loo, P.R.C. Kent, B.G. Sumpter, D. Li, J.K. Keum, P.J. Diemer, J.E. Anthony, O.D. Jurchescu, J. Huang, *Nanoscale* 6 **(2014)** 449.

[18] J. Chen, M. Shao, K. Xiao, Z. He, D. Li, B.S. Lokitz, D.K. Hensley, S.M. Kilbey, J.E. Anthony, J.K. Keum, A.J. Rondinone, W.-Y. Lee, S. Hong, Z. Bao, *Chemistry of Materials* 25 **(2013)** 4378.

[19] Y. Tobe, N. Utsumi, K. Kawabata, A. Nagano, K. Adachi, S. Araki, M. Sonoda, K. Hirose, K. Naemura, *J Am Chem Soc* 124 **(2002)** 5350.

[20] P.A. Korevaar, C. Schaefer, T.F. de Greef, E.W. Meijer, *J Am Chem Soc* 134 **(2012)** 13482.

[21] R.A. Sullivan, R.J. Davey, G. Sadiq, G. Dent, K.R. Back, J.H. ter Horst, D. Toroz, R.B. Hammond, *Crystal Growth & Design* 14 **(2014)** 2689.

[22] J.E. Coughlin, Z.B. Henson, G.C. Welch, G.C. Bazan, *Accounts of Chemical Research* 47 **(2013)** 257.

[23] C.J. Takacs, Y. Sun, G.C. Welch, L.A. Perez, X. Liu, W. Wen, G.C. Bazan, A.J. Heeger, *J Am Chem Soc* 134 **(2012)** 16597.

[24] I. McCulloch, M. Heeney, C. Bailey, K. Genevicius, I. Macdonald, M. Shkunov, D. Sparrowe, S. Tierney, R. Wagner, W. Zhang, M.L. Chabinyc, R.J. Kline, M.D. McGehee, M.F. Toney, *Nat Mater* 5 **(2006)** 328.

[25] K. Takimiya, I. Osaka, T. Mori, M. Nakano, *Acc Chem Res* 47 **(2014)** 1493.

[26] J.I. Park, J.W. Chung, J.Y. Kim, J. Lee, J.Y. Jung, B. Koo, B.L. Lee, S.W. Lee, Y.W. Jin, S.Y. Lee, *J Am Chem Soc* 137 **(2015)** 12175.

[27] F.J.M. Hoeben, P. Jonkheijm, E.W. Meijer, A.P.H.J. Schenning, *Chem Rev* 105 **(2005)** 1491.

[28] A. Yadav, P.C. Mishra, *Molecular Physics* 112 **(2014)** 88.

[29] W. Shockley, W.T. Read, *Physical Review* 87 **(1952)** 835.

[30] Y. Shirota, H. Kageyama, *Chem Rev* 107 **(2007)** 953.

[31] H. Iino, T. Usui, J. Hanna, *Nat Commun* 6 **(2015)** 6828.

Chapter 6

Implications/Impact/Outstanding Questions

Research findings in this thesis indicate both successful outcomes and issues to be solved in the future. In this chapter, those outcomes were summarized and challenges for the future were proposed. Novel donor materials, the DTCTT-based small molecules, were synthesized and their structure/property relationships were investigated. Aims and scopes of incorporating thienothiophene unit resulted in an enhanced organization due to the S-S interaction and suitable material properties for solar cell application. The results from the X-ray diffraction studies provided a qualitative understanding of the molecular self-assembled structure. However, the sm-OPV device performance remained moderate. Several molecular engineering proposals were presented for improving the performance. Overall, research pursuit in this thesis provided qualitative discussion of the structure/property relationship. Findings and outcome in this thesis will contribute to further development of efficient organic semiconducting materials using rational designing strategy.

6.1 Summary

In Chapter 4, novel donor material, di(HTh2BT)DTCTT, was designed and synthesized for application in sm-OPV materials. In order to increase the range of light absorption and to achieve a high charge carrier mobility, a thienothiophene unit was incorporated into the central core of fused-ladder aromatic backbone. The effect of this modification was investigated and compared to the counterpart, di(HTh2BT)IDT which has a benzene unit in the core instead. The DTCTT donor demonstrated improved properties: red-shifted absorption, enhanced crystallinity, higher thermal stability, and higher hole mobility than the IDT donor. They were then incorporated into sm-OPV device while blended with fullerene acceptors. Although the DTCTT donor showed promising structural and optoelectronic properties, the device performance was 2.8% PCE, inferior to 3.2% PCE of the device incorporated with the IDT donor. The device analysis indicated two reasons for this inferior performance: 1) the reduced crystallinity when blended with fullerene acceptors and 2) rough and uneven surface morphology which could result in pin-holes in the film. In addition, Voc of the device was 0.2 V lower than the device incorporated with the IDT donor. This voltage drop corresponds to the difference in the estimated HOMO level between the DTCTT and IDT donor (-4.95 and -5.18 eV, respectively). Is is suggested that further structural modification is necessary to promote an effective crystallization and uniform film morphology. Findings in Chapter 4 clarified factors need to be taken into account for designing high efficient OPV materials.

In an attempt to elucidate the impact of molecular structure of both the DTCTT and the IDT on the solid-state structure, X-ray diffraction techniques were used to the derivatives. Several derivatives were synthesized with varying the side group structures; the number of the thiophene rings and the length of alkyl chains were modified. The crystal structure of di(HTh1BT)IDT solved by X-ray

crystallography suggested reasons for amorphous nature of the IDT derivatives in thin film arisen from the lack of π–π stacking and the disordered conformation of the side groups. S-S interaction seems to play an important role to stabilize the structure. The S-S interaction could also explain the enhanced crystallinity of the DTCTT derivatives in both powder and thin film state due to the additional interactions through the thienothiophne unit. In addition, two DTCTT derivatives exhibited unique reversible phase transition behavior, and that of di(HTh2BT)DTCTT was investigated in details. Both experimental and computational results revealed the slip-stacked mode of π-stacking, forming columnar 1D organization, and each phase was assigned with 2D symmetricity of the structure. A combination of both the strong core-core interactions in the slip-stacked form and the flexibility of side groups was assumed to be the key factor for enhancing the molecular reorganization. The 1D organization and lamellar structures formed parallel to substrate is favorable to charge transport in the thin film. As a result, the hole mobility of 1.9 x 10^{-2} $cm^2/V \cdot s$ was obtained for di(HTh2BT)DTCTT in OFET device is, which is two order of magnitude higher than 3.0 x 10^{-4} $cm^2/V \cdot s$ of amorphous di(HTh2BT)IDT. Findings in Chapter 5 revealed the unique self-assembled structure in detail. It is believed that further structural modification and crystal engineering could lead to enhanced performance in solar cell devices.

In a summary, the outcomes and the unsolved questions regarding the initial scope were addressed.

Outcomes

- Molecular engineering by the incorporation of thienothiophene moiety resulted in suitable properties for OPV application with respect to extended light harvesting ability, a high thermal stability, enhanced crystallinity, and a good charge transport ability.

- This attempt made efficient p-type semiconductors of which hole mobility is 1.6 x 10^{-3} and 1.9 x 10^{-2} $cm^2/V \cdot s$ estimated by hole-only device and OFET device, respectively.
- The sm-OPV devices were successfully fabricated with power conversion efficiency of 2.8%.
- S-S interaction plays important role for determining a packing structure
- The self-assembled structure of the DTCTT-based molecules was elucidated. They form slip-stacked mode of self-assembly with fibrous crystallization habit.
- Unusual crystal-to-crystal reversible phase transition behavior was discovered and the plausible mechanism of the liquid crystal-like molecular reorganization was proposed.

Unsolved questions

- Despite of the suitable properties in the application of sm-OPV and device optimization work, the device performance was moderate. The film-forming ability was poor and the crystallinity was reduced when blended with fullerene acceptors. Low Voc and FF resulted in moderate PCE of 2.8%. These results originate from designing strategy of the molecular structure and modification is necessary for a high performance device.
- X-ray diffraction peaks showed high intensity at small angle but considerably low intensity and wide peak width at wide angle region, implying disordered short-range order. Enhancing the order of magnitude may lead to better crystallinity and charge transport properties.
- Unique reversible phase transition behavior was discovered but it only appears through melt-slow cooling in crystal. Crystal engineering such as crystallization of thin-film using external-stimuli will open a wide application.

6.2 Proposal of molecular engineering in the future

The DTCTT-based molecule has a versatile structure (Fig. 6.1) of which can be modified by redesigning the synthetic scheme. Based on findings and outcomes in this thesis, possible targets of molecular structures for further improvement in the device performance are presented.

1) Introduction of fluorine atoms into benzothiadiazoles.
2) Replacement of octylphenyl groups into less bulky and flexible groups
3) Add functionality to alkyl chains in the end position.

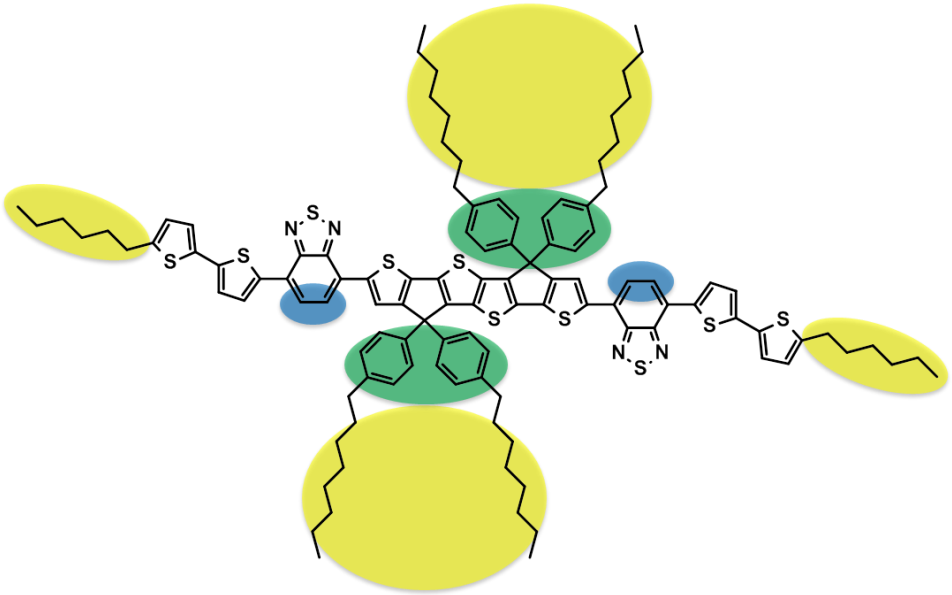

Fig. 6.1 Versatile structure of DTCTT-based small molecule

6.2.1 Introduction of fluorine atoms

Fluorine atom has a very high electron affinity and the incorporation into aromatic conjugation, especially into electron negative benzothiadiazole moiety, will be expected to lower both the LUMO and HOMO level. The energy band positions used in OPV devices are depicted in Fig. 6.2. Lower HOMO/LUMO level of the DTCTT molecules is favorable to increase the Voc. The Jsc will

also increase by forming ohmic contact with both cathode and anode materials. In addition, electron negative fluorine substitute can form the coulombic interactions with electron-rich sulfur atom in the DTCTT backbone, which will stabilize the intramolecular conformation. This effect is discussed and attempted in several small molecular donor molecules, resulting in improved performance in OPV devices[1-5]. According to reports from other groups[6,7], enhanced crystallinity in the presence of fullerene acceptors were also observed, which was one of remaining challenges of di(HTh2BT)DTCTT in this thesis. In recent years, kinetics of crystallization during spin-coating process has attracted much attention because spin-coating is an essential step for fabricating high performance solar cells. This step will determine the degree of crystallinity, D-A morphology, domain purity of donor and acceptor materials, and grain size[8,9]. Balance of those parameters affects the final device performance. In addition, some reports suggest existence of liquid crystal phase during the spin-coating process[10,11]. It is intrigued to see the crystallization kinetics of the DTCTT-based small molecules with fluorine substitutes as the DTCTT derivatives having two thiophene rings in the side group structure exhibited liquid crystal-like self-assembly and phase transitions.

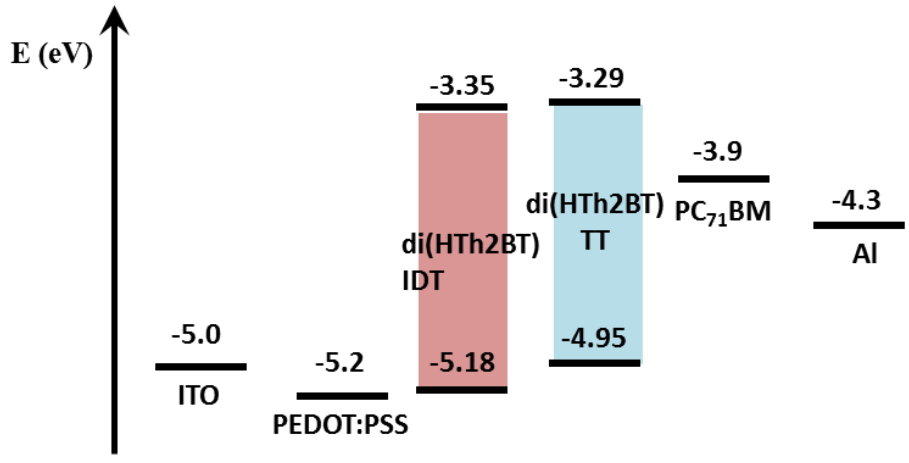

Fig. 6.2 Energy band diagram of materials used in OPV device

The synthesis of the DTCTT-based small molecule incorporated with fluorine atom is being carried out. Since the coupling reaction of the DTCTT backbone and side groups uses Suzuki reaction, the fluorinated side groups with boronic acid ester functional group need to be prepared. The conventional palladium-catalyzed Suzuki Miyaura borylation reaction was tried but it did not work for this system. This failed result is possibly because the electron negative fluorine atoms hampered the efficient conversion (Scheme 6.1). Currently, the iridium-catalyzed C-H borylation reaction is proposed to apply into this system. In fact, this reaction condition was applied for the preparation of 2,1,3-benzothiadiazole-4,7-bis(boronic acid pinacol ester) and the report indicated the reaction yield was higher than that of Suzuki Miyaura borylation reaction[12].

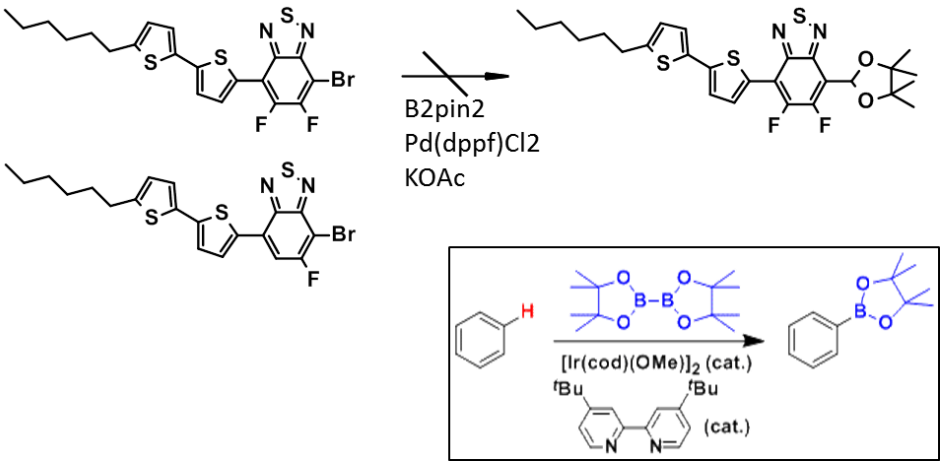

Scheme 6.1 Synthetic scheme of fluorobenzothiadiazole pinacol borate intermediate via Suzuki borylation reaction. The reaction condition of irdium-catalyzed C-H borylation reaction is also presented in inset.

6.2.2 Replacement of bulky octylphenyl groups

The result in X-ray crystallography of di(HTh1BT)IDT indicated the bulky phenyl groups attaching to the sp3 carbon of the backbone structure prevents efficient π–π stacking. Although these groups have a possible contribution into

a good solubility and the unique reversible phase transition behavior of the DTCTT derivatives, its bulkiness can potentially disrupt a close packing structure. As a result, it is detrimental to a good charge transport. The attempts to change such bulky phenyl groups to long and branched alkyl chains were tried on the IDT-based small molecular donor materials[13,14]. This attempt resulted in a significant improvement of the device performance, especially for the fill factor. The problem associated with this molecular design is that new synthetic route has to be tested for the preparation. As for synthesis of the DTCTT backbone, the ring closure reaction between peripheral thiophene and thienothiophene groups is radical-mediated reaction. The radicalized intermediates can be stabilized by benzene rings but no such effect comes from saturated alkyl groups. Redesigning the synthetic route is necessary to synthesize the DTCTT backbone having flexible alkyl chains on the sp3 carbon. A more realistic option would be Octylthiophene side group which is beneficial for both a good solubility and the closer π–π stacking structure and it can be synthesized through the conventional reaction scheme due to the aromaticity of the thiophene ring.

6.2.3 Modification of alkyl chains in the end position.

Structural investigation of the DTCTT derivatives revealed that the molecules are assembled in a slip-stacked manner of π–π stacking. Among weak intermolecular interactions which contribute to stabilize the structure, the S-S interactions are assumed to be especially important as was indicated by the single crystal X-ray crystallography of the di(HTh1BT)IDT. However, other interactions such as the van der Waals interactions between long alkyl chains could also play a role to stabilize the one-dimensional columnar organization. Replacement of C6 and C8 alkyl chains can affect the columnar structure. Alkyl chain length has been shown to affect the self-assembled structure, solubility, and the morphology of the film, which can ultimately influence the device

performance[14-16]. The introduction of polar chains, such as ethylene glycol chains, adds polar character onto the molecule. This modification is frequently used to control the self-assembly and supramolecular structures[17-19] by guiding through the hydrophobic and hydrophilic interactions. Long range order in fibrous structures, which could be stabilized by these side chain modifications, is beneficial for an efficient charge transport.

6.3 Application of reversible phase transition behavior

Unique reversible phase transition behavior was observed for the di(HTh2BT)DTCTT and di(C12Th2BT)DTCTT. The flexible molelcular reorganization seems to be arisen from combination of the attractive forces from the slip-stacked π–π interaction in the core structure and repulsive forces from rotational freedom of the side groups. The structural flexibility resulted in a reversible color change in the thin film sample according to temperature as was observed in optical microscope(Fig. 6.3),. This will be seen as the change of distance between the π–conjugated molecules at each temperature. It can be used as a smart sensor application that a molecular system which can change its ordered packing structure reversibly under particular environmental stimuli. One such example is the plastic crystals[20,21]; their various properties have been studied from both fundamental interests and possible application in energy devices[20-22]. In the DTCTT-based small molecules, different properties are expected on each crystalline phase. The L, H1, and H2 state should have different charge carrier mobility arisen from different mode of the packing structure. Currently, the reversible phase is only presented in crystals formed by slow melt-cooling. This will limit the application as organic crystals are mechanically brittle. Further crystal engineering enables them to form the reversible phase in thin film which open up possibility in various applications.

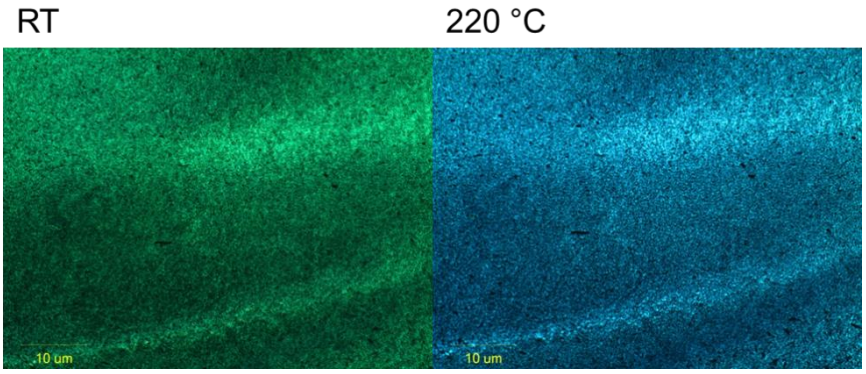

Fig. 6.3 Reversible color change of the di(C12Th2BT)DTCTT film at r.t. and 220 °C

In addition, the flexile packing structure of the DTCTT-based small moelcules may have advantage for solar cell application. Generally, the PCE of solar cell with large cell area (> 1 cm^2) becomes lower than that of small lab-scale cell. This is mainly attributed to the difficulties of controlling the crystallization step, resulting in pin-holes and uneven film. The reversibility of phase transition might enable to control the alignment of molecular orientation in post-deposition step. The liquid crystal-like packing structure is also attractive for the possible crystallization control by applying the electric field. External electric field treatment (EFT) has been developed recently as a viable approach to promote the self-organization of semicrystalline polymer[23]. The columnar structure of the DTCTT derivatives imply strong involvement of molecular dipole moment during the crystallization process as is the case of columnar liquid crystals[24]. It is highly possible that applying electric field during spin-coating process affects the alignment of dipole moment and hence induces the ordered self-assembled structure. Further studies are needed to exploit full potential of this reversible phase transition.

6.3 Outlook

The π–conjugated molecular system has been studied for a long time and attempts have been made to use them for optoelectric applications. Building a functional system from small molecular system is called the bottom-up approach. This approach has been deemed as a promising research direction which could potentially broaden the material design for device applications. In the OPV application, donor and acceptor materials used in the BHJ active layer are required to have a hierarchical organization for an efficient device operation. However, the optimum solid-state structure is difficult to achieve because of lack of a good understanding how to translate a molecular structure to the structure extends from nano- to macroscopic scale encompassing the entire device scale. In this thesis, the attempt has been made to establish a rational molecular designing strategy through validating the incorporation of thienothiohene unit into the core structure of the DTCTT-based small molecules. The designed DTCTT-based donor material showed promising properties for the device application, but the performance in sm-OPV remained moderate. The control of the solid-state morphology and the crystallization behavior was found to be a key for further improvement. In order to elucidate the solid-state structure of the DTCTT-based small molecule, detailed structural analysis was carried out. The results revealed columnar self-assembly and unique reversible phase transition behavior which occurred in a similar manner to liquid crystals. The one-dimensional columnar organization with the slipped-stacked mode of π–π stacking was proven to be beneficial to a good charge transport. Based on above findings, rationally designed molecular structures were proposed. In addition, the liquid crystal-like phase behavior suggested room for further crystal engineering. Overall, findings and outcomes in this thesis provided a qualitative understanding of the structure/property relationship of the novel DTCTT-based small molecules and the designing strategy was validated through detailed characterization and structural analysis. This research

will contribute to a rational designing of efficient π–conjugation system used in organic solar cells. It is believed that further structural modification and crystal engineering could lead to enhanced performance in solar cell devices.

List of Publications:

- Y. Abe, V. Savikhin, J. Yin, C. Soci, A.C. Grimsdale, M. F. Toney, Y.M. Lam: Reversible Crystal-to-Crystal Phase Transition Behavior of Fused Ladder Thienoarenes: Structural Investigation and P-type Transistor Properties, *To be submitted*
- Y. Abe, H. Li, J. Yin, C. Soci, A.C. Grimsdale, Y.M. Lam: Fused Thieno[3,2-b]thiophene-dithiophene Based Donor Material for Molecular Photovoltaics: Structural Comparative Study with Indacenodithiophene, *J. Mat. Chem. C*., 2016, 4, 9656-9663
- T. Salim, S. Sun, Y. Abe, A. Krishna, A.C. Grimsdale, Y.M. Lam: Perovskite-based Solar Cells: Impact of Morphology and Device Architecture on Device Performance, *J. Mat. Chem. A*., 2015, **3**, 8943-8969. Review article
- H. Li, T.M. Koh, Y. Hao, F. Zhou, Y. Abe, H. Su, A. Hagfeldt, A.C. Grimsdale: Comparative Studies on Rigid π Linker-Based Organic Dyes: Structure–Property Relationships and Photovoltaic Performance, *Chem. Sus. Chem.*, 2014, **7**, 3396-3406.

Poster Presentations:

- Y. Abe, J. Yin, C. Soci, A.C. Grimsdale, Y.M. Lam: Reversible Phase Transition Behavior of Fused Dithiophene-thieno[3,2-b]thiophene Based Molecular Donor Material for Photovoltaic Application, Poster Presentation in *International Symposium on Polymer Analysis and Characterization*

(ISPAC 2016), Nanyang Technological Univ., Singapore (Jun 13th, 2016), Student Poster Award

- Y. Abe, H. Li, A.C. Grimsdale, S.G. Mhaisalkar, Y.M. Lam: Low Band-gap Fused Thiophene Molecular Donor for Solution Processed Small Molecular Organic Photovoltaics, Poster Presentation in *MRS fall meeting 2014*, Boston, U.S. (Dec 4th, 2014)
- Y. Abe, H. Li, A.C. Grimsdale, S.G. Mhaisalkar, Y.M. Lam: Thienothiophene Derivatives for the Development of Novel Hole Transporting Material, Poster presentation in *3rd International Workshop on Natural and Artificial Photosynthesis*, Nanyang Technological Univ., Singapore (Jun 11th, 2014)

Reference:

[1] J.E. Coughlin, Z.B. Henson, G.C. Welch, G.C. Bazan, *Accounts of Chemical Research* 47 **(2013)** 257.

[2] Y. Chen, X. Wan, G. Long, *Accounts of Chemical Research* 46 **(2013)** 2645.

[3] Z.B. Henson, K. Mullen, G.C. Bazan, *Nat Chem* 4 **(2012)** 699.

[4] J.A. Love, C.M. Proctor, J. Liu, C.J. Takacs, A. Sharenko, T.S. van der Poll, A.J. Heeger, G.C. Bazan, T.-Q. Nguyen, *Advanced Functional Materials* 23 **(2013)** 5019.

[5] T.S. van der Poll, J.A. Love, T.Q. Nguyen, G.C. Bazan, *Adv Mater* 24 **(2012)** 3646.

[6] J.E. Coughlin, A. Zhugayevych, R.C. Bakus, T.S. van der Poll, G.C. Welch, S.J. Teat, G.C. Bazan, S. Tretiak, *The Journal of Physical Chemistry C* 118 **(2014)** 15610.

[7] C.J. Takacs, Y. Sun, G.C. Welch, L.A. Perez, X. Liu, W. Wen, G.C. Bazan, A.J. Heeger, *J Am Chem Soc* 134 **(2012)** 16597.

[8] A. Sharenko, M. Kuik, M.F. Toney, T.-Q. Nguyen, *Advanced Functional Materials* 24 **(2014)** 3543.

[9] S. Mukherjee, C.M. Proctor, J.R. Tumbleston, G.C. Bazan, T.Q. Nguyen, H. Ade, *Adv Mater* 27 **(2015)** 1105.

[10] M. Abdelsamie, N.D. Treat, K. Zhao, C. McDowell, M.A. Burgers, R. Li, D.M. Smilgies, N. Stingelin, G.C. Bazan, A. Amassian, *Adv Mater* 27 **(2015)** 7285.

[11] J.A. Love, I. Nagao, Y. Huang, M. Kuik, V. Gupta, C.J. Takacs, J.E. Coughlin, L. Qi, T.S. van der Poll, E.J. Kramer, A.J. Heeger, T.Q. Nguyen, G.C. Bazan, *J Am Chem Soc* 136 **(2014)** 3597.

[12] K. Ohya, *Jpn. Kokai Tokkyo Koho* **(2015)** JP 2015054823.

[13] J.-L. Wang, Q.-R. Yin, J.-S. Miao, Z. Wu, Z.-F. Chang, Y. Cao, R.-B. Zhang, J.-Y. Wang, H.-B. Wu, Y. Cao, *Advanced Functional Materials* 25 **(2015)** 3514.

[14] X. Liu, Q. Li, Y. Li, X. Gong, S.-J. Su, Y. Cao, *Journal of Materials Chemistry A* 2 **(2014)** 4004.

[15] J. Wolf, M. Babics, K. Wang, Q. Saleem, R.-Z. Liang, M.R. Hansen, P.M. Beaujuge, *Chemistry of Materials* 28 **(2016)** 2058.

[16] R.L. Uy, S.C. Price, W. You, *Macromolecular Rapid Communications* 33 **(2012)** 1162.

[17] E. Lee, B. Hammer, J.-K. Kim, Z. Page, T. Emrick, R.C. Hayward, *J Am Chem Soc* 133 **(2011)** 10390.

[18] F.J.M. Hoeben, P. Jonkheijm, E.W. Meijer, A.P.H.J. Schenning, *Chem Rev* 105 **(2005)** 1491.

[19] M. Wang, F. Wudl, *Journal of Materials Chemistry* 22 **(2012)** 24297.

[20] J. Harada, T. Shimojo, H. Oyamaguchi, H. Hasegawa, Y. Takahashi, K. Satomi, Y. Suzuki, J. Kawamata, T. Inabe, *Nat Chem* advance online publication **(2016)**.

[21] J. Luo, A.H. Jensen, N.R. Brooks, J. Sniekers, M. Knipper, D. Aili, Q. Li, B. Vanroy, M. Wubbenhorst, F. Yan, L. Van Meervelt, Z. Shao, J.

Fang, Z.-H. Luo, D.E. De Vos, K. Binnemans, J. Fransaer, *Energy & Environmental Science* 8 **(2015)** 1276.

[22] P.-J. Alarco, Y. Abu-Lebdeh, A. Abouimrane, M. Armand, *Nat Mater* 3 **(2004)** 476.

[23] A. Solanki, A. Bagui, G. Long, B. Wu, T. Salim, Y. Chen, Y.M. Lam, T.C. Sum, *ACS Appl Mater Interfaces* 8 **(2016)** 32282.

[24] T. Osawa, T. Kajitani, D. Hashizume, H. Ohsumi, S. Sasaki, M. Takata, Y. Koizumi, A. Saeki, S. Seki, T. Fukushima, T. Aida, *Angew Chem Int Ed Engl* 51 **(2012)** 7990.

APPENDIX A

Synthetic procedure

4-Bromo-7-(5'-hexyl-[2,2'-bithiophen]-5-yl)benzo[c][2,1,3]thiadiazole, Compound 1

To a 100 ml three neck flask was added 4,7-dibromo-2,1,3-benzothiadiazole (1.5 g, 5.1 mmol), 5-tributylstannyl-5'-hexyl-2,2'-bithiophene (2.3 g, 4.3 mmol) and degassed Toluene 20 ml, followed by adding $Pd(PPh_3)_4$ (450 mg, 0.39 mmol), and purged with nitrogen gas. The reaction was refluxed for overnight. The cooled mixture was poured into water and extracted with DCM. The organic layer was collected, dried over anhydrous $MgSO_4$. The filtrate was evaporated and the residue was purified by flash column chromatography on silica gel using Hexane:Chloroform = 4:1 (v/v) as eluent to yield compound 1as red solid (990 mg, 50%).

^{1}H NMR (400 MHz, CDCl3): δ 8.15 (d, *J*=4 Hz, 1H), 7.843 (d, *J*=7.5 Hz, 1H), 7.685 (d, *J*=7.5 Hz, 1H), 7.180 (d, *J*=4 Hz, 1H), 7.107 (d, *J*=4 Hz, 1H), 6.726 (d, *J*=4 Hz, 1H), 2.817 (t, 2H), 1.702 (m, 2H), 1.5-1.2 (m, 6H), 1.0-0.8 (m, 3H); MS (MALDI-TOF) m/z: 461 (M+); calcd 462.0

4-Boronic acid pinacol ester-7-(5'-hexyl-[2, 2'-bithiophen]-5-yl)benzo[c][2,1,3]thiadiazole, Compound 2

To a 50 ml two neck flask was added compound 1(880 mg, 1.9 mmol), B_2pin_2 (1.45 g, 5.7 mmol), KOAc (560 mg, 5.8 mmol) and thoroughly degassed Toluene 15 ml, followed by adding $Pd(dppf)Cl_2$ (78 mg, 0.1 mmol), and purged with nitrogen gas. The reaction was heated up to 80 °C and stirred for 9 hrs. The cooled mixture was poured into water and extracted with DCM. The organic layer was dried over anhydrous MgSO4, filtrate, and dried by rotary evaporator. The crude product was purified by short column chromatography on silica gel using Hexane:THF =2:1 (v/v) as eluent to yield slight crude compound as red viscous oil (440 mg, 45 %). The product was used

immediately to following reaction as was found to be unstable.

di(HTh2BT)IDT

diBr-IDT (135 mg, 0.11 mmol), compound 2 (170 mg, 0.33 mmol), $Pd(PPh_3)_4$ (20 mg, 0.017 mmol) were added to round-bottom flask purged with nitrogen gas, followed by THF (freeze pump thaw x3) 20 ml. The reaction was started by injecting K_2CO_3 aq (2M, 1 ml) and heating to 80 °C for reflux. The reaction was completed in 2 hrs and quenched by adding water, followed by extraction with DCM. The organic layer was dried by anhydrous $MgSO_4$, filtrate, and dried by rotary evaporator. The crude product was purified by column chromatography on silica gel using Hexane:chloroform =4:1 (v/v) as eluent (twice), followed by recrystallization with (Acetone/chloroform) to yield dark purple powder (110 mg, 52 %).

^{1}H NMR (400 MHz, CDCl3): δ 8.07 (s, 2H), 8.02 (d, 2H, *J* =4Hz), 7.80 (m, 4H), 7.54 (s, 2H), 7.28–7.26 (m, 8H), 7.18 (d, 2H, *J* =4Hz), 7.12–7.09 (m, 10H), 6.72 (d, 2H, *J* =4Hz), 2.82 (t, 4H, *J* =7.6Hz), 2.58 (t, 8H, *J* =8.0 Hz), 1.73–1.55 (m, 8H), 1.40–1.28 (m, 40H), 0.90–0.84 (m, 18H); ^{13}C NMR (100 MHz, CDCl3): δ 156.8, 153.8, 152.5, 152.4, 146.1, 143.3, 142.1, 141.8, 141.6, 139.3, 137.5, 135.5, 134.6, 128.4, 128.2, 128.0, 126.3, 125.3, 125.1, 125.0, 124.7, 123.8, 123.8, 123.2, 117.7, 63.2, 35.6, 31.7, 31.6, 31.3, 30.2, 29.2, 28.8, 22.6, 14.1; MS (MALDI-TOF) m/z: 1671 (M+); calcd 1670.6; Elemental analysis calcd (%) for C104H110N4S8: C, 74.68; H, 6.63; N, 3.35; found: C, 74.87; H, 6.49; N, 3.33

Precursor 3

To a 250 ml 3 neck flask was added 2,5-Bis(trimethylstannyl)thieno[3,2-b]thiophene (2.51 g, 5.4 mmol), 2-Bromo-3-thiophene carboxylic acid ethyl ester (2.67 g, 11.4 mmol) and degassed Toluene 20 ml, followed by adding $Pd(PPh_3)_4$ (600 mg, 0.52 mmol), and purged with nitrogen gas. The reaction was refluxed for overnight. After the reaction, the solvent was removed by

rotary evaporator and the residue was purified by flash column chromatography on silica gel using Hexane:DCM = 1:2 (v/v) as eluent. The compound was further purified by recrystallization from hot THF to yield compound as red powder (1.65 g, 68 %).

^{1}H NMR (400 MHz, CDCl3): δ 7.67 (s, 2H), 7.51 (d, 2H, *J* =5.2 Hz),7.23 (d, 2H, *J* =5.2 Hz), 4.31 (q, 4H, J =7.2 Hz), 1.33 (t, 6H, *J* =7.2) MS (MALDI-TOF) m/z: 447 (M+); calcd: 448.0

Precursor 4

The 100 ml round-flask was equipped with activated magnesium turning (1.08 g, 44.4 mmol), a small portion of iodine and anhydrous THF 5ml under nitrogen atmosphere in ice bath. 4-n-octyl-bromobenzene (7.0 ml, 32.5 mmol) dissolved in THF 25 ml was dropwised into the system so that inside temperature should not exceed 40 °C and stirred for 1 hr. To a precursor 3 (1.67 g, 3.7 mmol) in a round-flask under nitrogen atmosphere was added the prepared Grignard reagent at room temperature. The resulting mixture was heated up to reflux for 2 hrs. After cooling down to room temprature, the reaction mixture was quenched by HCl aq. and was extracted DCM/0.1 M HClaq, and washed with brine. The combined organic layer was dried in anhydrous $MgSO_4$, filtrated, and dried by rotary evaporator. The residue was purified by short column chromatography on silica gel using Hexane:DCM = 1:2 as eluent to yield a compound as orange powder (3.3 g, 79%)

^{1}H NMR (400 MHz, CDCl3): δ 7.15-7.08 (m, 20H), 6.63 (s, 2H), 6.44 (d, 2H, *J* =5.2 Hz), 2.59 (t, 8H, *J* =8.0 Hz), 1.61-1.59 (m, 8H), 1.30–1.26 (m, 40H), 0.87 (t, 12H, J =6.4 Hz); MS (MALDI-TOF) m/z: 1099 (M-OH); calcd 1116.6

dibromo-DTCTT, Precursor 5

Precursor 4 (3.3 g, 2.95 mmol), Amberlyst 1.4 g and degassed Toluene 200 ml were added to a round-bottom flask and purged with nitrogen gas. The reaction was refluxed for 3 hrs. After filtration, the solvent was removed by rotary

evaporator and the residue was purified by short column chromatography on silica gel using Hexane:DCM = 10:1 (v/v) to yield cyclized compound as yellow oil (2.47 g) and was immediately used to following reaction as was found to be unstable.

The cyclized compound (2.47 g) and degassed chloroform 100 ml was added to a round-bottom flask, purged with nitrogen gas, and placed in ice bath. N-bromosuccimide (850 mg, 4.8 mmol) was slowly added into the system. After 1 hr of reaction time, the reaction was quenched by NaOH aq, followed by extraction with DCM/0.1 M NaOH aq., washed with brine. The combined organic layer was dried with anhydrous $MgSO_4$, filtrated, and dried by rotary evaporator. The crude oil was purified by recrystallization (Acetone/DCM) to yield bright yellow powder (1.22 g, 33 % in 2 steps).

^{1}H NMR (400 MHz, CDCl3): δ 7.12-7.04 (m, 18H), 2.55 (t, 8H), 1.6-1.1 (m, 44H), 0.867 (t, 12H); Elemental analysis calcd (%) for C72H86S4Br2: C, 69.77; H, 6.99; S, 10.35; found: C, 70.16; H, 6.58; S, 10.16

di(HTh2BT)DTCTT

This compound was synthesized with the same method of di(HTh2BT)IDT from precursor 5 (150 mg, 0.12 mmol) to yield as dark green powder (110 mg, 50 %).

^{1}H NMR (400 MHz, CDCl3): δ 8.14 (s, 2H), 8.02 (d, 2H, J = 4 Hz), 7.79 (s, 4H), 7.25 (m, 8H), 7.18 (d, 2H J = 4 Hz), 7.13-7.10 (m, 10H), 6.72 (d, 2H, J = 4 Hz), 2.82 (t, 4H, J = 7.6 Hz), 2.56 (t, 8H, J = 7.6 Hz), 1.73-1.50 (m, 12H), 1.40-1.24 (m, 52H), 0.92-0.86 (m, 18H); ^{13}C NMR (100 MHz, CDCl3): δ 158.2, 152.5, 152.2, 149.3, 146.0, 142.0, 140.3, 139.5, 139.3, 139.2, 137.7, 137.6, 136.0, 134.7, 128.6, 128.1, 127.9, 126.2, 125.1, 125.0, 124.9, 124.1, 123.8, 123.7, 123.4, 62.4, 35.6, 31.9, 31.6, 31.3, 30.3, 29.5, 29.4, 29.2, 28.8, 22.6, 22.6, 14.1; MS (MALDI-TOF) m/z: 1844 (M+); calcd 1844.7; Elemental analysis calcd (%) for C112H124N4S10: C, 72.84; H, 6.77; N, 3.03; S, 17.36; found: C, 73.21; H, 6.50; N, 2.95

4-Bromo-7-(2-hexylthiophene-5-yl)-benzo[c][2,1,3]thiadiazole, Compound 1 (R=R_1)

To a 100 ml 3 neck flask was added 4,7-dibromo-2,1,3-benzothiadiazole (1.29 g, 4.4 mmol), 2-tributylstannyl-5-hexylthiophene (1.8 g, 3.9 mmol) and degassed Toluene 20 ml, followed by adding Pd(PPh3)4 (300 mg, 0.26 mmol), and purged with nitrogen gas. The reaction was refluxed for overnight. The cooled mixture was poured into water and extracted with DCM. The organic layer was collected, dried over anhydrous MgSO4. The filtrate was evaporated and the residue was purified by flash column chromatography on silica gel using Hexane:Chloroform = 4:1 (v/v) as eluent to yield compound 1as orange solid (0.74 g, 49%).

^{1}H NMR (400 MHz, $CDCl_3$): δ 7.92 (d, *J*=4 Hz, 1H), 7.82 (d, *J*=7.5 Hz, 1H), 7.6 (d, *J*=7.5 Hz, 1H), 6.87 (d, *J*=4 Hz, 1H), 2.87 (t, 2H), 1.75 (m, 2H), 1.5-1.2 (m, 6H), 0.91 (t, 3H); MS (MALDI-TOF) m/z: 380 (M+); calcd 380.0

4-Bromo-7-(5'-dodecyl-(2,2'-bithiophen)-5-yl)-benzo[c][2,1,3]thiadiazole, Compound 1 (R=R_3)

This compound was synthesized with the same procedure of compound1 (R=R_1). The reaction started from 4,7-dibromo-2,1,3-benzothiadiazole (760 mg, 2.6 mmol) and 5-tributylstannyl-5'-dodecyl-2,2'-bithiophene (1.36 g, 2.2 mmol) to get product as red solid (490 mg, 41%).

^{1}H NMR (400 MHz, $CDCl_3$): δ 8.01 (d, *J*=4 Hz, 1H), 7.84 (d, *J*=8.0 Hz, 1H), 7.68 (d, *J*=8.0 Hz, 1H), 7.18 (d, *J*=4 Hz, 1H), 7.11 (d, *J*=4 Hz, 1H), 6.72 (d, *J*=4 Hz, 1H), 2.81 (t, *J*=7.6 Hz, 2H), 1.70 (m, 2H), 1.4-1.3 (m, 18H), 0.88 (t, *J*=6.8 Hz, 3H); MS (MALDI-TOF) m/z: 546 (M+); calcd 546.1

4-Boronic acid pinacol ester-7-(2-hexylthiophene-5-yl)benzo[c][2,1,3]thiadiazole, Compound 2 (R=R_1)

To a 50 ml 2 neck flask was added compound 1 (R=R_1)(580 mg, 1.52 mmol), B2pin2 (1.2 g, 4.7 mmol), KOAc (440 mg, 4.49 mmol) and thoroughly degassed Toluene 25 ml, followed by adding Pd(dppf)Cl2 (62 mg, 0.08 mmol), and purged with nitrogen gas. The reaction was heated up to 80 °C and stirred for 9 hrs. The cooled mixture was poured into water and extracted with DCM. The organic layer was dried over anhydrous MgSO4, filtrate, and dried by rotary evaporator. The crude product was purified by short column chromatography on silica gel using Hexane:THF =2:1 (v/v) as eluent to yield slight crude compound as orange solid (320 mg, 49 %). The product was used immediately to following reaction as was found to be unstable.

4-Boronic acid pinacol ester-7-(5'-dodecyl-[2, 2'-bithiophen]-5-yl)benzo[c][2,1,3]thiadiazole, Compound 2 (R=R_3)

This compound was synthesized with the same procedure of compound2 (R=R_1). The reaction started from compound 1 (R=R_3) (430 mg, 0.78 mmol) to get crude product as red viscous oil (230 mg).

di(HTh1BT)IDT

diBr-IDT (120 mg, 0.11 mmol), compound 2 (R=R_1) (120 mg, 0.28 mmol), Pd(PPh3)4 (19 mg, 0.016 mmol) were added to round-bottom flask purged with nitrogen gas, followed by THF (freeze pump thaw x3) 25 ml. The reaction was started by injecting K2CO3 aq (1M, 1 ml) and heating to 80 °C for reflux. The reaction was completed in 2 hrs and quenched by adding water, followed by extraction with DCM. The organic layer was dried by anhydrous MgSO4, filtrate, and dried by rotary evaporator. The crude product was purified by column chromatography on silica gel using Hexane:chloroform =4:1 (v/v) as eluent (twice), followed by recrystallization with (Acetone/chloroform) to yield dark purple powder (95 mg, 56 %).

^{1}H NMR (400 MHz, $CDCl_3$): δ 8.03 (s, 2H), 7.93 (d, 2H, *J* =4Hz), 7.81 (d, 2H, *J* =8 Hz), 7.74 (d, 2H, *J* =8 Hz) 7.53 (s, 2H), 7.27 (d, 8H, *J* =10 Hz), 7.10 (d, 8H, *J* =10 Hz), 6.87 (d, 2H, *J* =4Hz), 2.88 (t, 4H, *J* =7.6Hz), 2.57 (t, 8H, *J* =7.2 Hz), 1.78–1.71 (m, 4H), 1.59–1.28 (m, 44H), 0.90–0.84 (m, 18H); ^{13}C NMR (100 MHz, $CDCl_3$): δ 156.7, 153.7, 152.6, 152.4, 148.0, 143.1, 142.2, 141.9, 141.6, 136.9, 135.5, 128.4, 128.0, 127.5, 126.0, 125.9, 125.3, 125.0, 124.8, 123.0, 117.7, 63.2, 35.6, 31.7, 31.6, 31.4, 30.3, 29.2, 28.9, 22.6, 14.1; MS (MALDI-TOF) m/z: 1506 (M+); calcd 1506.7; Elemental analysis calcd (%) for $C_{96}H_{106}N_4S_6$: C, 76.45; H, 7.08; N, 3.71; found: C, 76.26; H, 6.89; N, 3.53

di(HTh1BT)DTCTT

This compound was synthesized with the same method of di(HTh1BT)IDT. The reaction started from diBr-DTCTT (150 mg, 0.12 mmol) and compound 2 (R=R_1) (130 mg, 0.3 mmol) to yield as dark green powder (104 mg, 51 %). ^{1}H NMR (400 MHz, $CDCl_3$): δ 8.09 (s, 2H), 7.92 (d, 2H, *J*=3.2 Hz), 7.70 (s, 4H), 7.23 (d, 8H, *J*=8.0 Hz), 7.07 (d, 8H, *J*=8.0 Hz), 6.87 (d, 2H, *J*=3.2 Hz), 2.88 (t, 4H, *J*=7.6 Hz), 2.54 (t, 8H, *J*=7.6 Hz), 1.77-1.71 (m, 4H), 1.56-1.24 (m, 60H), 0.92-0.82 (m, 18H); ^{13}C NMR (100 MHz, $CDCl_3$): δ 158.1, 152.6, 152.3, 149.2, 147.9, 141.9, 140.4, 139.6, 139.0, 137.7, 136.9, 135.9, 128.6, 127.9, 127.7, 127.4, 125.9, 125.5, 125.3, 125.1, 124.3, 123.2, 62.4, 35.6, 31.9, 31.6, 31.6, 31.3, 30.3, 29.7, 29.5, 29.5, 29.4, 29.3, 29.2, 28.9, 22.7, 22.6, 14.1 ; MS (MALDI-TOF) m/z: 1681 (M+); calcd 1680.7; Elemental analysis calcd (%) for $C_{104}H_{120}N_4S_8$: C, 74.24; H, 7.19; N, 3.33; found: C, 74.39; H, 6.79; N, 3.23

di(C12Th2BT)DTCTT

This compound was synthesized with the same method of di(HTh1BT)IDT. The reaction started from diBr-DTCTT (150 mg, 0.12 mmol) and compound 2 (R=R_3) (230 mg) to yield as dark green powder (106 mg, 43 %). ^{1}H NMR (400 MHz, $CDCl_3$): δ 8.12 (s, 2H), 8.05 (d, 2H, *J*=3.2 Hz), 7.76 (m, 4H), 7.24 (d, 8H, *J*=8.0 Hz), 7.18 (d, 2H, *J*=4.0 Hz), 7.09 (m, 10H), 6.72 (d, 2H, *J*=3.2 Hz), 2.81 (t, 4H, *J*=7.6 Hz), 2.55 (t, 8H, *J*=7.6 Hz), 1.72-1.68 (m, 4H), 1.61-1.52 (m, 8H), 1.45-1.2 (m, 76H), 0.9-0.8 (m, 18H); ^{13}C NMR (100 MHz, $CDCl_3$): δ 158.2, 152.5, 152.3, 149.3, 146.0, 142.0, 140.3, 139.5, 139.3, 139.2, 137.7, 137.6, 135.9, 134.7, 128.6, 128.1, 127.9, 126.2, 125.1, 125.0, 124.9, 124.1, 123.8, 123.7, 123.4, 62.4, 35.6, 31.9, 31.9, 31.6, 31.3, 30.2, 29.7, 29.6, 29.6, 29.5, 29.4, 29.4, 29.2, 29.1, 22.7, 22.6, 14.1 ; MS (MALDI-TOF) m/z: 2013 (M+); calcd 2012.9; Elemental analysis calcd (%) for C124H148N4S10: C, 73.91; H, 7.40; N, 2.78; found: C, 73.95; H, 7.24; N, 2.76

^{1}H-NMR, ^{13}C-NMR, and MS data

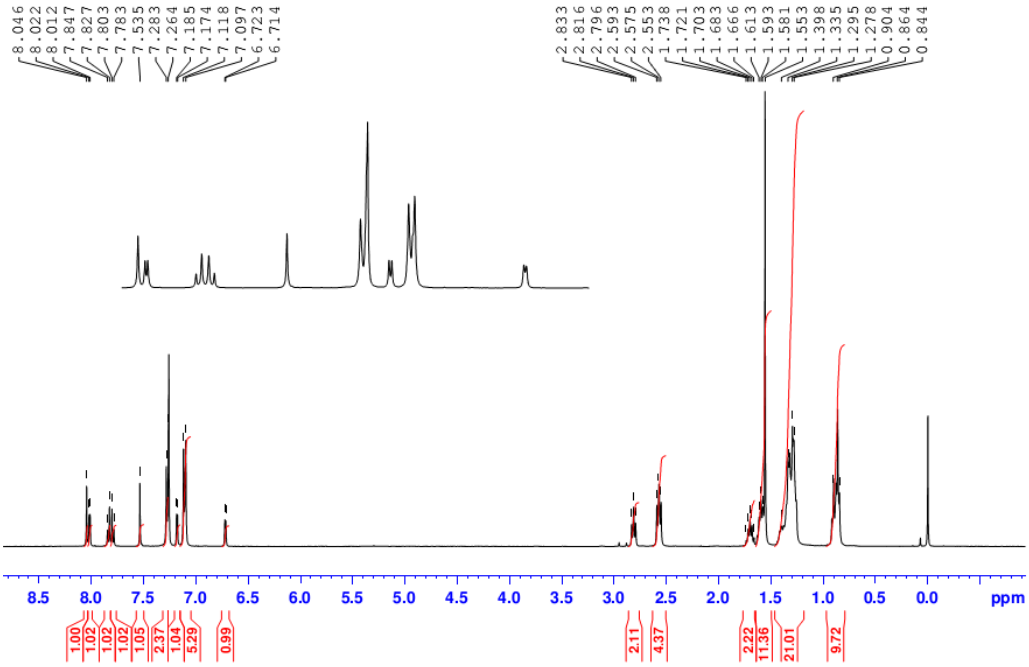

Fig. S1 ^{1}H-NMR of di(HTh2BT)IDT

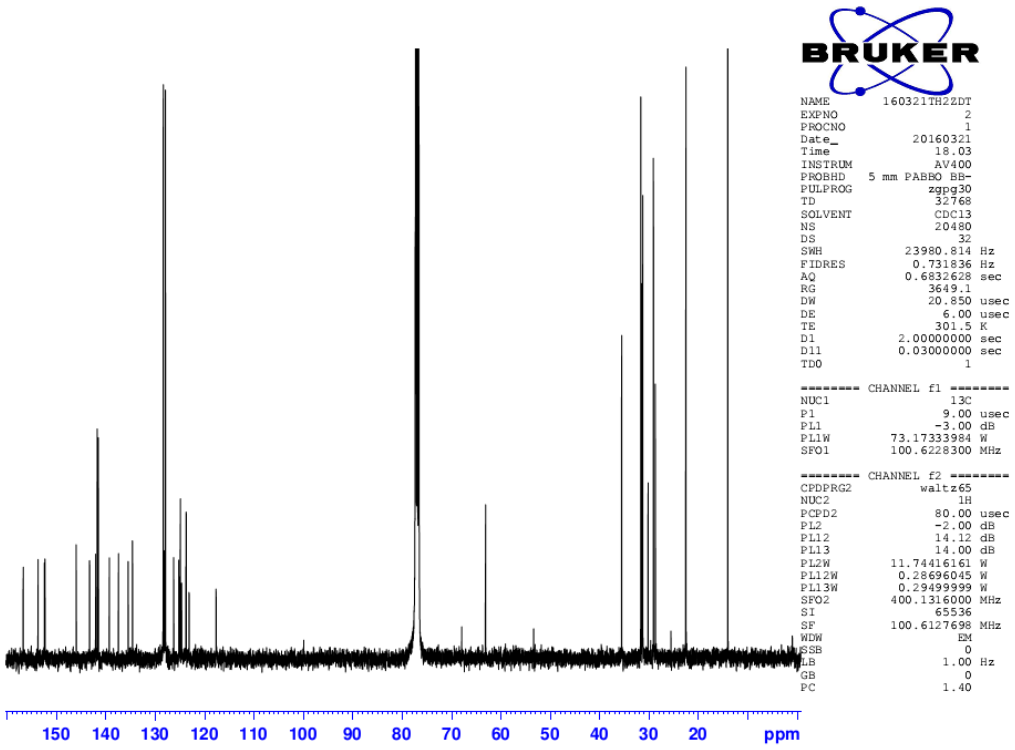

Fig. S2 ^{13}C-NMR of di(HTh2BT)IDT

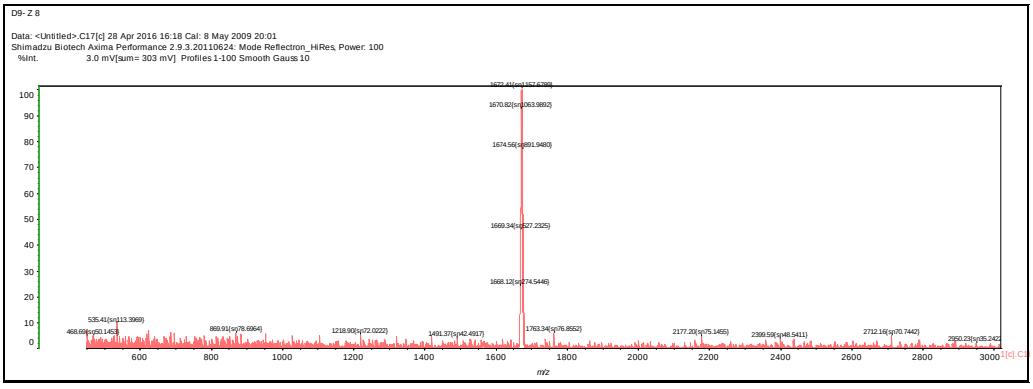

Fig. S3 MALDI-TOF MS of di(HTh2BT)IDT

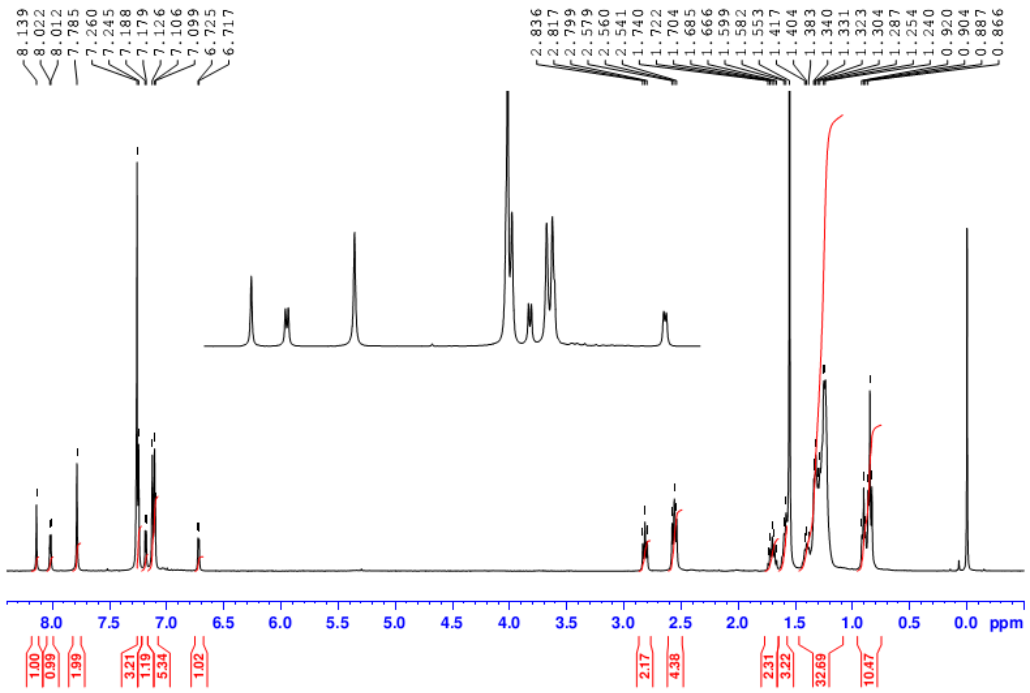

Fig. S4 ^{1}H-NMR of di(HTh2BT)DTCTT

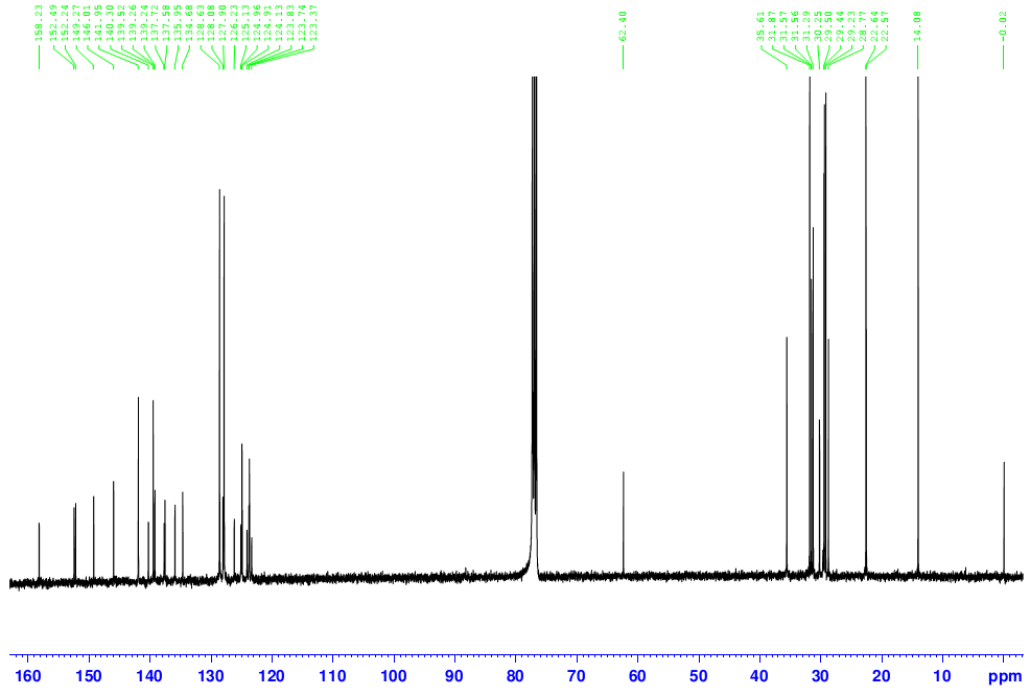

Fig. S5 ^{13}C-NMR of di(HTh2BT)DTCTT

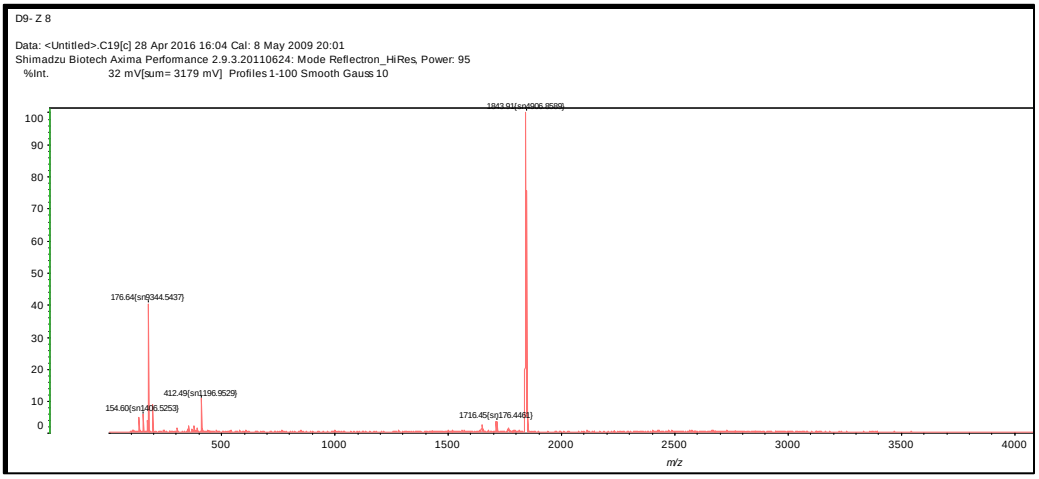

Fig. S6 MALDI-TOF MS of di(HTh2BT)DTCTT

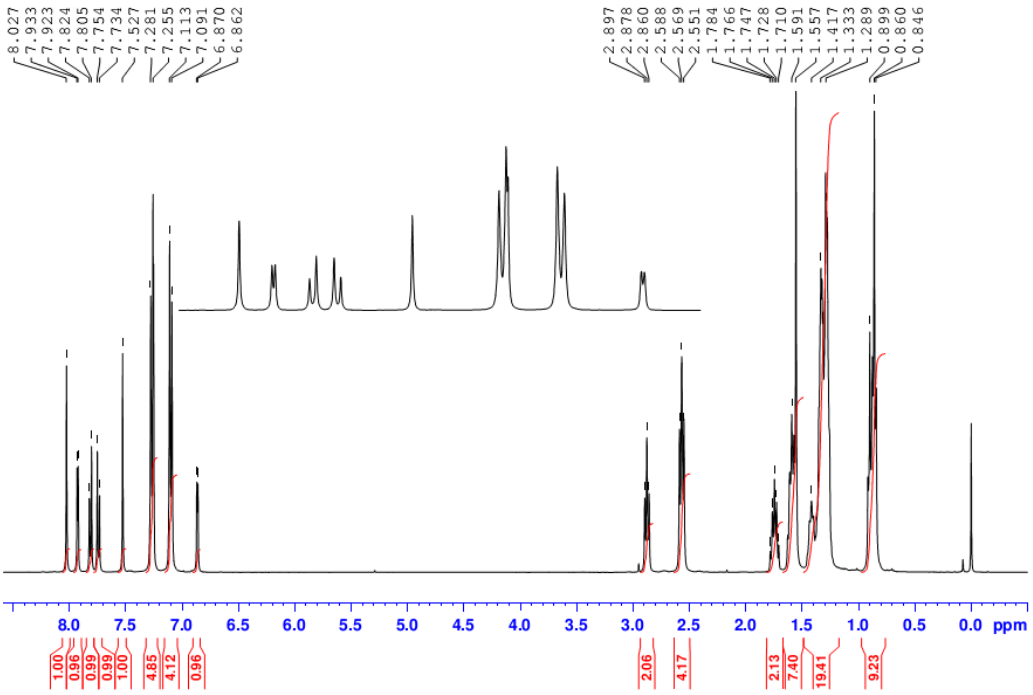

Fig. S7 ^{1}H-NMR of di(HTh1BT)IDT

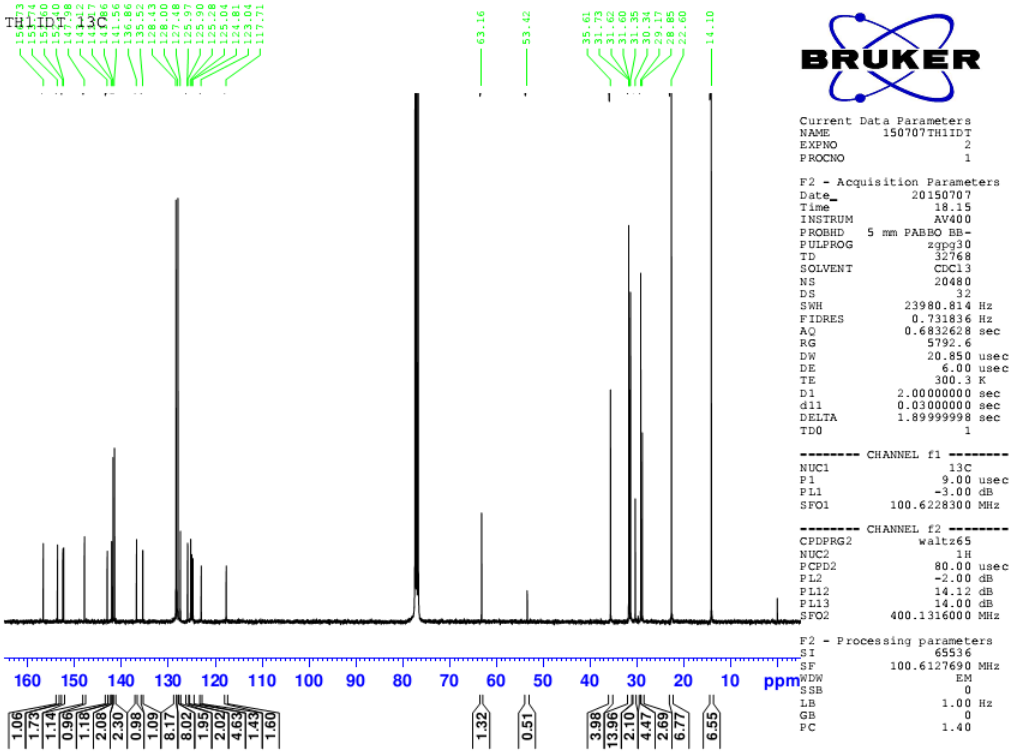

Fig. S8 ^{13}C-NMR of di(HTh1BT)IDT

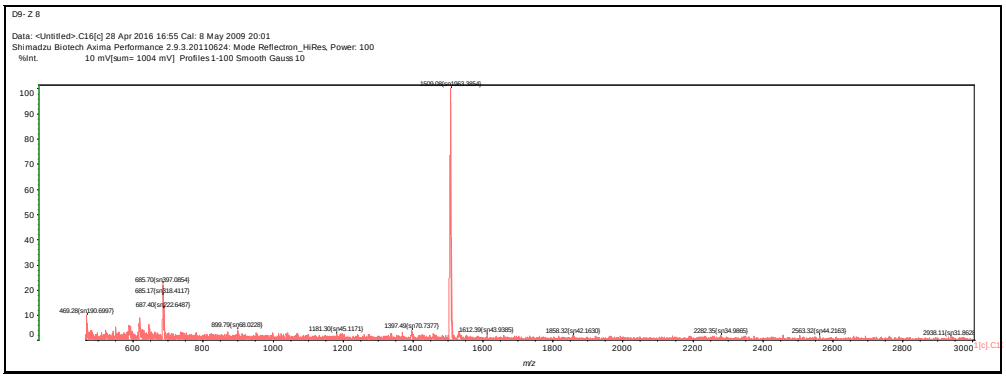

Fig. S9 MALDI-TOF MS of di(HTh1BT)IDT

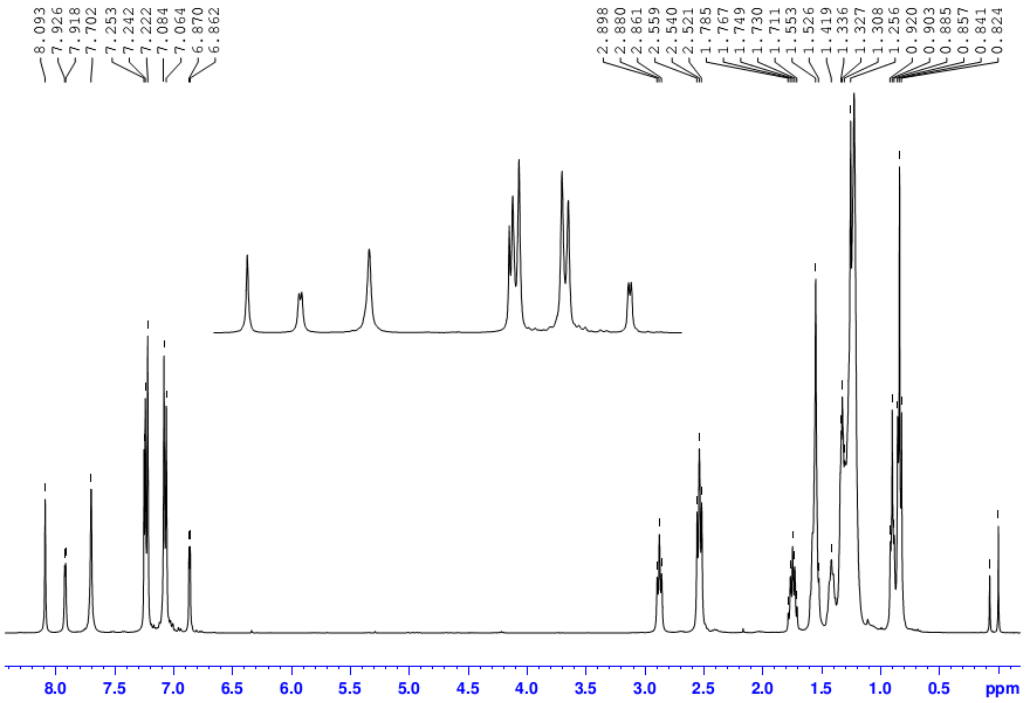

Fig. S10 ^{1}H-NMR of di(HTh1BT)DTCTT

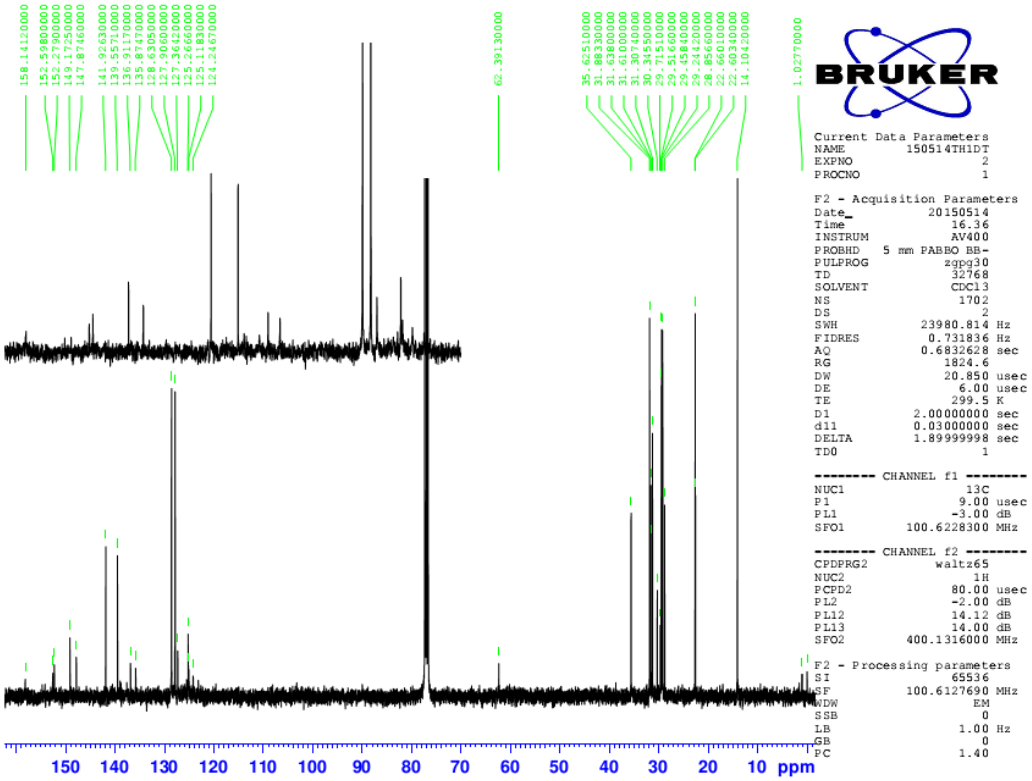

Fig. S11 ^{13}C-NMR of di(HTh1BT)DTCTT

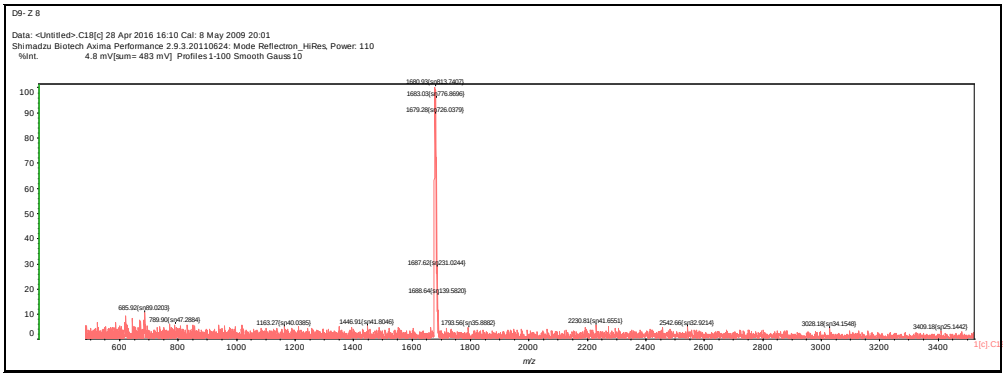

Fig. S12 MALDI-TOF MS of di(HTh1BT)DTCTT

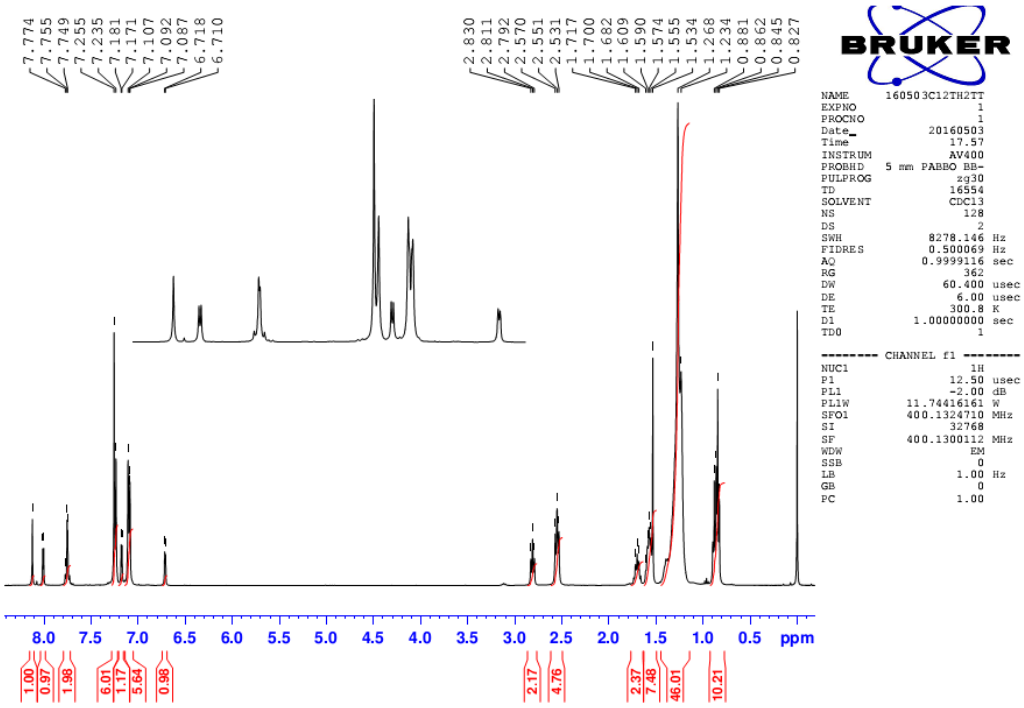

Fig. S13 ^{1}H-NMR of di(C12Th2BT)DTCTT

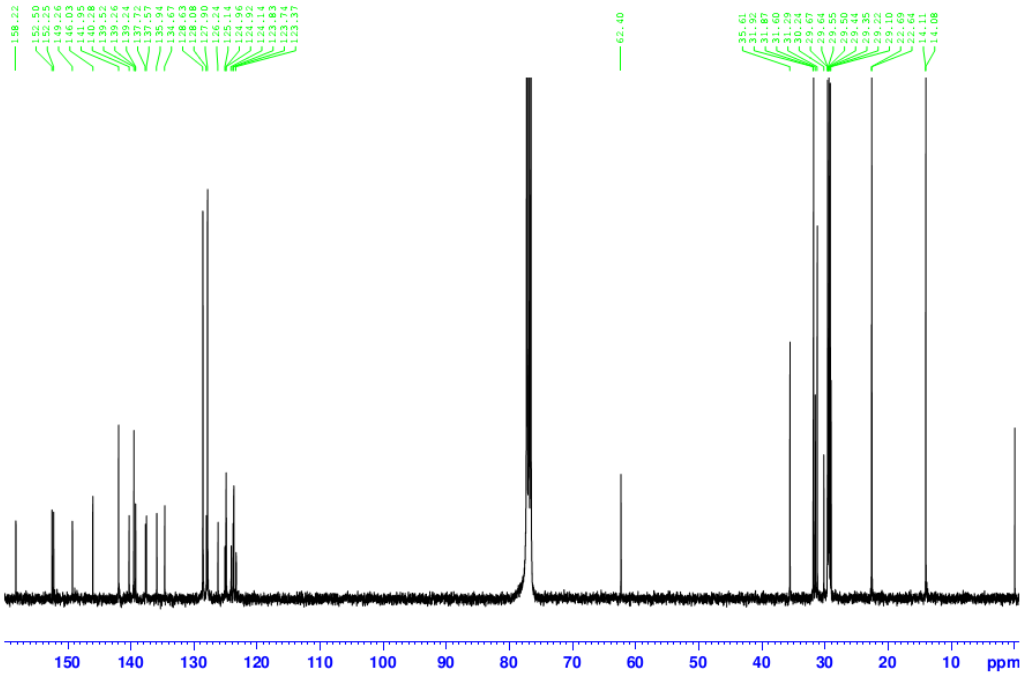

Fig. S14 ^{1}H-NMR of di(C12Th2BT)DTCTT

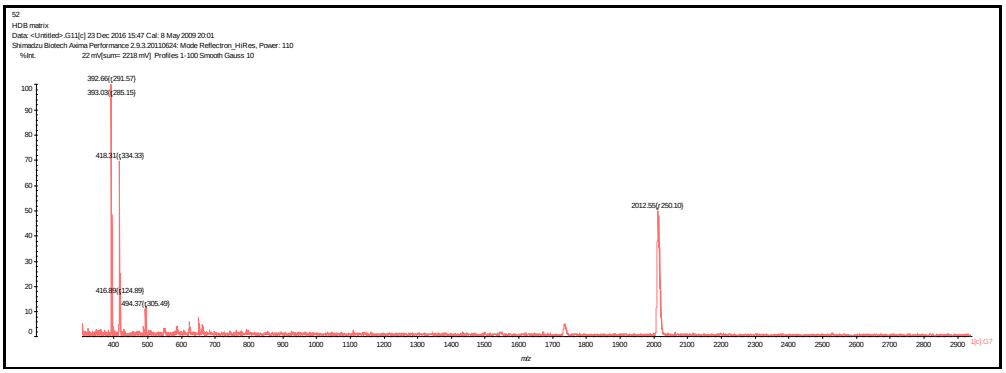

Fig. S15 MALDI-TOF MS of di(C12Th2BT)DTCTT

Appendix B

X-ray crystallography report of di(HTh1BT)IDT

A black plate-like single crystal of C96H106N4S6, approximate dimensions (0.158 x 0.375 x 0.589) mm^3, was selected for the X-ray crystallographic analysis, and mounted at low temperature (T = 100 K) on a cryoloop. Using a Perfluoropolyether Cryo Oil based cryoprotectant. A 4 circles goniometer Kappa geometry Bruker AXS D8 Venture, equipped with a Photon 100 CMOS active pixel sensor detector with a Copper monochromatized (λ = 1.54178 Å) X-Ray radiation was used to carried out the measurement. Frames were integrated with the Bruker SAINT software[1] using a narrow-frame algorithm. The integration of the data using a monoclinic unit cell yielded a total of 33878 reflections to a maximum θ angle of 64.53° (0.85 Å resolution), of which 18387 were independent (average redundancy 1.842, completeness = 87.8%, Rint = 5.80%, Rsig = 8.63%) and 13666 (74.32%) were greater than 2σ (F2). Final cell constants of a = 23.7507(8) Å, b = 27.8509(17) Å, c = 38.1895(17) Å, β = 100.163(2)°, volume = 24865.(2) Å3, are based upon the refinement of the XYZ-centroids of 3499 reflections above 20 σ(I) with 5.750° < 2θ < 128.3°. Data were corrected for absorption effects using the multi-scan method implemented on the program (SADABS)[2]. The calculated minimum and maximum transmission coefficients (based on crystal size) are 0.401 and 0.753. The model was solved in the centrosymmetric space group *C 2/c* with the aid of the software SHELXT[3] , using a Dual Space method to solve the phase problem expanded in a triclinic unit cell P1. Starting with random atoms, phases calculation are initiated in the reciprocal space, then more atomics positions are localized in the real space and used to calculate additional phases. In the course of the calculation process different strategies are used in the reciprocal space to improve phases and localize more atoms. Solutions with the best figure of merit are chosen and an electronic density map is directly computed. Then the structure is assembled to maximize its connectivity and centered in the unit cell.

Asymmetric unit was built up with three and half molecules respectively labelled: A, B and C. Refinement of the structure was carried out by least squares procedures on weighted F2 values using the SHELXL-version 2014/6[4] included in the WinGx programs for Windows[5]. Hydrogen atoms were localized on difference Fourier maps but then introduced in the refinement as fixed contributors in idealized geometry with an isotropic thermal parameters fixed at 20 % higher than those carbons atoms they were connected. All disordered parts of the model were anisotropically refined with a ratio of occupancy equal to: 50%. Interatomic lengths and angles were restrained in order to get a chemically correct model. Constraints were applied on ADP's parameters for carbon atoms. At the last cycles of refinement the program Squeeze[6] under the Crystallographic tools Platon[7] was used in order to modelize some broad and undefined electronic density peaks remaining on the difference Fourier maps. The final anisotropic full-matrix least-squares refinement on F2 with 1601 variables converged at R1 = 16.78%, for the observed data and wR2 = 47.42% for all data. The goodness-of-fit was 2.080. The largest peak in the final difference electron density synthesis was 1.859 e-/Å3 and the largest hole was -1.155 e-/Å^3 with an RMS deviation of 0.169 e-/Å3. On the basis of the final model, the calculated density was 1.212 g/cm3 and F(000), 9652 e-.

Platon Squeeze details:
PLATON: Total Potential Solvent Accessible Void Vol: 246.1 Å^3 per unit cell volume : 24767.6 Å^3 [1.0%]

SQUEEZE produces and analyzes a phase enhanced difference map using the files name.res & name.hkl. Density found in solvent accessible voids is back-fourier transformed into A(solv) & B(solv) contributions to F(calc) to be used for subsequent L.S. refinement. No model refinement is done by PLATON/SQUEEZE

Table S1 Summary of crystallographic data of di(HTh1BT)IDT

Chemical formula	$C_{144}H_{157.5}N_6S_9$
Formula weight	2260.79 g/mol
Temperature	100(2) K
Wavelength	1.54178 Å
Crystal size	(0.158 x 0.375 x 0.589) mm^3
Crystal system	monoclinic
Space group	C 1 2/c 1
Unit cell dimensions	a = 23.7318(10) Å b = 27.7793(13) Å α = 90° c = 38.1560(17) Å β = 100.061(2)°
Volume	24767.6(19) $Å^3$ γ = 90°
Z	8
Density (calculated)	1.213 g/cm^3
Absorption coefficient	1.900 mm^{-1}
F(000)	9660
Theta range for data collection	2.35 to 64.62°
Index ranges	-27<=h<=27, -28<=k<=32, -44<=l<=43
Reflections collected	58808
Independent reflections	18590 [R(int) = 0.0624]
Coverage of independent reflections	89.0%
Absorption correction	multi-scan
Max. and min. transmission	0.7530 and 0.4010
Function minimized	$\Sigma w(F_o^2 - F_c^2)^2$
Data / restraints / parameters	18590 / 1848 / 1601
Goodness-of-fit on F^2	2.079
Final R indices	14448 data; I>2σ(I) R1 = 0.1678, wR2 = 0.4527 all data R1 = 0.1858, wR2 = 0.4741
Weighting scheme	$w=1/[\sigma^2(F_o^2)+(0.2000P)^2]$ where $P=(F_o^2+2F_c^2)/3$
Extinction coefficient	0.0001(0)
Largest diff. peak and hole	1.861 and -1.124 $eÅ^{-3}$
R.M.S. deviation from mean	0.169 $eÅ^{-3}$

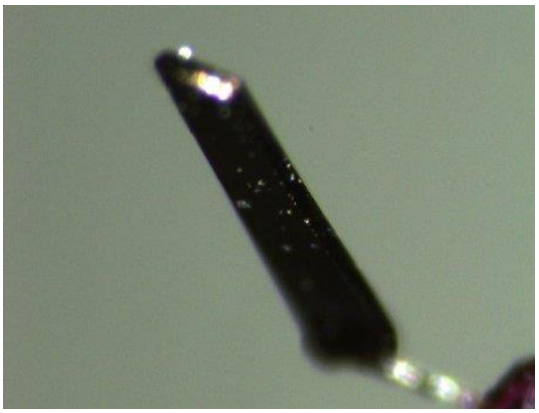

Fig. S16 Crystal view of di(HTh1BT)IDT crystal

References:

[1] Saint Program included in the package software: APEX3 v2015.5.2.

[2] SADABS. Ver. 2014/5. Krause, L., Herbs-Irmer, R., Sheldrick, G. M. Stalke, D. **(2015).** *J. Appl. Crystallogr*. 48.

[3] SHELXT-Integrated space-group and crystal-structure determination Sheldrick, G. M. *Acta Crystallogr., Sect. A* **(2015),** A71, 3-8.

[4] SHELXTL Sheldrick, G. M. Ver. 2014/7. *Acta Crystallographica. Sect C Structural Chemistry* 71, 3 - 8.

[5] WinGX Farrugia, L. J. *J. Appl. Cryst.* 32, **(1999),** 837-838.

[6] Sluis, P. v.d.; Spek, A. L. *Acta Crystallogr., Sect. A* 46, **(1990),** 194-201.

[7] Spek, A. L. *J. Appl. Cryst.* **2003**, 36, 7-13.